uc3m | Universidad Carlos III de Madrid

Dpto. Bioingeniería e Ingeniería Aeroespacial
Escuela Politécnica Superior

A numerical study of turbulent heat transfer in pipes

Autor
Antonio Antoranz Perales

Directores de Tesis
Oscar Flores
Manuel García-Villalba

Leganés, Septiembre 2017

TESIS DOCTORAL

A NUMERICAL STUDY OF TURBULENT HEAT TRANSFER IN PIPES

Autor: Antonio Antoranz Perales

Directores de Tesis: Oscar Flores, Manuel García-Villalba

Firma del Tribunal Calificador:

Firma

Presidente:

Secretario:

Vocal:

Calificación:

Leganés, de Septiembre de 2017

Para mi mujer, mis padres y mi hermano.
Os quiero.

Abstract

The present work is devoted to the detailed study of the turbulent heat transfer problem in a pipe flow with variable fluid properties subjected to highly non-uniform heat flux distribution on the pipe surface. This problem aims to be representive of the conditions found in the tubes of heat receivers in Solar Power Tower (SPT) plants where sun radiation is converted into electric energy. The operational and economical performance of SPT plants rely on an accurate prediction of the thermal field, sometimes beyond the current semi-empirical approach to the heat transfer problem. Moreover, this study might be of interest for many other heat transfer applications in engineering.

The primary intention of this thesis is to shed some light on the influence of the circumferentially-varying heat flux conditions and of the temperature-dependent fluid properties in the statistics of a fully-developed turbulent flow. To that end, we create and analyze a numerical database modifying the main flow parameters of interest: the friction Reynolds number ($Re_\tau = 180 - 360$), the Prandtl number ($Pr = 0.7 - 4$), the heat flux distribution and the sensitivity to temperature of the fluid variables.

From the analysis, we observe that, while the friction Reynolds number has little effect on the temperature distribution on the pipe wall, the impact of the Prandtl number is significant. This is of importance for the heat receiver application, as the maximum flow temperature at the inner wall, the so-called film temperature, might be always below certain limit.

Another important outcome from the analysis of a case with a heated half of the pipe but cooled in the other half is that, because of the influence of the variable fluid properties, the temperature turbulent fluctuations are enhanced near the cold wall but damped near the hot wall. This behavior is seen to reduce the maximum temperature peaks in the flow while maintaining a similar wall temperature distribution. The variation of the fluid properties are also shown to induce small but discernible secondary velocities in the pipe cross-plane. These velocities are responsible of a non negligible contribution to the heat flux from the heated wall to the cooled wall.

To gain a deeper insight in the turbulent heat transfer phenomena, we perform a modal decomposition of the instantaneous velocity and temperature fields to extract the information on the most energetic coherent structures in the flow. The use of a relatively new technique, Extended Proper Orthogonal Decomposition, allows us to discern how the velocity fluctuations are correlated to the temperature fluctuations, hence increasing our knowledge in the heat transfer process. From this analysis, we characterize the modes that are responsible of the heat transport in the pipe cross-plane, obtaining that the scales of the structures bringing hot fluid from the heated wall to the pipe core are strongly affected by the Prandtl number.

Resumen

Este trabajo está orientado al estudio detallado del problema de transferencia de calor turbulenta en un tubo sujeto a un flujo de calor no uniforme en la superficie y recorrido por un fluido con propiedades dependientes de la temperatura. El estudio de este problema busca ser representativo de las condiciones de trabajo de los tubos en un receptor solar de torre. La operación de estas plantas de energía solar térmica por concentración depende en gran manera de obtener una solución precisa del problema térmico, muchas veces por encima de lo que proporcionan las correlaciones actualmente en uso. La resolución de este problema es, además, de utilidad para otras muchas aplicaciones en ingeniería

El principal objetivo de esta tesis es contribuir al avance en el entendimiento de la influencia de las condiciones de contorno térmicas no uniformes y de las propiedades del fluido variables en las estadísticas del flujo turbulento dentro del tubo. Con este fin, se ha generado una base de datos numérica modificando los parámetros del problema: el número de Reynolds de fricción ($Re_\tau = 180 - 360$), el número de Prandtl ($Pr = 0.7 - 4$), la distribución de radiación en la superficie y la sensibilidad de la viscosidad y la difusividad del fluido con la temperatura.

En el estudio hemos observado que, mientras que el número de Reynolds tiene poco efecto en la distribución de temperatura, el impacto del número de Prandtl es significativo. Este resultado es de importancia para el diseño de los receptores solares ya que su operación tiene limitado el rango de temperaturas de funcionamiento.

Otro resultado notable del estudio es la observación del efecto que tiene el calentamiento o enfriamiento de la pared en un caso con propiedades variable del fluido. Debido al cambio de viscosidad con la temperatura, se obtiene que la fluctuaciones de temperatura incrementan cerca de la superficie fría y se amortiguan en la superficie caliente.

La variación de propiedades con la temperatura produce además la generación de pequeñas pero distinguibles velocidades medias en el plano del tubo. Estas velocidades secundarias son responsables de una contribución no desdeñable del flujo de calor total.

Con objeto de profundizar en el fenómeno del flujo de calor turbulento en el tubo, se ha realizado un descomposición modal de los campos de velocidad y temperatura instantáneos, extrayendo las estructuras más energéticas en el flujo. Usando la técnica de EPOD (Extended Proper Orthogonal Decomposition), se han identificado las estructuras turbulentas responsables de la transferencia de calor. Se ha observado que, en el rango considerado, el tamaño de estas estructuras es poco dependiente del número de Reynolds pero está muy afectado por el número de Prandtl.

Agradecimientos

Quisiera sinceramente agradecer a mis directores de la tesis, Manolo García-Villalba y Oscar Flores, sus buenos consejos, su perfecta orientación, su apoyo continuo y su enorme dedicación. Las discusiones técnicas que hemos mantenido sin duda han venido a mejorar sustancialmente el resultado de este trabajo.

Gracias a mis compañeros de doctorado Alex Gonzalo, Manuel Moriche y Toni Almagro por su ayuda en todos los aspectos, desde configurar mi usuario hasta enseñarme como lanzar mis casos. Sin vosotros esto habría sido aún más difícil.

Mi agradecimiento a mis padres por haberme dado todo lo que tenían y haberme permitido llegar hasta aquí. Os lo debo todo a vosotros.

A mi esposa, Isabel, gracias por quererme y aguantarme. Ya queda menos.

Madrid, 14-07-2017

Al bien facer jamás le falta premio
Don Quijote de la Mancha
Miguel de Cervantes

Contents

1 Introduction

1.1 Motivation

Energy drives the world.

Our society has an imperative need for power. We need energy for our houses, cars, appliances, phones and everything that makes our life so technological. Power has been obtained from the combustion of oil, gas, coal or other solid fuels for more than two centuries. The industrial activities of our modern civilization produce millions of tons of contaminants and "greenhouse effect" gases every year. Evidences of climate change and global warming are now overwhelming and there is a clear consensus that we might blame on human kind and its reliance on energy (NASA, 2017). Carbon dioxide, methane and nitrous oxide have caused much of the observed increase in Earth's temperatures over the past 50 years. Global climate change is now a reality and has observable effects on the environment.

Green energy collected from renewable resources, which are naturally replenished on a human timescale, such as sunlight, wind, rain, tides, waves, and geothermal heat are becoming important sources of energy in some areas as electricity generation, air and water heating/cooling or transportation among others (Renewable energy, 2017). Research on non-polluting modes of power generation has received a substantial boost in the 21th century. Latest developments in the technology of solar thermal collectors, improving efficiency and operational costs, has risen the interest on using the energy coming from the sun for industrial purposes. Among other plants architectures, Concentrated Solar Power (CSP) plants have proved very effective in fulfilling heat requirements in industries and for electric power production. In the two mainstream technologies for CSP, central-tower technology and parabolic trough technology, the radiation from the sun is concentrated on tubes containing a heat transfer fluid (HTF), typically a molten salt, which increases its temperature by heat conduction and forced convection. We are interested in investigating the turbulent heat transfer that occurs in the fluid running through those pipes.

The present work is devoted to the detailed study of the heat transfer problem in the fully-developed turbulent flow in a pipe subjected to highly non-uniform heat flux distribution on the pipe surface as found in the tubes of heat receivers in Solar Power Tower (SPT) plants. The problem is further complicated because the fluid properties of the molten salts flowing through the pipes are strongly dependent on temperature. An accurate solution of the problem is of the greatest importance since the operation of the plant must ensure that the temperature of the salt never reaches the decomposition temperature nor the melting temperature.

The study of heat transfer in tubes with non-uniform heating is of interest for many others ap-

plications in engineering. There are currently very active areas of research in cooling systems for electronic devices formed by micro heat pipes where the working fluid follows an evaporation and condensation process. This boiling heat transfer also plays an important role in the case of water cooled pipes in nuclear reactors. Accurate prediction of temperature is essential to avoid overheating when a boiling crisis occurs. The performance of heat exchangers, especially those of shell-and-tube or finned tube types, rely on simplified correlations that might need to be reconsidered in applications with varying heat flux. Finally, another example where the heat transfer problem exceeds the capabilities of the usual correlations is the internal cooling of static or rotating airfoils in a jet engine turbine. Airfoil life prediction highly depends, among other considerations as material properties, on an accurate solution of the metal-coolant heat transfer problem.

The findings and conclusions from this work should contribute to a better understanding of the flow performance in the central receiver of SPT but might also add novel data to be used in other pipe flow applications.

1.2 Central Power Towers

In contrast to photovoltaic systems, which generate electricity rather than heat, solar thermal technology uses the energy from the sun to generate low-cost, environmentally friendly thermal energy (Solar thermal energy, 2017). Solar thermal collectors range from low-temperature collectors that are typically used for heating water or air for residential and commercial use to high-temperature collectors that concentrate sunlight using mirrors or lenses and are generally used for electric power production or industrial heat. The largest facilities in the world using the technology of concentrated solar thermal power are located in the American Mojave Desert of California-Nevada and in the south of Spain. Some examples of the enormous size of these facilities in the United States are the Ivanpah Solar Power Facility (377 MW), the Solar Energy Generating Systems installation (354 MW) and the Crescent Dunes (110 MW). Spain is the other major developer of solar thermal power technology. The largest facilities are Solnova Solar Power Station (150 MW), the Andasol Solar Power Station (150 MW) and Extresol Solar Power Station (100 MW). In the field of Central Power Tower systems, the Gemasolar plant, settled near Seville (Spain), plays a leading role. Gemasolar, developed by SENER and property of Torresol Energy, was the first commercial plant to generate electricity with solar technology using a central tower receiver, a heliostat field and a molten-salt heat storage system (ISE, 2017).

Central Power Tower systems utilize sun-tracking mirrors called heliostats to reflect solar radiation onto a receiver located at the top of a tower more than 100 meters high. The heat transfer fluid running through the receiver, a molten salt in our case, absorbs highly concentrated solar radiation increasing its temperature up to $850K$. The hot salts are stored in a hot tank from where they can be driven on demand to generate water steam, which is used in a conventional turbine-generator to produce electricity. The main advantages of using molten salts and aheat storage system are that the plant can supply power at times when there is no sunlight and direct generation is not

Figure 1.1: Heliostat field and power tower at Gemasolar plant (taken from Gemasolar, 2017).

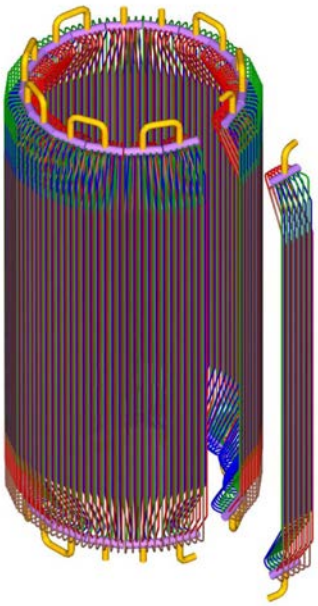

Figure 1.2: Heat receiver (taken from Rodríguez-Sánchez *et al.*, 2014).

possible and that the production peaks can be decoupled from demand peaks. As an example, in the summer of 2013, Gemasolar plant achieved continuous production, operating 24 hours per day for 36 consecutive days (Gemasolar, 2017).

A key element of a CPT is the heat receiver. As explained in Rodríguez-Sánchez *et al.* (2014), the molten salt external receivers are configured as cylindrical tubular receivers, formed by a variable number of thin-wall straight tubes that gather into panels and through which the HTF flows as a serpentine. The receiver tubes are typically made of high nickel based alloy steel finished with a high absorptivity black coating. The main challenge associated with the design of the receiver tubes is the high temperature gradient at the receiver surface and transient thermal processes that may lead to local hot spots, and consequently, degradation or failure of the receiver. Film temperature (or maximum temperature of the HTF) is the most limiting parameter for the

receiver design because it is responsible for salt decomposition and tube corrosion.

For the application of a Central Solar Receiver (CSR) using molten salts in pipes of typically $25mm$ diameter, the working conditions are characterized by flow bulk velocities of about $1 - 3m/s$ and bulk temperatures in the range of $500 - 750K$. At these conditions, and depending on the salt used (Solar Salt, Hitec or Hitec XL for example), the typical working range for the bulk Reynolds number is $Re_b = 2U_bR/\nu = 5 \cdot 10^3 - 5 \cdot 10^4$, where U_b is the bulk velocity, R is the pipe radius and ν is the kinematic viscosity. The Prandtl number varies in the range $Pr = 4 - 20$.

The tube face exposed to the solar radiation receives a heat flux of order $q''_w \sim 1MW/m^2$ while the opposite face is almost adiabatic. This highly non-uniform heat flux distribution produces significant circumferential temperature variations on the pipe wall, ranging from $\Delta T = 50 - 250K$ along the pipe (Rodríguez-Sánchez *et al.*, 2014). In terms of fluid properties variation, this temperature difference produces changes in density of about $5 - 10\%$, in specific heat coefficient of about $2 - 5\%$, in diffusivity of about $10 - 30\%$ and in viscosity of about $100 - 200\%$ from the hot face to the cold face.

The influence on the heat transfer fluid performance produced by the changes in fluid properties is of utmost importance from an economical and operational point of view. The operation of the plant must ensure that the temperature of the salt never reaches the decomposition temperature nor the melting temperature. The admissible temperature range to avoid salt degradation or solidification of the Solar Salt is from $530K$ to $870K$, while Hitec and Hitec XL salts can range approximately from $430K$ to $800K$ (Benoit *et al.*, 2016). A small increase of the film temperature above certain limit can produce a sharp rise of the tube corrosion rate and stress corrosion cracking (Rodríguez-Sánchez *et al.*, 2014).

1.3 State of the art

Numerous investigations have been devoted to the canonical case of a pressure-driven flow in a circular pipe since the origins of Fluid Dynamics. Based on the analysis of the flow in a pipe, Osborne Reynolds (1883) published his famous paper in which the concept of Reynolds number was introduced. Prandtl (1904) and Von Kármán (1937) used turbulent pipe flow data to establish the concept of mixing-lenght obtaining the expression for the logarithmic law. The problem of turbulence heat tranfer in a pipe has also risen the interest from many researchers. Since the studies of Nusselt (1927), many authors have investigated this problem from the experimental, analytical and numerical point of view. Widely used in industry are, for example, the empirical correlations after the work of Dittus & Boelter (1930) and Gnielinski (1976). Most of these correlations were obtained for cases with uniform heating and constant fluid properties, although corrections have been proposed to account for the influence of the variation of physical properties with temperature in heat transfer and skin friction (see e.g. Petukhov, 1970). Nowadays, turbulent pipe flows are still object of intense research (the recent thematic issue on high Reynolds number wall turbulence Klewicki *et al.* (2017) is a good example) because of their significant interest for engineering.

In spite of this practical relevance, turbulent heat transfer in pipes has not been so thoroughly studied through Direct Numerical Simulations (DNS) as other wall bounded canonical flows. The main reason might have been the numerical difficulties associated with the cylindrical coordinate system and the corresponding numerical singularity along the symmetry line. There are some DNS of turbulent pipe flow without heat transfer like those of Wu & Moin (2008), El Khoury *et al.* (2013) and Chin *et al.* (2014). DNS of heat transfer in pipes with *homogeneous* heating are available, for example, in the papers of Piller (2005) and Redjem-Saad *et al.* (2007). To the best of our knowledge DNS of pipe flow with *circumferentially-varying* heat flux of application to our case of study are not available in the literature.

Reference articles for the study of *circumferentially-varying* heat flux in a pipe are, for example, the experimental works of Black & Sparrow (1967) and Quarmby & Quirk (1972) and the RANS analysis of Reynolds (1963), Gärtner *et al.* (1974), Launder (1978) and Baughn *et al.* (1984), but in all of them fluid properties are considered uniform.

From those experimental studies, it is clear that the effective thermal diffusivity in a circular pipe is significantly non-isotropic, being higher in the circumferential than in the radial direction (Quarmby & Quirk, 1972). Besides this empirical evidence, many RANS calculations of the turbulent heat-transfer still use isotropic models for the thermal eddy-diffusivity as the one employed by Reynolds (1963). Gärtner *et al.* (1974) improved on Reynolds results by employing a non-isotropic model. Later, Launder (1978) suggested that, for an axisymmetric fully-developed velocity field, the ratio of circumferential-to-radial heat eddy diffusivities can be approximated by the ratio of the corresponding mean square velocity fluctuations. Baughn *et al.* (1984) applied this model to the case of a pipe with a top-half heating distribution (constant heat flux on one half of the pipe but adiabatic conditions on the other half) obtaining remarkable better results that when using an isotropic eddy diffusivity model.

Regarding the studies on temperature-dependent fluid properties, the works of Zonta *et al.* (2012) and Lee *et al.* (2013) stand out as the more relevant for the current study. Zonta *et al.* (2012) carried out DNS of a forced convection turbulent flow in a channel with anisotropic temperature-dependent viscosity. They considered constant temperature boundary conditions but different gradients between the channel walls. They observed an increase of turbulence kinetic energy in the cold wall but a decrement on the hot wall. Impacts on temperature fluctuations or turbulent heat fluxes were not reported. Lee *et al.* (2013) run DNS of a turbulent boundary layer over heated walls to investigate the effect of viscosity stratification. They found that, in the heated flow, the turbulence energy diminished in the buffer layer, leading to smaller levels of Reynolds shear stresses and hence in a reduction of skin friction. Temperature fluctuations were shown to decrease when increasing the wall temperature.

1.4 Purpose of the thesis and objectives

The present thesis is concerned with the study of the forced-convection heat transfer in a turbulent pipe flow with variable fluid properties and subjected to a non-homogeneous heat flux distribution. The intention is to gain, using Direct Numerical Simulations, a better understanding of the fundamental flow characteristics in the tubes of heat receivers using molten salts as found in modern Solar Power Tower plants.

The problem of study in this thesis departs significantly from the canonical pipe flow analysis. The introduction of circumferentially-varying heat flux boundary conditions and variable fluid properties complicate substantially the analysis. We address this problem sequentially by establishing two approaches.

For the first approach, we consider the heat transfer problem of fully-developed turbulent pipe flow with a sinusoidal heat flux distribution on the upper half of the pipe and adiabatic conditions on the lower half, replicating the conditions on a Central Solar Receiver (CSR). The problem is however simplified by considering constant fluid properties for the heat transfer fluid. See that, with this approximation, the temperature field can be considered as a passive scalar. This approach allows the use of periodic boundary conditions at the inlet and outlet of the pipe with only performing a change of variable in the temperature to account for the temperature increase along the tube, as explained later in this thesis.

As a second approach, we introduce in the simulation a representative variation with temperature of the kinematic viscosity and the thermal diffusivity for the HTF. By contrast, we modify the more realistic heat flux boundary condition from the first approach to allow the use of periodic boundary conditions at the inlet and outlet of the pipe. The pipe is then subjected to a pure sinusoidal heat flux condition on the surface, adding no net heat into the pipe. See that, as it will be apparent later, the use of the more realistic heat flux boundary condition would imply an increase of temperature from pipe inlet to outlet, hampering the use of periodic boundary conditions in the DNS because of the temperature-dependant fluid properties. Note also that, despite the different approach, we still maintain a non-uniform heat flux boundary condition which varies in the circumferential direction and that might produce a temperature variation range similar to those found in the tubes of a Central Solar Receiver (CSR).

Considering the purpose of the thesis and the approximation to the problem described, this thesis focus on three main objectives.

The first objective of the study is to generate a numerical database at different Reynolds and Prandtl numbers with three main purposes. First, to analyse the influence of these parameters in the velocity and temperature characteristics within the pipe. Second, to generate information for RANS RANS turbulence models benchmarking. Third, to evaluate eddy diffusivity models currently in use for the preliminary design of the heat receivers.

The second objective is to gain a better insight on which coherent structures in the flow field are the main responsible of the heat transport inside the pipe. To that end, we use the generated

numerical database to carry out a modal decomposition analysis of the fluctuating velocity and temperature fields. By means of an Extended Proper Orthogonal Decomposition (EPOD) method we aim to obtain an understanding of the correlated events on the turbulent flows under study.

The third and final objective is to analyse the influence of the variable HTF properties on the mean flow values and turbulence statistics in the pipe and to provide with quantitative results for the main parameters affecting the operation of the Solar Central Power: flow friction, heat transfer and peak temperatures.

1.5 Organization of the thesis

In order to adress the objectives established above, the thesis is organized in three chapters.

Chapter 2 is devoted to the analysis of the turbulent heat tranfer in a pipe flow with a heat flux distribution replicating the conditions on a Central Solar Receiver (CSR) but with constant fluid properties for the HTF (first approach described above). Direct Numerical Simulations are conducted for three cases, varying the friction Reynolds number from $Re_\tau = 180$ to 360 and the Prandtl number from $Pr = 0.7$ to 4. The temperature statistics are analyzed and compared for the different cases. Finally, the eddy-diffusivities and the turbulent Prandtl numbers obtained from the computations are contrasted with the approximations used in the literature for RANS analysis.

These numerical database is further analyzed in Chapter 3 by aplying a modal decomposition analysis. The modes obtained by means of POD and EPOD methods for the velocity and temperature fields are presented and discussed. The flow structures responsible for the most of the heat flux in the pipe flow are identifies and then their contributions are quantified.

Finally, we address the problem of variable fluid properties in Chapter 4. Following the second approach described above, DNS are performed for a turbulent pipe flow with sinusoidal heat flux conditions on the surface and temperature-dependent viscosity and thermal diffusivity, representative of the characteristics of the molten salts used in CSR. The analysis is conducted on three cases with different sensitivity of the fluid properties to temperature: null, low and high sensitivity, corresponding the latter with the behavior of the molten salt. We analyse and compare the velocity and temperature turbulent statistics to measure the influence of the variable properties. By considering local wall units, we try to determine the scaling laws in the viscous and thermal sublayers applicable for all three cases. Heat fluxes associated with the secondary flow in the cross-plane created by the variation in fluid properties are calculated and compared with the turbulent and diffusive heat fluxes. Last but not least, the overall performance of the pipe flow is quantified in terms of friction coefficient, heat transfer coefficient and film temperature for the three cases.

2 Influence of realistic thermal boundary conditions

This chapter studies the turbulentheat transfer in a pipe flow with circumferentially-varying heat flux in the upper side but with adiabatic conditions in the lower side. Three DNS are performed for friction Reynolds number in the range 180–360 and Prandtl number in the range 0.7–4. The enphasis is placed in the comparison of actual eddy diffusivities and turbulent Prandtl numbers for radial and circumferential with literature models.

2.1 Introduction

Prediction of turbulent flows characterized by large temperature gradients and high heat-transfer rates is of great importance in engineering. Heat exchangers, combustion chambers, nuclear reactors and cooling systems in electronic devices are just some of the well-known examples in which significant temperature variations typically occur within the flow. In particular, the motivation for this study is the flow in the tubes of the heat receiver of concentrated solar power towers (Moore *et al.*, 2010; Kolb, 2011). The heat receivers are formed by thin-walled metal tubes, assembled into panels. Heliostats located around the tower concentrate the solar radiation onto the tubes. Since the tubes are irradiated only on their outward facing side, they are subject to highly non-uniform heat flux. The heat transfer fluid, typically a molten nitrate salt, flows through the tubes increasing its temperature by convection. From a design point of view, the problem is complicated since the density, the viscosity and the heat conductivity of the salts are temperature dependent. Although the Reynolds numbers of operation are not extremely large, in the range $Re_b = 2U_bR/\nu = 5 \cdot 10^3$ – $5 \cdot 10^4$, where U_b is the bulk velocity, R is the pipe radius and ν is the kinematic viscosity, the Prandtl numbers are large, in the range 4–20 depending on the employed salt. The operation of the plant must ensure that the temperature of the salt never reaches the decomposition temperature nor the melting temperature. This is not always easy to predict and requires a greater understanding of the temperature distribution than currently available. Such understanding may be obtained through direct numerical simulations (DNS) of fully developed turbulent flow in pipes. These simulations are becoming affordable with the recent advances in computational power, specially for the lower end of the range of Reynolds and Prandtl numbers mentioned above.

In spite of its practical relevance, turbulent heat transfer in pipes has not been so thoroughly studied through DNS as in plane channel flows. The main reason is the numerical difficulties associated with the cylindrical coordinate system and the corresponding numerical singularity along the symmetry line. There are some DNS of turbulent pipe flow without heat transfer like those of Wu & Moin (2008), El Khoury *et al.* (2013) and Chin *et al.* (2014). DNS of heat transfer

Case	Re_τ	Re_b	Pr	Line style
1	180	$5.26 \cdot 10^3$	0.7	Solid (Black)
2	180	$5.26 \cdot 10^3$	4	Dashed (Red)
3	360	$1.16 \cdot 10^4$	0.7	Dashed-dotted (Blue)

Table 2.1: Parameters of the simulations. $Re_\tau = u_\tau R/\nu$, $Re_b = U_b 2R/\nu$, where R is the pipe radius, u_τ is the friction velocity, U_b is the bulk velocity and ν is the kinematic viscosity.

in pipes with *homogeneous* heating are also available, for example Piller (2005) and Redjem-Saad *et al.* (2007). To the best of our knowledge DNS of pipe flow with *circumferentially-varying* heat flux are not available in the literature.

In this paper we report on the turbulent heat transfer in a pipe with circumferentially-varying heat flux by means of DNS of fully-developed turbulent flow. As a first step towards understanding the heat transfer characteristics of the pipes used in heat receivers, we simplify the problem by considering constant fluid properties and somewhat lower Reynolds and Prandtl numbers, as summarized in Table 2.1.

The main objective of the study is to generate a numerical database for RANS turbulence models benchmarking. We are particularly interested in the improvement of eddy diffusivity models, since there is a need to use very simplified models in some practical applications as the preliminary design of the heat receivers of concentrated solar power towers (Flores *et al.*, 2014).

From experimental studies it is clear that the effective thermal diffusivity in a circular pipe is significantly non-isotropic, being higher in the circumferential than in the radial direction, as reported for example by the experiments of Quarmby & Quirk (1972). Besides this empirical evidence, many RANS calculations of the turbulent heat-transfer still use isotropic models for the thermal eddy-diffusivity as the one employed by Reynolds (1963). Gärtner *et al.* (1974) improved on Reynolds results by employing a non-isotropic model. Later, Launder (1978) suggested that, for an axisymmetric fully-developed velocity field, the ratio of circumferential-to-radial heat eddy diffusivities can be approximated by the ratio of the corresponding mean square velocity fluctuations. Baughn *et al.* (1984) applied this model to the case of a pipe with a top-half heating distribution (constant heat flux on one half of the circunference but adiabatic conditions on the other half) obtaining remarkable better results that when using an isotropic eddy diffusivity model. The DNS database reported in this paper will allow to assess the accuracy and validity of such models.

The structure of the paper is as follows. In section 2 the computational setup is presented, including the governing equations and the boundary conditions. Results are presented in section 3. First, the temperature statistics are characterized. This is followed by the evaluation of eddy diffusivities and turbulent Prandtl numbers. Finally, conclusions are presented in section 4.

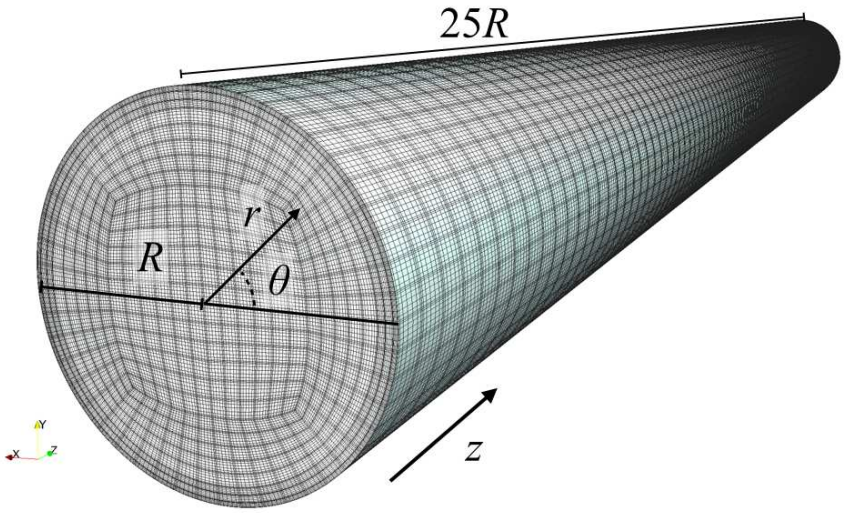

Figure 2.1: Sketch of the computational domain, coordinate systems and mesh.

2.2 Governing equations and computational setup

As discussed in the introduction, the flow configuration studied in the present paper is a pressure-driven incompressible flow of a viscous fluid in a smooth circular pipe of radius R, subjected to a circumferentially-varying heat flux. The fluid has constant density, ρ, kinematic viscosity, ν, thermal diffusivity, α, and specific heat, C_p. Since gravity effects are not considered in the present study, the fluid temperature is simply treated as a passive scalar. Hence, the system of equations that need to be solved are the Navier-Stokes equations for an incompressible fluid (continuity and momentum), together with an advection-difussion equation for the temperature.

In the following the nomenclature used is (x_1, x_2, x_3) for the three cartesian coordinates, with corresponding velocity components (u_1, u_2, u_3). Due to the geometry of the problem, it is convenient to define also cylindrical coordinates (r, θ, z) and velocities (u_r, u_θ, u_z), where $z = x_3$ is the axial coordinate along the pipe axis (see Fig. 2.1). Several averages will be used throughout the paper. The brackets $\langle\cdot\rangle$ indicate mean values, averaged in time and over the homogeneous directions. Primed variables denote fluctuations with respect to these mean values. Bulk variables, denoted with a b subindex, are averaged in time and over the cross-plane (r, θ).

The boundary conditions imposed at the wall are no-slip for the velocity and a circumferentially-

varying heat flux given by

$$q''_w(\theta) = \pi \overline{q}''_w \sin\theta, \qquad 0 < \theta < \pi \tag{2.1}$$

$$q''_w(\theta) = 0, \qquad \pi < \theta < 2\pi \tag{2.2}$$

where $\overline{q''}_w$ is the net heat flux at the wall, which corresponds to the value of the heat flux in a homogeneous heating case with the same total added heat to the system. The imposed heat flux aims to reproduce the heat transfer conditions of the pipes in a heat receiver, where the sun radiation only affects half of the circumference, while the other half can be considered adiabatic. Note that the added heat leads to a net increase of the temperature along the axial direction. A heat balance in a thin slab shows that the bulk temperature T_b increases linearly with z, with a slope given by

$$\frac{\mathrm{d}T_b}{\mathrm{d}z} = \frac{2\overline{q''}_w}{\rho C_p U_b R}, \tag{2.3}$$

where U_b is the bulk velocity.

The net heat flux $\overline{q''}_w$, together with the friction velocity, u_τ, allows the definition of a characteristic friction temperature $T^* = \overline{q''}_w/\rho C_p u_\tau$. When the equations are normalised using the pipe radius R, the friction velocity u_τ and the friction temperature T^*, the only non-dimensional parameters that control the heat transfer are the Reynolds number $Re_\tau = u_\tau R/\nu$ and the Prandtl number $Pr = \nu/\alpha$. Three cases are defined with the values of Re_τ and Pr summarized in Table 2.1.

The linear increase of T_b with z allows us to simplify the advection-diffusion equation for the temperature, by decomposing the temperature field into $T_b(z) + T(r, \theta, z, t)$. The evolution equation for the latter is

$$\frac{\partial T}{\partial t} + u_i \frac{\partial T}{\partial x_i} = \alpha \frac{\partial^2 T}{\partial x_i \partial x_i} - u_3 \frac{\mathrm{d}T_b}{\mathrm{d}z}, \tag{2.4}$$

where the last term acts as a source term. Note that, since dT_b/dz is constant, the axial direction is homogeneous for $T(r, \theta, z, t)$.

Equation (2.4), together with the continuity and momentun equations, are solved using the massively parallel spectral-element method (SEM) solver Nek5000. This code has been developed by Fischer *et al.* (2008), and it solves the incompressible Navier-Stokes equations on Gauss-Lobatto-Legendre nodes. It essentially divides the physical domain into a number of hexahedral elements where the equations of motion are solved by means of local approximations based on high-order orthogonal polynomials basis. Time is advanced with a 3rd order mixed Backward Difference/Extrapolation (BDF3/EXT3) scheme. Along with its efficient parallelization, this code provides spectral accuracy with geometrical flexibility, which makes it suitable for some engineering problems.

The size of the computational domain is selected following El Khoury *et al.* (2013), who performed DNS of turbulent pipe flow (without heat transfer) also with Nek5000. The computational

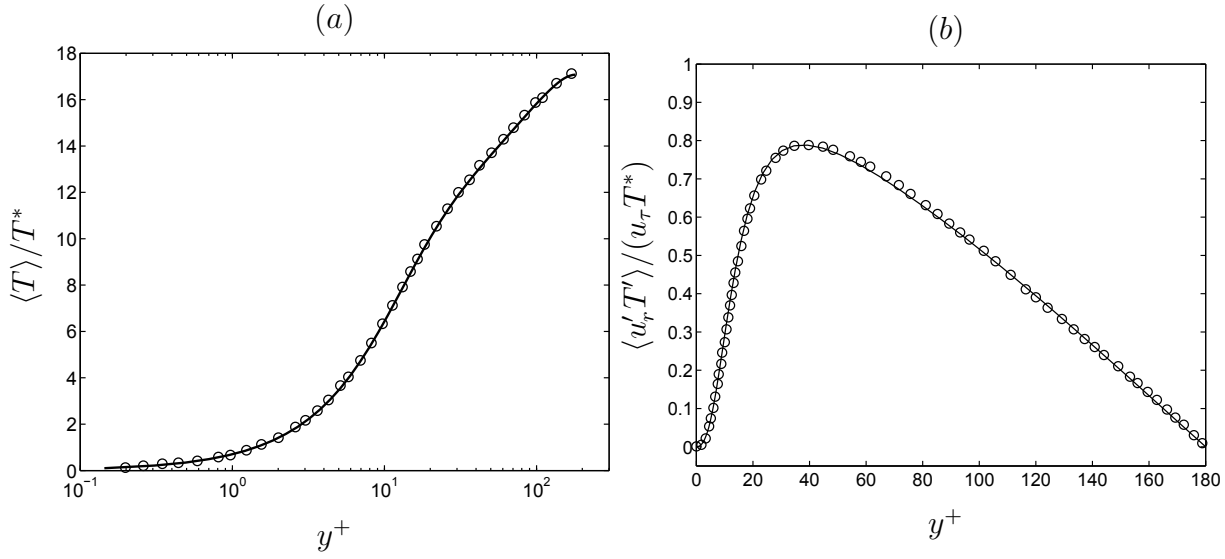

Figure 2.2: Results for the uniform heat flux case. Lines, present calculation. Symbols, data from Piller (2005). (a) Mean temperature $\langle T\rangle/T^*$ as a function to the distance to the wall $y^+ = (R-r)u_\tau/\nu$. (b) Turbulent heat flux $\langle u_r'T'\rangle/(u_\tau T^*)$ vs y^+.

domain is shown in figure 2.1, and it consists of a circular pipe of length $25R$. Since the z direction is homogeneous, periodic boundary conditions are used in at the inlet and outlet of the pipe. The same computational mesh has been used for the three cases. We use a total of 55440 spectral elements of polynomial order $n = 7$, with 105 elements in the streamwise direction and 528 elements in the cross-plane. For cases 1 and 2, the grid spacing in wall units (i.e. normalised with u_τ and ν) is $\Delta r^+_{max} \leq 3.5$, $\Delta(R\theta)^+_{max} \leq 3.5$, $\Delta z^+_{min} \simeq 2.8$ and $\Delta z^+_{max} \leq 9$. The first grid point in the radial direction is located at $\Delta r^+ \simeq 0.25$ from the wall. Case 1 is well resolved, with a resolution slightly better than a similar case reported by El Khoury *et al.* (2013). The resolution for case 2 with $Pr = 4$ is slightly under-resolved compared to a channel flow computation with the same Reynolds number and $Pr = 3$ (Schwertfirm & Manhart, 2007).

The grid spacing for the more demanding simulation (case 3 in Table 2.1) is $\Delta r^+_{max} \leq 7$, $\Delta(R\theta)^+_{max} \leq 7$, $\Delta z^+_{min} \simeq 5.5$ and $\Delta z^+_{max} \leq 18$. The first grid point in the radial direction is located at $\Delta r^+ \simeq 0.5$ from the wall. This case is also slightly under-resolved compared to the simulations reported by El Khoury *et al.* (2013).

The validation of the methodology was performed by carrying out an additional simulation with uniform heat flux, as the one reported by Piller (2005). The friction Reynolds number of the flow was set to $Re_\tau = 180$ and the Prandtl number to $Pr = 0.7$. The velocity statistics were compared to the DNS data of Wu & Moin (2008) and were found to be in good agreement (not shown). Details can be found in Gonzalo (2013). The mean temperature distribution $\langle T\rangle$ and the turbulent heat flux $\langle u_r'T'\rangle$ are displayed in Fig. 2.2. The data of Piller (2005) is included in the figure. Both calculations are shown to be in good agreement.

2.3 Results and discussion

2.3.1 Characterization of the temperature field

First, we provide a general impression of the velocity and temperature fields. Figure 2.3(a) shows a snapshot of the instantaneous streamwise velocity and Figure 2.3(b) displays a snapshot of the instantaneous temperature. Both plots correspond to case 3 with $Re_\tau = 360$ and $Pr = 0.7$. Note that, although the flow is turbulent in the whole pipe and velocity fluctuations are present everywhere, temperature fluctuations are concentrated in the upper part of the pipe. It can be observed that a thin thermal boundary layer develops in the upper region of the pipe where the heat flux is maximum. Near the adiabatic region the temperature distribution is more uniform.

A more quantitative view of the temperature is provided in Figures 2.4-2.6. First, Figure 2.4 displays the mean temperature $\langle T \rangle$ for the three cases, both as a contour plot in the cross-plane and as selected profiles. Also the mean temperature of the uniform heat-flux case (shown in Fig. 2.2) is included for comparison. The profiles are taken along three radial lines at $\theta = \pi/2, \pi/4$ and 0 as indicated in Figure 2.4(a). The distance to the pipe wall is plotted in wall units, $y^+ = (R-r)u_\tau/\nu$, using a logarithmic scale. The mean temperature in the contour plots is normalized with T^* so that the different thickness of the thermal boundary layers can be appreciated when comparing cases 1 and 2, that have the same Reynolds number. On the other hand, Figs. 2.4$(d) - (f)$ show the deviation of the mean temperature with respect to the mean wall temperature $\langle T_w - T \rangle$, normalized with PrT^*. With this scaling all curves corresponding to the circumferentially-varying heat-flux cases collapse in the vicinity of the wall where the molecular conduction dominates over the turbulent heat diffusion.

One of the main concerns of the thermo-solar community is the temperature at wall, the so-called film temperature, since this is one of the main causes of pipe failure and salt degradation during operation. Figure 2.5 shows the variation of the wall temperature, $\langle T_w \rangle / T^*$, as a function of the circumferential coordinate. As expected, the maximum temperature is reached at the location of maximum heat flux, $\theta = \pi/2$, with a value which is slightly dependent on the Reynolds number but strongly affected by the Prandtl number. The comparison between cases 1 and 2 (with the same Reynolds number) suggests that the peak temperature changes as $\sqrt{Pr}$, although more simulations would be needed to confirm this trend.

The characterization of the temperature field is completed by analyzing the root-mean-square (RMS) temperature fluctuations. Figure 2.6 displays the RMS temperature fluctuations, T_{rms}, for the three cases, both as a contour plot in the cross-plane and as selected profiles. The profile of the RMS temperature fluctuations near the wall shows a plateau very close to the wall followed by a peak located at a distance to the wall that depends on the Prandtl number. After this peak the fluctuations decrease monotonically towards the center of the pipe. As shown in DNS of turbulent heat transfer in pipes (see for example Redjem-Saad *et al.* (2007)), when the Prandtl number increases, the peak of temperature fluctuations moves closer to the wall and rises significantly.

(a)

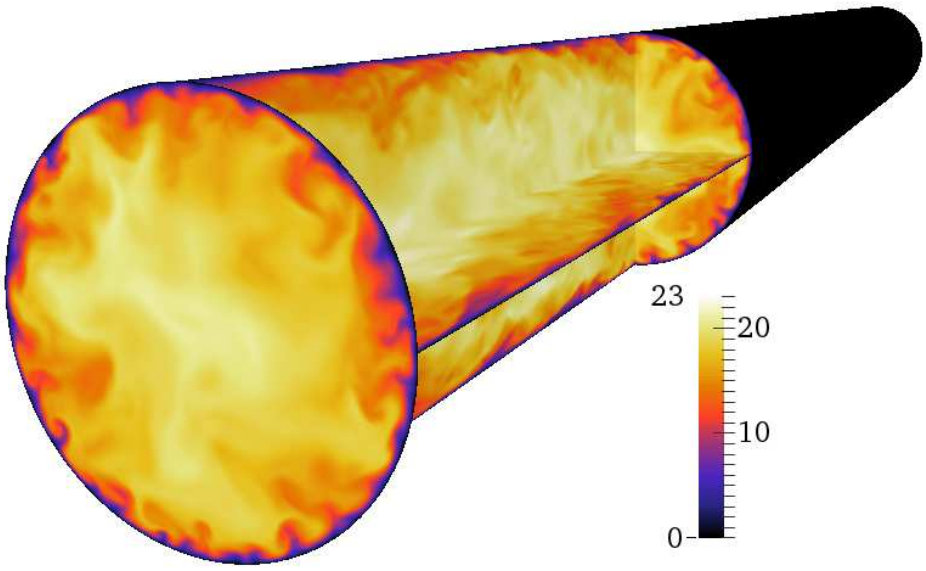

(b)

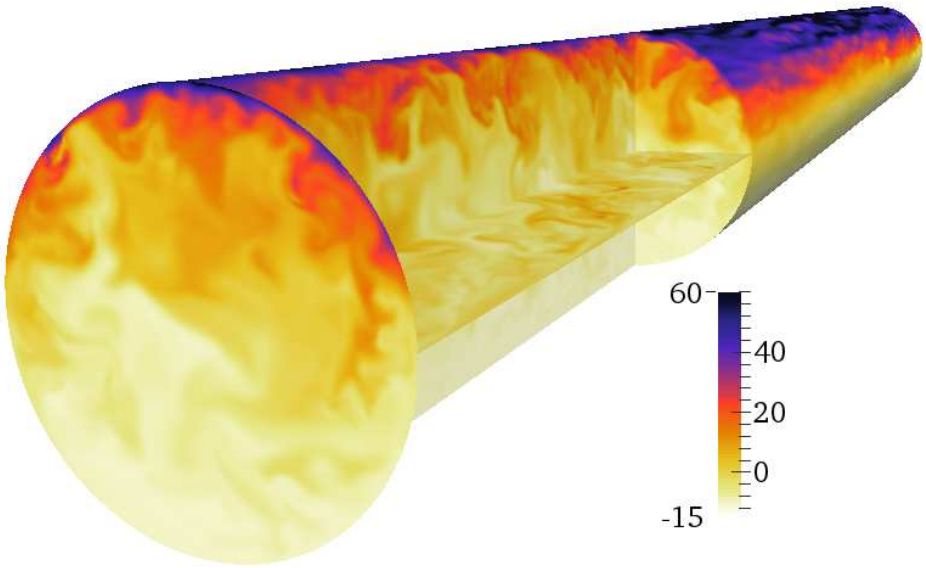

Figure 2.3: (a) Visualization of the instantaneous streamwise velocity, u_z/u_τ. (b) Visualizations of the instantaneous temperature T/T^*. Both visualizations correspond to Case 3 and are taken at the same time.

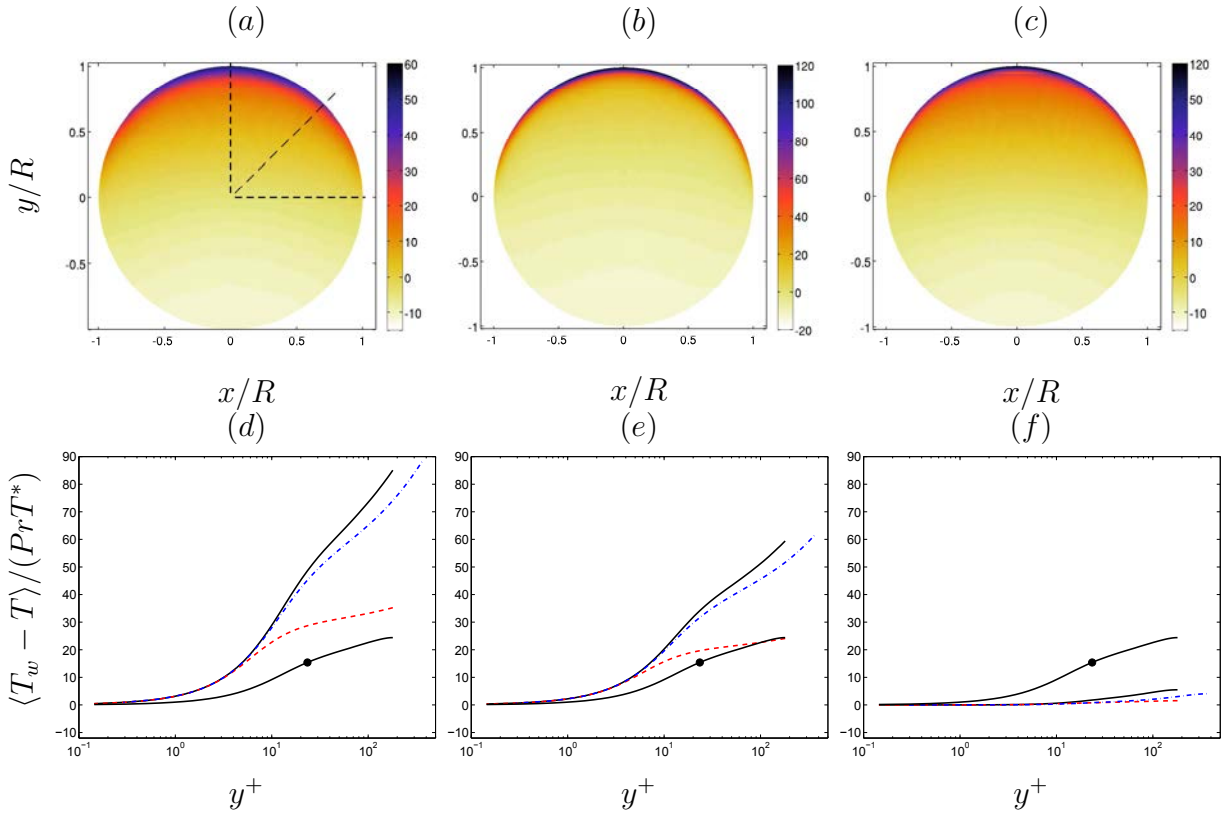

Figure 2.4: $(a)-(c)$ Mean temperature $\langle T\rangle/T^*$ in the cross-plane. Note that the scale is different in each panel. (a) Case 1. (b) Case 2. (c) Case 3. The dashed lines in (a) indicate the angles for which profiles are shown in $(d)-(f)$. $(d)-(f)$ Mean temperature, $\langle T_w - T\rangle/(PrT^*)$, profiles as a function of the distance to the wall y^+. Line styles defined in Table 2.1. The line with the symbol corresponds to the case with homogeneous heating. (d) $\theta = \pi/2$. (e) $\theta = \pi/4$. (f) $\theta = 0$.

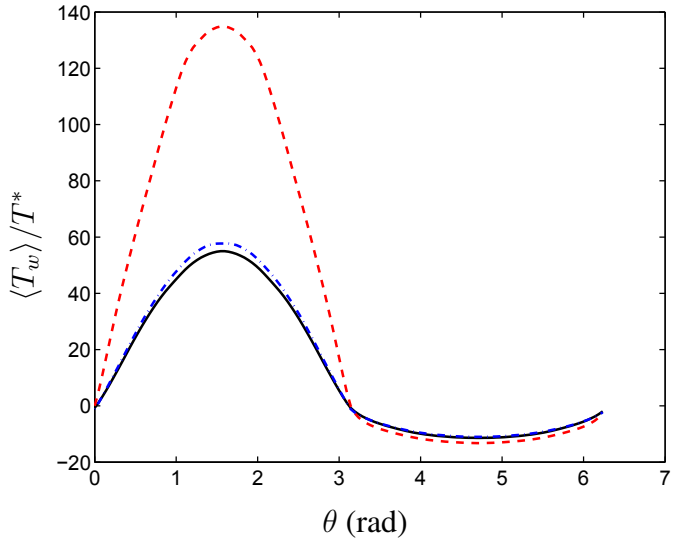

Figure 2.5: Mean temperature at the wall $\langle T_w \rangle / T^*$ as a function of the circumferential coordinate. Line styles defined in Table 2.1.

The present results displayed in Figure 2.6(d) at $\theta = \pi/2$ show that for $Pr = 0.7$ the peak is located at $y^+ \simeq 11$, whilst for $Pr = 4$, this distance reduces up to $y^+ \simeq 7$. This difference is still clearly visible at $\theta = \pi/4$, Figure 2.6(e). At other circumferential locations where the heat flux at the wall vanishes, like in Figure 2.6(f), the temperature fluctuations are much weaker and the Pr effect is less apparent. We have tried several normalizations for the peak temperature fluctuations involving the Prandtl number with inconclusive results. Note that the scaling of thermal boundary layers is an issue of current debate even for canonical configurations (Saha *et al.*, 2014).

2.3.2 Turbulent eddy diffusivity

The development of the fully developed thermal field in a turbulent pipe flow with a circumferentially-varying heat-flux is described by the three-dimensional mean energy equation

$$\langle u_z \rangle \frac{\partial T_b}{\partial z} = \frac{1}{r}\frac{\partial}{\partial r}\left[(\alpha + \varepsilon_{hr})\, r \frac{\partial \langle T \rangle}{\partial r}\right] + \frac{1}{r}\frac{\partial}{\partial \theta}\left[\frac{1}{r}(\alpha + \varepsilon_{h\theta})\frac{\partial \langle T \rangle}{\partial \theta}\right], \tag{2.5}$$

where we have introduced the eddy diffusivities to model the velocity-temperature correlations as

$$\langle u_r' T' \rangle = -\varepsilon_{hr} \frac{\partial \langle T \rangle}{\partial r}, \tag{2.6}$$

$$\langle u_\theta' T' \rangle = -\varepsilon_{h\theta} \frac{1}{r}\frac{\partial \langle T \rangle}{\partial \theta}. \tag{2.7}$$

Figure 2.7 shows the iso-contours obtained in the present DNS for the thermal eddy diffusitivies in radial, ε_{hr}, and circumferential, $\varepsilon_{h\theta}$, directions for Case 1. Although in principle these quantities could be a function of r and θ, the DNS results show that they are roughly functions of r only.

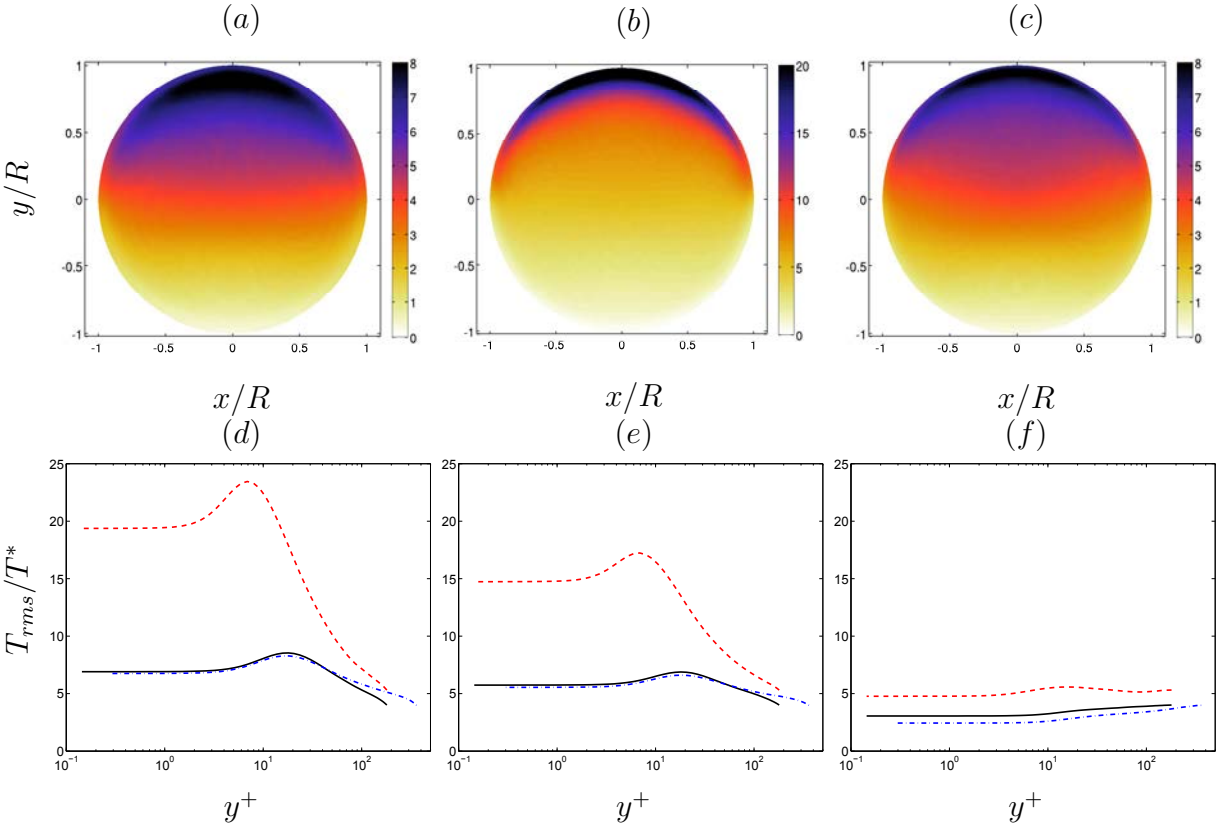

Figure 2.6: $(a)-(c)$ RMS temperature T_{rms}/T^* in the cross-plane. Note that the scale is different in each panel. (a) Case 1. (b) Case 2. (c) Case 3. $(d)-(f)$ RMS of temperature fluctuations, T_{rms}/T^*, profiles as a function of the distance to the wall y^+. Line styles defined in Table 2.1. (d) $\theta = \pi/2$. (e) $\theta = \pi/4$. (f) $\theta = 0$.

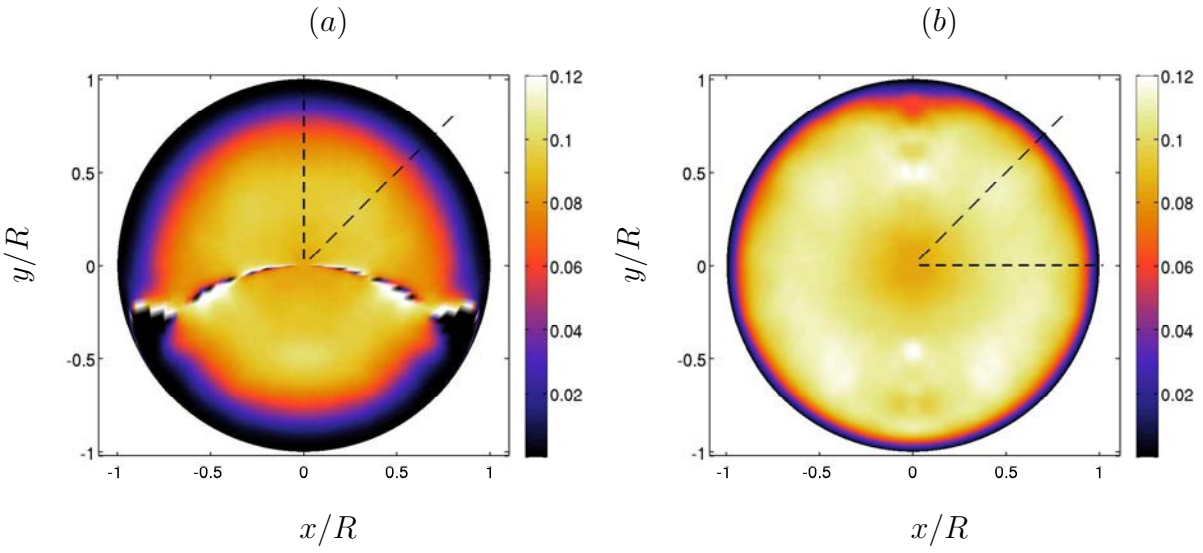

Figure 2.7: Thermal eddy diffusivity in (a) radial, $\varepsilon_{hr}/(u_\tau R)$, and (b) circumferential, $\varepsilon_{h\theta}/(u_\tau R)$, directions for Case 1. The dashed lines show the averaging region for Figure 2.8.

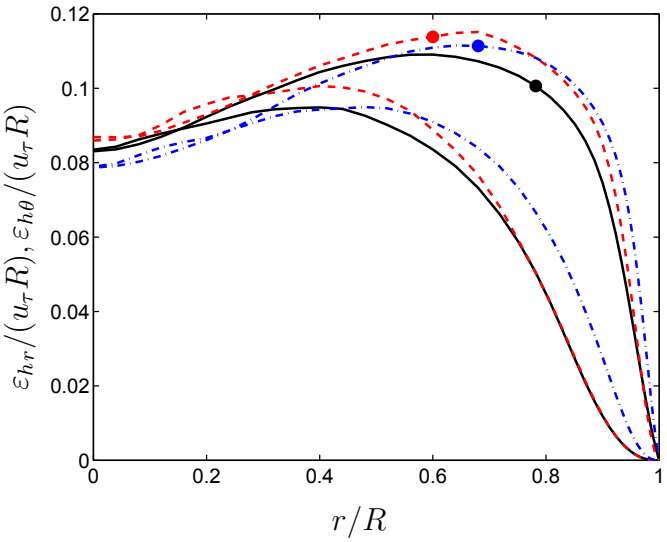

Figure 2.8: Thermal eddy diffusivity for both radial, $\varepsilon_{hr}/(u_\tau R)$ (without symbols), and circumferential, $\varepsilon_{h\theta}/(u_\tau R)$ (with symbols), directions as a function of the radial coordinate, r/R. Line styles defined in Table 2.1.

Singularities appear in ε_{hr} when $\partial \langle T \rangle / \partial r$ goes to zero (near $\theta = 0$ and π). A singularity also occurs for $\varepsilon_{h\theta}$ at $\theta = \pi/2$ where $\partial \langle T \rangle / \partial \theta = 0$ at the wall. At this location $\varepsilon_{h\theta}$ seems to have circumferential variations, Figure 2.7(b). Although not shown here, the results for cases 2 and 3 are qualitatively similar.

In order to avoid the singularities, we have averaged ε_{hr} in the range $[\pi/4, \pi/2]$ and $\varepsilon_{h\theta}$ in the range $[0, \pi/4]$, as shown in Figure 2.7. The resulting eddy diffusivities normalized with $u_\tau R$ are shown in Figure 2.8, where the larger value of the thermal eddy diffusivity in the circumferential direction near the wall can be appreciated. Near the pipe center, both ε_{hr} and $\varepsilon_{h\theta}$ tend to the same values, indicating that the behaviour is rather isotropic. The value at pipe axis seems to be fairly independent of the Prandtl number with the present normalization.

As discussed in the introduction, we now proceed to evaluate the model proposed by Launder (1978). The eddy-diffusivity ratio $\varepsilon_{h\theta}/\varepsilon_{hr}$ is compared with the ratio of the corresponding mean square velocity fluctuations, $\langle u_\theta'^2 \rangle / \langle u_r'^2 \rangle$, both as a function of the distance to the wall in inner units (Figure 2.9). The present results indicate that both ratios differ near the wall. For $y^+ < 20$, the eddy diffusivity ratio is proportional to y^{-1} while the velocity ratio is proportional to y^{-2}. However, it seems that in the pipe core both ratios are of the same order of magnitude. A similar result was obtained in channel flow with heat flux varying in spanwise direction by Matsubara *et al.* (2012). Therefore, a non-isotropic eddy diffusivity model as proposed by Launder should be valid far from the wall. However, in order to provide the correct behaviour near the wall it should incorporate modifications with a proper scaling.

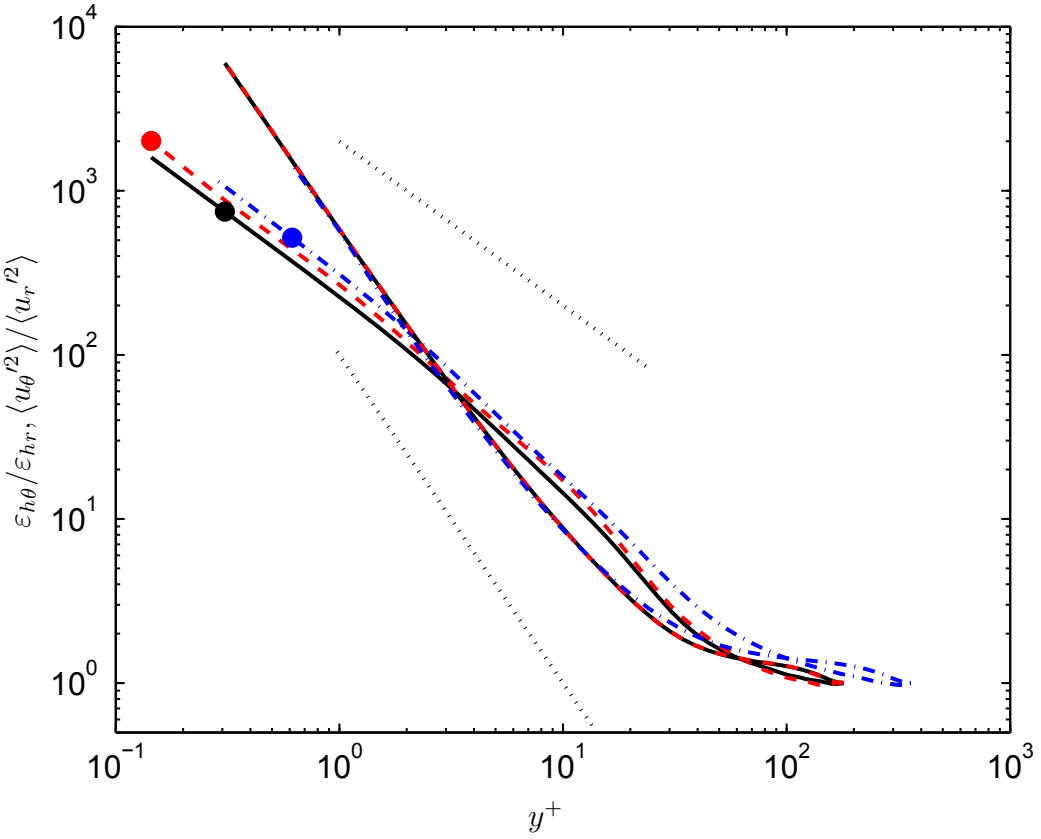

Figure 2.9: Ratio of thermal eddy diffusivities $\varepsilon_{h\theta}/\varepsilon_{hr}$ (with symbols), and ratio of velocity variances $\langle u_\theta{}'^2\rangle/\langle u_r{}'^2\rangle$ (without symbols) as a function of the distance to the wall, y^+. Line styles defined in Table 2.1. The dotted lines have slopes -1 and -2, respectively.

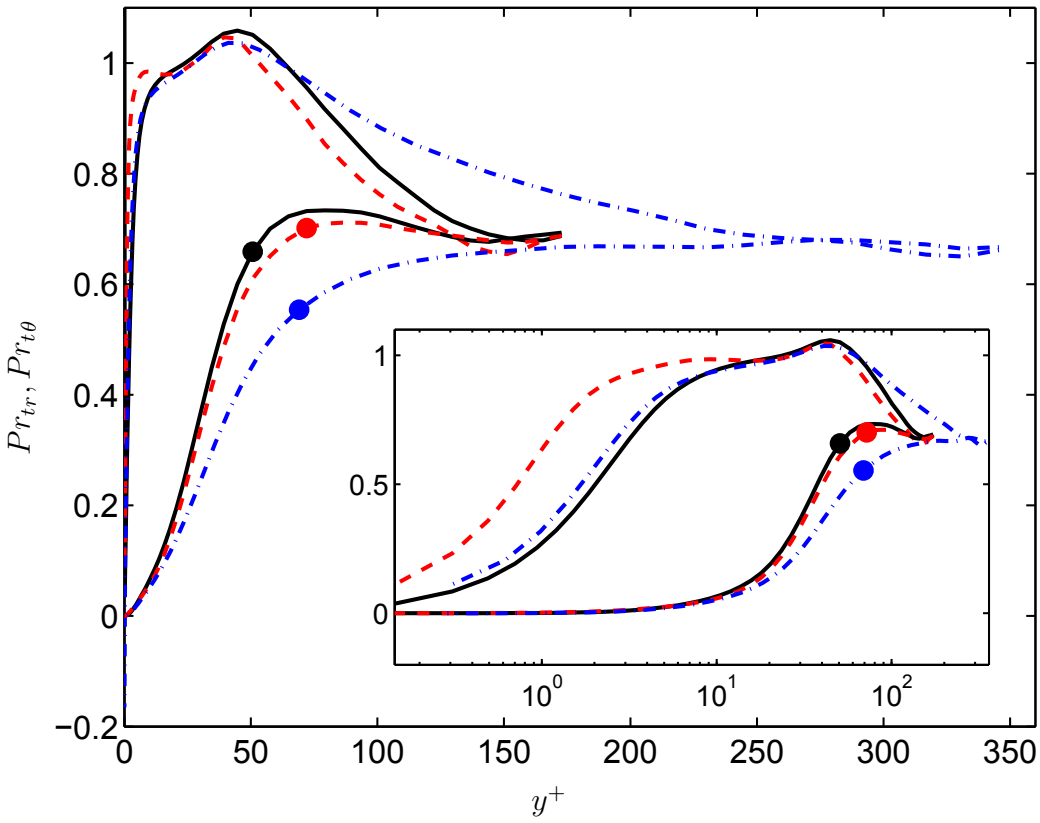

Figure 2.10: Turbulent Prandtl number for both radial, Pr_{tr} (without symbols), and circumferential, $Pr_{t\theta}$ (with symbols), directions as a function of the distance to the wall, y^+. Line styles defined in Table 2.1. The inset displays the same information as the main plot but the x-axis is shown in logarithmic scale.

2.3.3 Turbulent Prandtl number

The knowledge of the turbulent Prandtl numbers is of great importance if we attempt to predict heat transfer from a known velocity field. We define turbulent Prandtl numbers in radial and circumferential directions

$$Pr_{tr} = \frac{\nu_t}{\varepsilon_{hr}}, \tag{2.8}$$

$$Pr_{t\theta} = \frac{\nu_t}{\varepsilon_{h\theta}}, \tag{2.9}$$

where ν_t is the eddy viscosity defined from

$$\langle u_r' u_z' \rangle = -\nu_t \frac{\partial \langle u_z \rangle}{\partial r}, \tag{2.10}$$

Note that in cases with uniform heating, the turbulent Prandtl number Pr_t corresponds to eq. (2.8).

In experiments, it is often difficult to determine the turbulent Prandtl number in turbulent boundary layer flows, since measurements near the wall are hard to obtain. With the advent of DNS, several authors have tried to address this problem, but mainly in cases with uniform heat transfer conditions. The behaviour of Pr_t near the wall is strongly dependent on the temperature boundary conditions. For isothermal walls (Schwertfirm & Manhart, 2007; Redjem-Saad *et al.*, 2007) Pr_t tends to a finite value at the wall that depends on the molecular Pr. For constant heat flux at the wall Pr_t goes to zero at the wall (Chung & Sung, 2003). In the present case, where the heat flux conditions at the wall are non uniform, the characterization of the turbulent Prandtl number in the circumferential direction is of utmost importance.

Figure 2.10 shows Pr_{tr} and $Pr_{t\theta}$ for the three cases. As expected $Pr_{t\theta}$ is lower than Pr_{tr} in the near-wall region, indicating the higher contribution of the circumferential fluxes to the net turbulent heat transfer. As the distance to the wall approaches zero the circumferential turbulent Prandtl number is $Pr_{t\theta} \propto y^2$, while $Pr_{tr} \propto y$. In the buffer region, Pr_{tr} reaches values around 1 and then it decreases smoothly to reach a value $Pr_{tr} \sim 0.7$ in the central part of the pipe. On the other hand, $Pr_{t\theta}$ increases almost monotonically, and at the centre the temperature field becomes more isotropic, leading to $Pr_{t\theta} \sim Pr_{tr}$. At the pipe axis, the turbulent Prandtl numbers reaches a value of roughly 0.7 independently of the change in Re_τ and Pr, which agrees well with previous experimental data (Blackwell *et al.*, 1972; Hollingsworth *et al.*, 1989) and computations (Kim & Moin, 1989).

2.4 Conclusions

DNS of turbulent heat transfer of the fully-developed flow in a pipe with circumferentially-varying heat flux boundary conditions have been conducted for two Reynolds number ($Re_\tau = 180$ and 360) and two Prandtl numbers ($Pr = 0.7$ and 4). The imposed heat flux at the wall aims to

reproduce the heat transfer conditions at the pipes of a heat receiver, therefore, the heat flux at the wall is modelled as sinusoidal from $\theta = 0$ to π and zero (adiabatic condition) from $\theta = \pi$ to 2π.

First, we focus on the mean and root-mean-square temperature distributions on the pipe cross-section. Most of the turbulent fluctuations take place in the upper part of the pipe where the heat flux is maximum. While the Reynolds number has a small impact on the wall temperature distribution, the Prandtl number produces deep changes, being the circumferential variations of temperature more pronounced when Pr is higher.

In orden to analyse the significance of the turbulent heat fluxes, thermal eddy-diffusivities are defined for the radial and circumferential directions similar to the definition of the eddy-viscosity in the momentum equation. Although in principle these quantities could be a function of r and θ, present DNS results show that they are roughly functions of r only. We found a similar ratio $\varepsilon_{h\theta}/\varepsilon_{hr}$ for all Re_τ and Pr cases studied, which varies as the inverse of the wall distance very near the wall. This implies that, although the Launder's hypothesis for the anisotropic behaviour might be valid far from the wall, the asymptotic behaviour of $\varepsilon_{h\theta}/\varepsilon_{hr}$ and $\langle u_\theta^2 \rangle / \langle u_r^2 \rangle$ differ near the wall, implying that a correction of the model is needed.

Finally, the turbulent Prandtl numbers for radial and circumferential directions relating the thermal eddy-diffusivities with the eddy-viscosity are presented and discussed. At the center of the pipe, we obtain an isotropic behaviour with $Pr_{t\theta} \sim Pr_{tr} \sim 0.7$, irrespective of the Re and Pr considered here. Near the pipe wall, however, we find that $Pr_{tr} \propto y^+$ and $Pr_{t\theta} \propto y^{+2}$.

3 Extended proper orthogonal decomposition analysis

This chapter analyzes the role of coherent structures in turbulent thermal transport in pipe flows. This is done base on a model decomposition based on an extended proper orthogonal decomposition. The analysis is performed on a dataset corresponding to the database described in the previous chapter.

3.1 Introduction

In order to identify coherent motion in wall-bounded flows, such as pipes, modal decompositions are often employed. A typical approach consists in decomposing through Proper Orthogonal Decomposition (POD) the fluctuating turbulent fields in orthogonal modes which are representative of the main coherent structures of the flow (Holmes *et al.*, 2012). Coherent structures include motions on different scales in the boundary layer ranging from near wall streaks to large and very large scale motions which in a boundary layer might extend up to 20 boundary layer thicknesses in the streamwise direction. Especially these large scale motions are found to be responsible of up to 50% of turbulent Reynolds stresses (Guala *et al.*, 2006) and are especially interesting for the development of simplified models and the development of control strategies (Rowley & Dawson, 2017).

The POD modes are obtained as a weighted average of flow snapshots and are optimal in an energy sense. The most common choice in turbulent flow studies is to decompose the velocity field, thus identifying the set of modes which is optimum in terms of turbulent kinetic energy. This procedure is well assessed in pipe flows especially in the recent works by Hellström & Smits (2014); Hellström *et al.* (2015, 2016); Hellström & Smits (2017). It can be shown that, for a fully developed flow where the statistical quantities are homogeneous in the tangential direction, POD modes converge to Fourier modes (see, e.g. Hellström & Smits (2014)). These structures correspond to roll-cell like structures (Baltzer *et al.*, 2013) that line up to create very large scale motions which extend up to 30 radii in the streamwise direction.

When dealing with multiple physical quantities such as temperature or pressure it can be interesting to analyse the proper orthogonal modes connected with other quantities of interest. The extended proper orthogonal decomposition (EPOD, Borée (2003)) is based on the use of the same temporal basis to find the modes of whatever data ensemble synchronized with the data ensemble used for the decomposition in order to extract information on correlated events. EPOD has been previously used to correlate several processes with flow coherent structures, as for example wall pressures in Picard & Delville (2000) and flame dynamics in Duwig & Iudiciani (2010). Within

this chapter, datasets of the DNS database discussed in the previous chapter are analysed with EPOD.

While the flow velocity temporal basis is optimal in terms of kinetic energy, the temperature temporal basis is optimal in term of temperature variance, i.e. and therefore connected to turbulent thermal transport. In this chapter we explore the capabilities of the EPOD technique applied to temperature and velocity fields. The aim is to gain an understanding about the physical mechanisms of convective heat transfer by determining and quantifying the flow motions responsible for the temperature fluctuations.

3.2 Proper Orthogonal Decomposition of velocity and temperature fields

3.2.1 Fundamentals of Proper Orthogonal Decomposition

In this paragraph a short introduction to Proper Orthogonal decomposition is presented. A complete discussion can be found in the book by Holmes *et al.* (2012). Consider a turbulent quantity, function of spatial coordinate $\underline{x}$ and time t, $W(\underline{x},t)$. The quantity $W(\underline{x},t)$ can be decomposed according to the Reynolds decomposition as sum of mean and fluctuating field.

$$\begin{aligned} W(\underline{x},t) &= \langle W(\underline{x})\rangle + w(\underline{x},t) \approx \\ &\approx \langle W(\underline{x})\rangle + \sum_{n=1}^{N_m} a_n(t)\varphi_n(\underline{x}), \end{aligned} \tag{3.1}$$

where the symbols $\langle W(\underline{x})\rangle$ and $w(\underline{x},t)$ indicate the time-average and the fluctuating part of $W(\underline{x},t)$, respectively. The fluctuating part can be approximated as a linear combination of a set of spatial basis functions $\varphi_n(\underline{x})$, with coefficients $a_n(t)$ depending on time; the symbol N_m is used to indicate the number of modes, i.e. the rank of the function space. Evidently, in the limit $N_m \to \infty$ the approximation becomes exact.

When choosing a basis function it is often advisable to make it orthonormal, i.e. that the inner product

$$(\varphi_n(\underline{x}), \varphi_p(\underline{x})) = \int \varphi_n(\underline{x}), \varphi_p(\underline{x}) d\underline{x} = \delta_{np} \tag{3.2}$$

with δ_{np} the Kronecker delta equal to 1 for $n = p$ and to 0 elsewhere. Proper Orthogonal Decomposition (POD, Berkooz *et al.* (1993)) is a well assessed tool to extract information on the coherent structures in turbulent flows because it looks at the spatial basis functions $\varphi_n(\underline{x})$ with the larger mean square projections $\lambda_n = \langle (w(\underline{x},t), a_n(t)\varphi_n(\underline{x}))\rangle$.

This leads to the computation of the solution of the integral eigenvalue problem known as Fredholm equation which has as kernel the two-point correlation of w, of which λ_n are the eigenvalues. Considering a set of N_t realizations $W_i(\underline{x})$ of $W(\underline{x},t)$, the integral equation has a discrete set of

solutions: N_t eigenvalues λ_n of the two-point correlation matrix and N_t basis functions $\varphi_n(\underline{x})$. If in every realization, W is discretely sampled in space, e.g. each realization consists of N_p values along the spatial coordinate $\underline{x}$, following the snapshot method Sirovich (1987), it can be treated as an N_p-dimensional vector. The data can be arranged in a $N_t \times N_p$ snapshot matrix:

$$\underline{\underline{w}} = \begin{bmatrix} w(x_1,t_1) \cdots w(x_{N_p},t_1) \\ \vdots \quad \ddots \quad \vdots \\ w(x_1,t_{N_t}) \cdots w(x_{N_p},t_{N_t}) \end{bmatrix}. \tag{3.3}$$

At this point, if the spatial sampling is uniform, the modes can be determined solving the eigenvalue problem of the two-point correlation matrix of w with dimensions $N_t \times N_t$, i.e. $\underline{\underline{C}} = \underline{\underline{w}} \cdot \underline{\underline{w}}^T$ (being $\underline{\underline{w}}^T$ the transpose of $\underline{\underline{w}}$). Solving the eigenvalue problem of $\underline{\underline{C}}$ returns the eigenvalues λ_n and the left and right eigenvector matrices. The left and right eigenvector matrices are respectively the matrix $\underline{\underline{\psi}}$ containing in its columns the temporal modes $\underline{a_n}/\sqrt{\lambda_n}$ (which are orthonormal vectors of length N_t) and its inverse (i.e. its transpose). Note that the columns of $\underline{\underline{\psi}}$ are a basis of rank N_t. The orthonormal spatial modes $\varphi_n(\underline{x})$ can then easily be computed as $\underline{\underline{\Sigma}}\underline{\underline{\varphi}} = \underline{\underline{\psi}}^T \underline{\underline{w}}$ where $\underline{\underline{\Sigma}}$ is a square diagonal matrix having the square root of the eigenvalues λ_n on its diagonal elements. The element of $\underline{\underline{\Sigma}}$ are called singular values of $\underline{\underline{w}}$. Consequently it is possible to express $\underline{\underline{w}} = \underline{\underline{\psi}}\underline{\underline{\Sigma}}\underline{\underline{\varphi}}$.

The computation of the two-point correlation matrix $\underline{\underline{C}}$ is complicated whenever the spatial sampling of W is not uniform. Each element i, j of the two-point correlation matrix of W has to be computed as the scalar product of two realizations of $\underline{W_i} \cdot \underline{W_j}$ which in every point has to be weighted by the corresponding flow area, in order to reflect the different weights attributed by the non-uniform spatial sampling. This means that $\underline{\underline{C}} = \left(A^{-1}\underline{\underline{dA}} \circ \underline{\underline{w}}\right) \cdot \underline{\underline{w}}^T$ in which A is the total area of the flow under analysis, $\underline{\underline{dA}}$ is the matrix containing the local values of area corresponding to each point of the sampling grid and $\circ$ stands for the entry-wise Hadamard product (i.e. the ij^{th} element of $\underline{\underline{dA}} \circ \underline{\underline{w}}$ is equal to $dA_{i,j}w_{i,j}$).

3.2.2 Extracting POD modes when dealing with multiple quantities and the need for extended POD

Whenever analysing realizations involving two or more dimensionally homogeneous quantities, i.e. a velocity vector field with $\underline{U} = (u_x, u_y, u_z)$, it is possible to determine the spatial basis functions which maximize the mean square projections for every velocity component separately. However, it can be shown that the eigenvalue problem of the sum of the two-point correlation matrices for the three velocity components provides modes which are optimal in terms of turbulent kinetic energy (Holmes *et al.*, 2012). When dealing with data non dimensionally homogeneous among them (e.g. a velocity vector field and a fluid density field) it has been shown that, after a proper normalization, it is possible to sum the correlation matrices of all the physical quantities.

The eigenvalues, in this case will contain the variance of a composite mode including both velocity and further physical quantities (e.g. density) (Lumley & Poje, 1997). This approach results to be especially interesting when dealing with "active scalars" such as density in a buoyancy driven flow.

The Extended Proper Orthogonal Decomposition (EPOD, Borée (2003)), instead, is based on the use of the same temporal basis obtained solving the eigenvalue problem of the correlation matrix of $W(\underline{x},t)$ to find the modes of whatever data ensemble synchronized with $W(\underline{x},t)$. EPOD allows to extract further information on correlated events of the two quantities.

The main objective of this work is to analyse the correlation between velocity and temperature, which is responsible for the turbulent transport of internal energy. Temporal bases are obtained solving the eigenvalue problem of both the fluid temperature correlation matrix $\underline{\underline{\psi}}_T$ and the velocity correlation matrix $\underline{\underline{\psi}}_k$. The two temporal bases are optimal in the least square sense for what concerns temperature fluctuations and for the description of turbulent kinetic energy. Temperature and velocity modes are then obtained from both bases:

$$\begin{aligned}
\underline{\underline{\Sigma}}_{u_i,k}\,\underline{\underline{\varphi}}_{u_i,k} &= \underline{\underline{\psi}}_k^T\,\underline{\underline{u_i}},\\
\underline{\underline{\Sigma}}_{T,k}\,\underline{\underline{\varphi}}_{T,k} &= \underline{\underline{\psi}}_k^T\,\underline{\underline{T}},\\
\underline{\underline{\Sigma}}_{u_i,T}\,\underline{\underline{\varphi}}_{u_i,T} &= \underline{\underline{\psi}}_T^T\,\underline{\underline{u_i}},\\
\underline{\underline{\Sigma}}_{T,T}\,\underline{\underline{\varphi}}_{T,T} &= \underline{\underline{\psi}}_T^T\,\underline{\underline{T}}.
\end{aligned} \tag{3.4}$$

In the left hand side of Eq. 3.4 the double subscripts refer to the quantity which has been decomposed and to the temporal basis used for the decomposition respectively, e.g. $\underline{\underline{\varphi}}_{u_i,T}$ refers to the spatial modes of the velocity component u_i obtained projecting the velocity snapshot matrix on the temporal basis $\underline{\underline{\psi}}_T$ obtained from the temperature correlation matrix. It has to be remarked here that the EPOD modes $\underline{\underline{\Sigma}}_{u_i,T}\underline{\underline{\varphi}}_{u_i,T}$ account only for the part the turbulent kinetic energy correlated with the T signal and vice versa. It is thus possible to obtain different spectral distributions amongst modes based on turbulent kinetic energy and on temperature. Eventually it can be possible to identify a part of the correlation matrix $\underline{\underline{C}} = \sum_{i=1}^{3} \underline{\underline{u_i}} \cdot \underline{\underline{u_i}}^T$ which is poorly correlated with the temperature fluctuations and thus contribute to these in a minimal amount.

3.2.3 Some considerations about the physical meaning of the POD modes of temperature fields

As outlined before, POD modes obtained from the solution of the eigenvalue problem of the temperature correlation matrix in a turbulent flow are optimal in the least square sense for the representation of temperature fluctuations variance $(\Delta T)^2$. The physical meaning of this quantity has to be regarded in light of the problem under analysis and of its boundary conditions.

In the present problem the wall heat flux is given and average temperature maps show that a region of higher temperature is located nearby the wall in the region with higher heat flux (corresponding to the angular position $\theta = \pi/2$). The wall heat flux q''_w is given by the product of the convective heat transfer coefficient times the difference between the local wall temperature in the pipe and the fluid adiabatic wall temperature, which locally can be assumed as equal to the fluid temperature outside of the boundary layer $q''_w = h(T_w - T_{fluid})$. For a given wall temperature (hotter than the fluid) and heat flux (constant), a greater convective heat transfer coefficient h allows to increase the fluid temperature of a value ΔT. This means that a modal basis able to describe optimally in the least square sense the fluid temperature fluctuations is able to provide information of the main flow structures able to provide convective heat transfer enhancement (decrease) corresponding to positive (negative) ΔT.

This aspect is further confirmed by the well known concept of entropy generation minimization (Bejan, 2016) for heat transfer enhancement according to which the objective of convective heat transfer enhancement requires a minimization of $q''_w \cdot (T_w - T_{fluid})$. In present case the convective heat flux is constant thus to objective function to be minimized is $(T_w - T_b - \Delta T)$ which is minimized for maximum values of ΔT.

3.3 Dataset description

Recall that the non-dimensional parameters that govern the problem are the friction Reynolds number Re_τ and the Prandtl number Pr. The three cases discussed in the previous chapter are analyzed. The non-dimensional parameters of these cases are

1. $Re_\tau = 180$, $Pr = 0.7$.

2. $Re_\tau = 180$, $Pr = 4$.

3. $Re_\tau = 360$, $Pr = 0.7$.

For every case a snapshot dataset is obtained starting from 90 3D fields with a length of $25R$. The fields have a time separation greater than the eddy turnover length, i.e. $\Delta t^+ = 1.25R/u_\tau$ where $u_\tau \approx u_{bulk}/15$, i.e. in every subsequent time sample eddies have been convected about $18.75R$. From each field, 50 cross-plane slices have been extracted, with a separation of $0.5R$ between each pair of slices. The *snapshots* ensembles to be analysed are obtained from the mentioned slices. The temporal and spatial separation between the slices is assumed to be large enough to build a statistically significant dataset. The final dataset composed by the considered slices includes $N_t = 4500$ snapshots and has a spatial resolution of 69 and 100 points in the radial and azimuthal direction respectively.

3.4 Results and discussion

In the following both standard snapshot POD modes and extended POD modes are presented. For standard snapshot POD modes, the i^{th} eigenvalue of the snapshot correlation matrix, normalized with respect to the sum of all the correlation matrix eigenvalues is represented as σ_i^2 and represents the *energy* contribution of each POD mode to the total turbulent fluctuation of a given quantity (turbulent kinetic energy or temperature fluctuation variance). For what concerns the EPOD modes, their turbulent kinetic energy contribution is estimated from the sum of the square of the diagonal elements of the $\Sigma_{u_i,T}$ matrices and is normalized with respect to the sum of all the velocity correlation matrix eigenvalues. The contribution of EPOD modes to temperature fluctuations is instead expressed as the square of the elements of $\Sigma_{T,k}$ normalized with respect to the sum of the eigenvalues of the temperature correlation matrix.

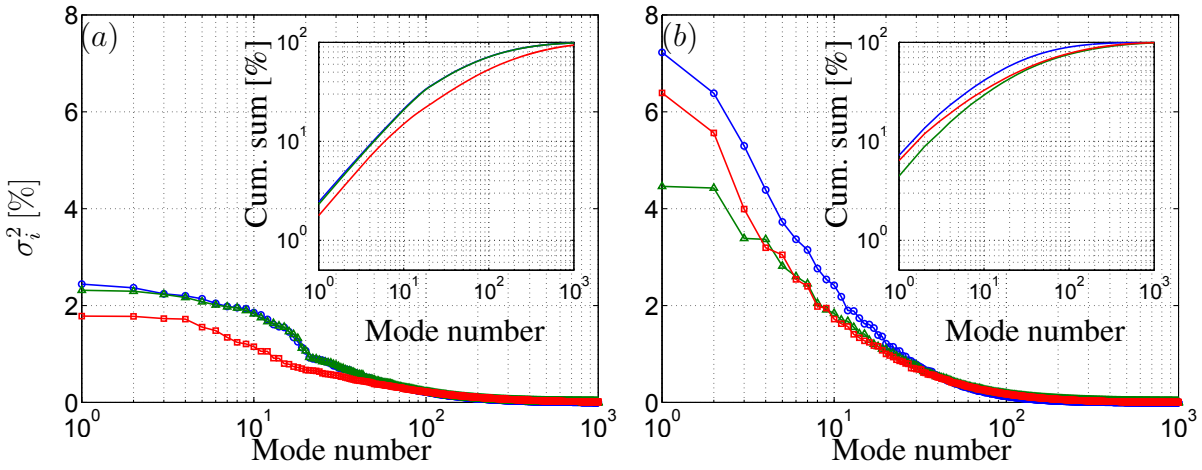

Figure 3.1: Energetic contribution of the POD modes. (a) Kinetic energy basis. (b) Temperature basis. The insets show the cumulative sum of the energetic contributions. Blue, case 1. Green, case 2. Red, case 3.

3.4.1 POD modes

The spectral contribution of velocity and temperature modes, optimal in sense of turbulent kinetic energy and temperature fluctuations respectively, is reported in figure 3.1. In agreement with the literature (Hellström & Smits, 2014), as shown in figure 3.1(a) the spectral contribution of the velocity modes to the turbulent kinetic energy is rather flat with the first mode accounting for about 2% of the turbulent kinetic energy. The first modes are slightly more energetic for the two cases at lower Reynolds number as a result of the greater spectral richness experienced in higher Reynolds number flows. The spectral contribution of temperature POD modes is reported in figure 3.1(b). Both the Prandtl and Reynolds numbers enhance the energy spreading over the modes spectrum;

in fact the first temperature mode accounts for more than 7% of the temperature variance for the case at $Re = 180$ and $Pr = 0.7$, about 6.5% for the case at $Re = 360$ and $Pr = 0.7$ and about 4.5% for the case at $Re = 180$ and $Pr = 4$. This results might be ascribed to the fact that both the increase of the Reynolds number and the increase of the Prandtl number cause the decrease of the thermal boundary layer thickness.

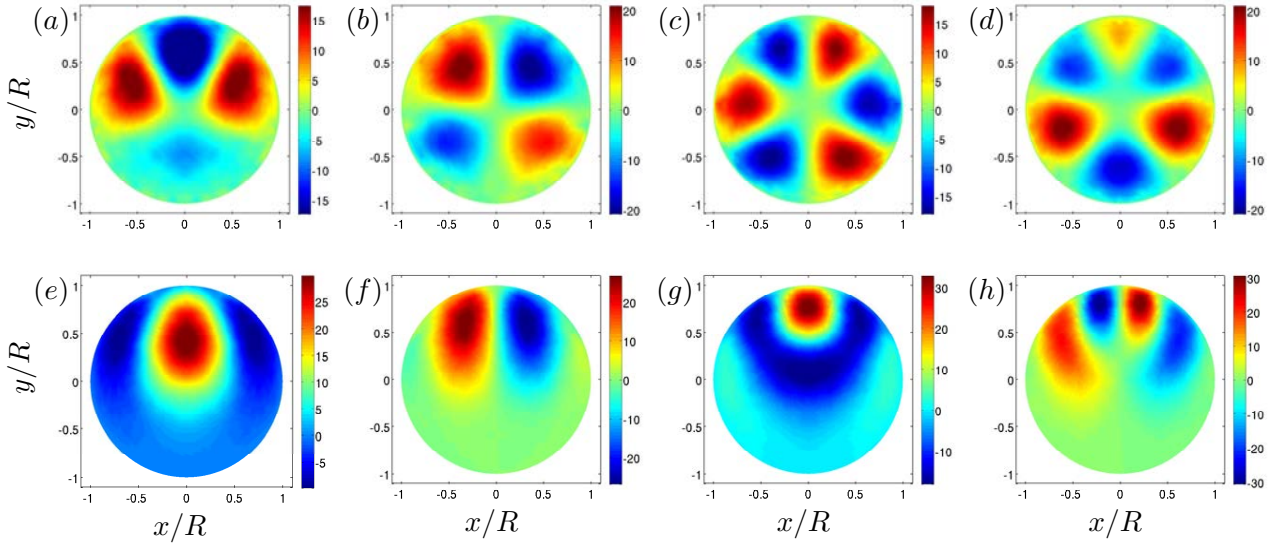

Figure 3.2: First four POD modes of case 3. (a)-(d) Modes of the kinetic energy basis, color represents axial velocity fluctuations. (e)-(h) Modes of the temperature basis, color represents temperature fluctuations.

As an illustration, the first four turbulent kinetic energy and temperature modes for case 3 are presented in figure 3.2. Velocity modes are in agreement with literature (Hellström & Smits, 2014): being the flow field statistically-homogeneous in the azimuthal direction and being the internal energy treated as a passive scalar, modes correspond to typical Fourier modes in the azimuthal direction. Note that there are some authors that make use of the azimuthal periodicity to decompose the POD modes by construction (Citriniti & George, 2000; Hellström *et al.*, 2015). When this is not done as in the present case, mode mixing might occur, as reported bu Hellström & Smits (2014). A mild mode mixing is observed for example in the modes 1 and 4 shown in figures 3.2(a) and (g). We have not enforced azimuthal periodicity by construction since the temperature POD modes do not present azimuthal symmetry, due to the non-homogeneous heat input. Instead, the heat input is symmetric with respect to the line $x = 0$, and the resulting temperature modes are either symmetric or antisymmetric with respect to this axis.

The first temperature mode, figure 3.2(e), contains a large scale temperature fluctuation in the upper part of the pipe, reaching beyond the thermal boundary layer. This might be connected with large scale motions in the outer region of the pipe, which are very energetic as has been shown by Guala *et al.* (2006). Indeed, the first few turbulent kinetic energy modes in figure 3.2 represent

large scale motions, while near wall motions are captured by high order modes (see figure 3 of reference Hellström & Smits (2014)). The temperature modes 2-4 (figure 3.2(f), (g) and (h)) can be interpreted as azimuthal and radial modulations of the first mode. In particular, the second mode can be seen as the azimuthal displacement of the temperature fluctuation in the first mode and the fourth mode provides a smaller wavelength azimuthal displacement. On the other side, the third mode can be seen as a radial shift of the first mode.

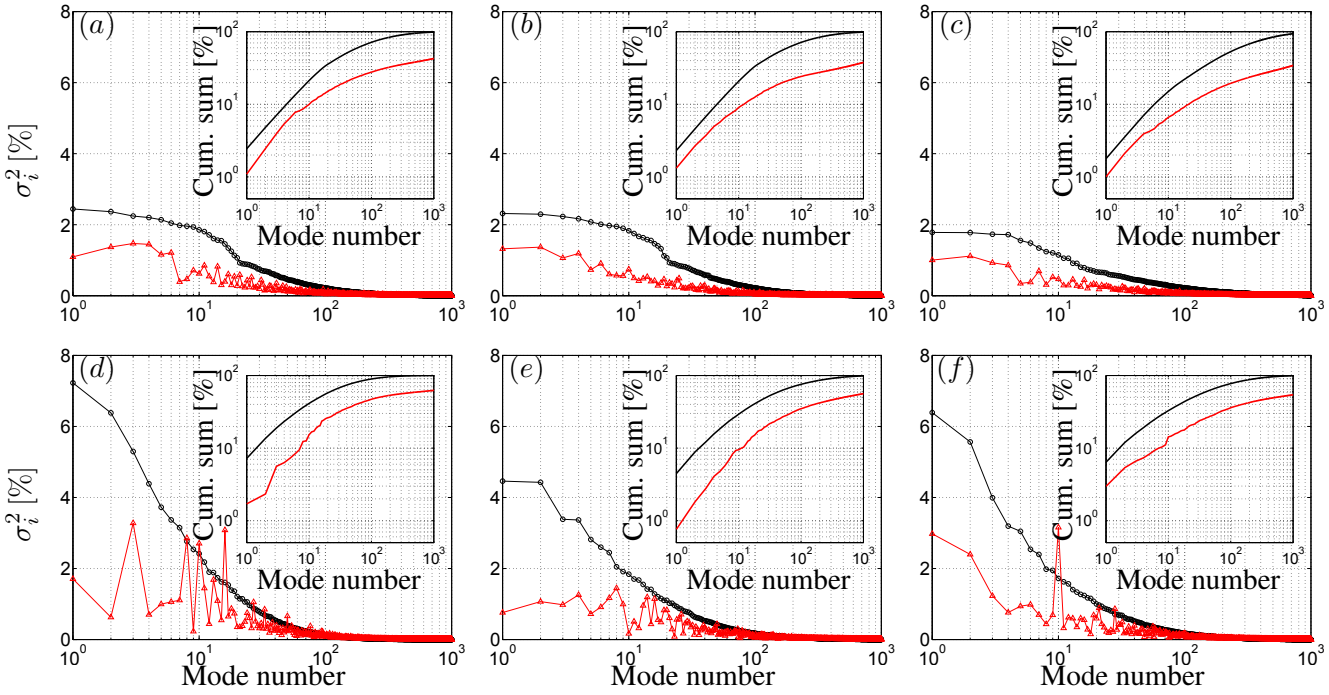

Figure 3.3: Energetic contribution of the POD and EPOD modes. $(a), (d)$ Case 1. $(b), (e)$ Case 2. $(c), (f)$ Case 3. $(a) - (c)$ Black line represents the contribution of the POD modes of the kinetic energy basis. Red line represents the kinetic energetic contribution of the EPOD modes of the temperature basis. $(d) - (f)$ Black line represents the contribution of the POD modes of the temperature basis. Red line represents the temperature variance contribution of the EPOD modes of the kinetic energy basis. The insets show the cumulative sum of the corresponding energetic contributions.

3.4.2 Extended POD modes

From the anaysis of the previous section, a main difference between the kinetic energy modes and the temperature modes is observed. While the former occupy the entire pipe section, the latter occupy mainly the upper part of the pipe, since the lower part of the pipe wall is adiabatic. Even if the temperature can be considered as a passive scalar, and it is therefore, mainly governed by the convection from the flow field, the kinetic energy modes do not provide a useful basis for the

temperature modes. However, the temperature temporal basis can be used, via the extended POD modes, to determine what velocity fluctuations are correlated to the temperature fluctuations.

Figure 3.3 shows both the POD and the EPOD modes energy contribution for all three cases. Figures 3.3(a)-c compare the energy contribution of the turbulent kinetic energy POD and EPOD modes (obtained from the temperature temporal basis). No significant differences are observed between the three cases considered. Overall, the EPOD mode contribution for the first few modes is roughly constant, and considerably smaller than the POD mode contribution (about one half). This is more evident from the observation of the cumulative sum in the corresponding inset that shows that with 1000 modes the POD mode contribution corresponds to about 99% while the EPOD mode contribution corresponds to roughly 40% of the total turbulent kinetic energy. This can be ascribed to the fact that the temperature temporal basis is biased towards events happening in the upper part of the pipe. Note also that the contribution from the EPOD modes presents oscillations, indicating that the EPOD modes are not ordered.

Figures 3.3(d)-(f) compare the energy contribution of the temperature POD and EPOD modes (obtained from the turbulent kinetic energy temporal basis). For the temperature modes, differences between the three cases are observed. All the EPOD curves exhibit a fluctuating behaviour, however, the peaks for case 1 (Figure 3.3(b)) and 3 (Figure 3.3(f)) are more marked than for case 2 (Figure 3.3(d)). For case 2, the energy contribution of any of the EPOD modes do not reach 2% and the higher energy content is reached in higher order modes such as mode 8 and 14. What is different in case 2 with respect to the other two cases is the Prandtl number ($Pr = 4$), so that the thermal boundary layer is thinner than the momentum boundary layer for case 2. This leads to a greater scale separation between the velocity and temperature fluctuation fields. Consequently, only higher order modes, containing velocity fluctuations at smaller wavelengths can be correlated with temperature fluctuations. For the other two cases, since $Pr = 0.7$, the two boundary layers are comparable in size. The EPOD mode contribution presents large spikes, since the modes are not ordered as discussed above. Some of the peaks represent an energy contribution greater than 3%, see for example mode 10 of case 3 in Fig. 3.3(f). This is due to the fact that the mode 10 of the turbulent kinetic energy basis is qualitatively similar to the mode 1 of the temperature basis (not shown). This similarity leads to a large energetic contribution for the EPOD mode 10 of the temperature from the kinetic energy basis.

Figures 3.4-3.7 show, for the three cases, the first four POD modes of temperature together with the corresponding EPOD modes of velocity. Contours of the axial velocity are provided together with vectors illustrating the flow in the cross-plane. For cases 1 and 3, with the same Pr, the first four POD temperature modes are esentially equivalent, with mild variations in intensity, Figures 3.4(a),(c)-3.7(a),(c). The shape of these modes was already discussed referring to Figure 3.2(e)-(h). The difference between these two cases is the Re number, and this parameter does not seem to affect significantly the first few temperature modes. This reflects the fact that the more energetic modes are related to the large-scale flow structures, which are rather similar for these two cases. The first four POD temperature modes are significantly different for case 2, with $Pr = 4$,

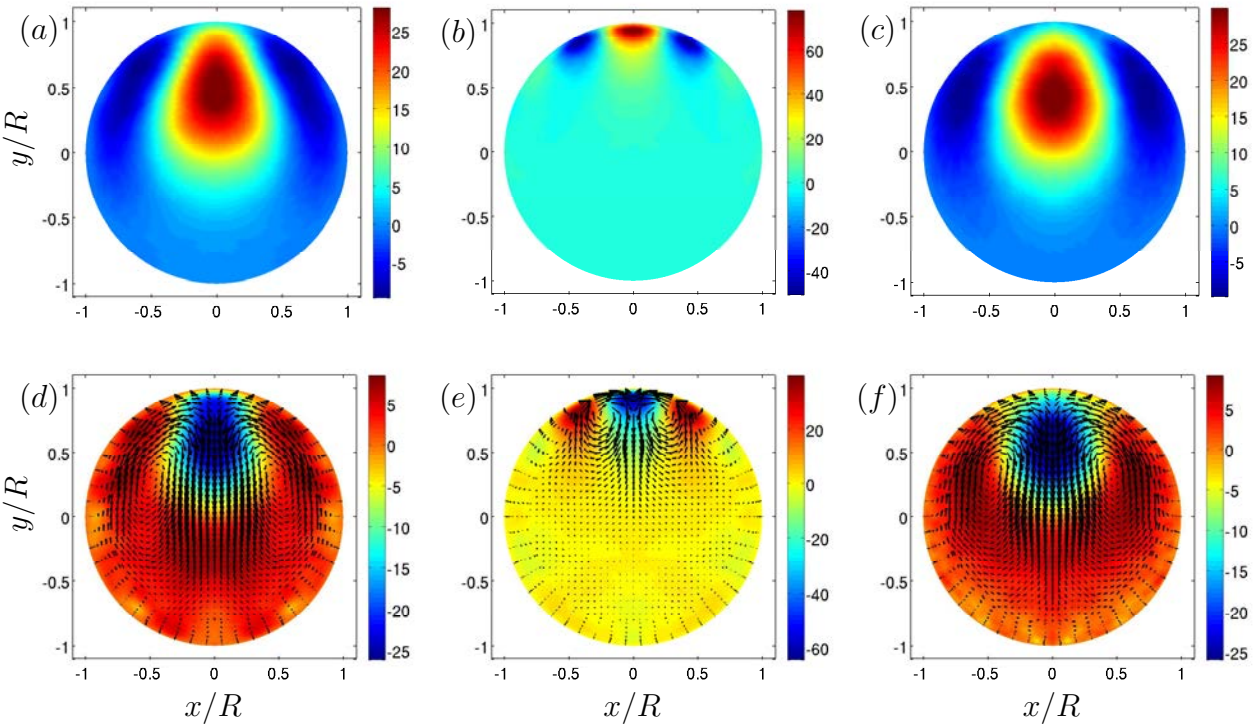

Figure 3.4: POD and EPOD Mode 1. $(a), (d)$ Case 1. $(b), (e)$ Case 2. $(c), (f)$ Case 3. $(a) - (c)$ Temperature POD mode on temperature basis. $(d) - (f)$ Velocity EPOD mode on temperature basis. Color represents axial velocity fluctuations, vectors represent cross-plane velocity fluctuations.

compared to cases 1 and 3, with $Pr = 0.7$. Thus, increasing Pr leads to POD temperature modes with fluctuations which occur closer to the top, Figures 3.4(b)-3.7(b). Note that increasing Pr the thermal boundary layer thickness becomes significantly thinner than the momentum boundary layer thickness and this might be connected to this observation.

The difference between the POD modes of velocity and the EPOD modes of velocity using the temperature basis is illustrated by comparing Fig. 3.2(a)-(d) to Figures 3.4(f)-3.7(f). As already mentioned, while the POD modes occupy the whole pipe, the EPOD modes are concentrated in the upper part, where the convective heat transfer is taking place. The combined analysis between a given temperature POD mode and its corresponding velocity EPOD mode leads to an improved understanding of the heat transfer mechanisms. For example the first mode of case 1, Fig. 3.4(a),(d), is formed by a low speed region in the upper part of the pipe flanked by two counter-rotating vortices so that hot fluid from above is transported downwards in the central part while cold fluid from below is transported upwards from both sides. This is a symmetric mode with respect to the $x = 0$ plane. The second mode on the other hand is antisymmetric, Fig. 3.5(a),(d). It is formed by a high speed region and a low speed region side by side in the upper part of the pipe, with a vortex in between them with a sense of rotation such that in the

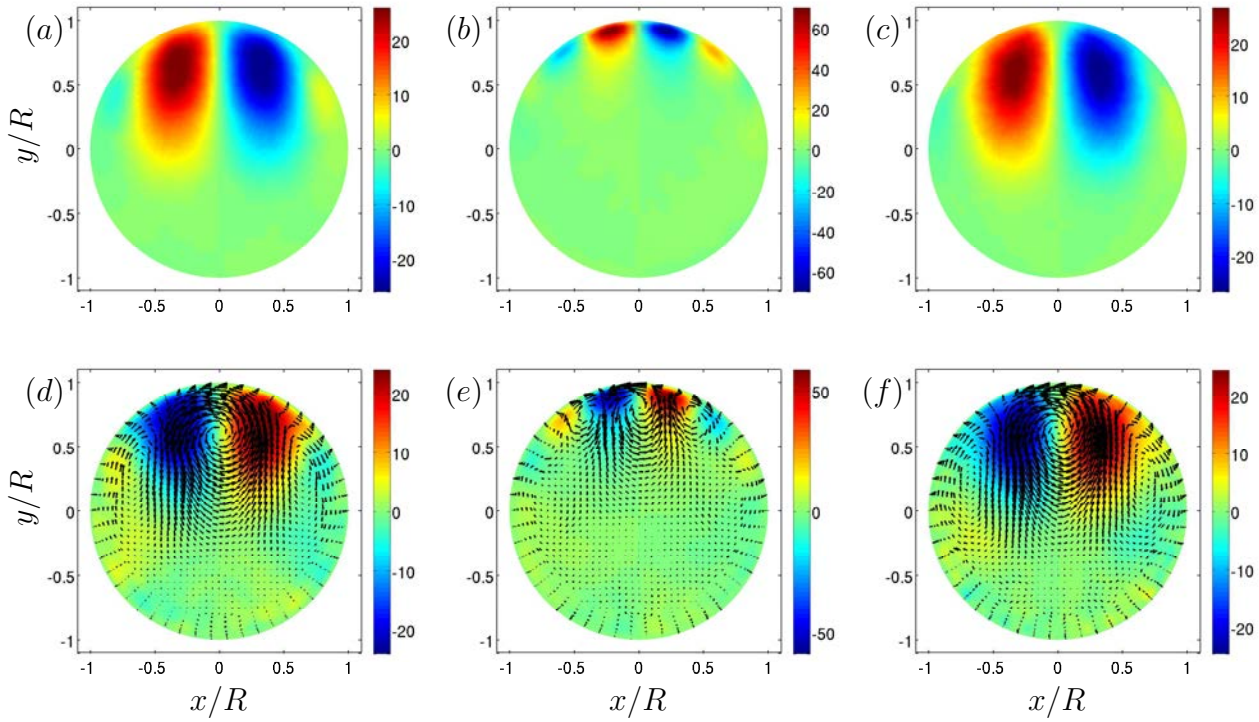

Figure 3.5: POD and EPOD Mode 2. $(a), (d)$ Case 1. $(b), (e)$ Case 2. $(c), (f)$ Case 3. $(a) - (c)$ Temperature POD mode on temperature basis. $(d) - (f)$ Velocity EPOD mode on temperature basis. Color represents axial velocity fluctuations, vectors represent cross-plane velocity fluctuations.

low (high) speed region, hot (cold) fluid is transported downwards (upwards) by the vortex. The remaining POD and EPOD modes shown in Figures 3.4-3.7 can be analyzed in similar terms. A more quantitative analysis is provided in the following section.

3.4.3 Turbulent heat flux in the vertical direction

In order to illustrate the utility of the POD-EPOD approach, in this section we consider the turbulent heat flux in the vertical direction. In the problem under consideration, heat is added to the system through the upper surface of the pipe $\theta \in (0, \pi)$ while the lower surface of the pipe $\theta \in (\pi, 2\pi)$ is adiabatic. The added heat is transported downwards, first by diffusive processes very near the wall and then by turbulent transport farther from the wall. Then, heat is transported in streamwise direction mainly by convection of the mean flow, leading to an increase of the bulk temperature along the pipe axis, as discussed above. For applications in which the turbulent heat transport plays an important role, it is interesting to analyze which flow structures contribute to the turbulent heat transport in the vertical direction. This can be done using the POD-EPOD approach.

First, the turbulent heat flux in the vertical direction $\langle v'T' \rangle$ for the three cases is shown in

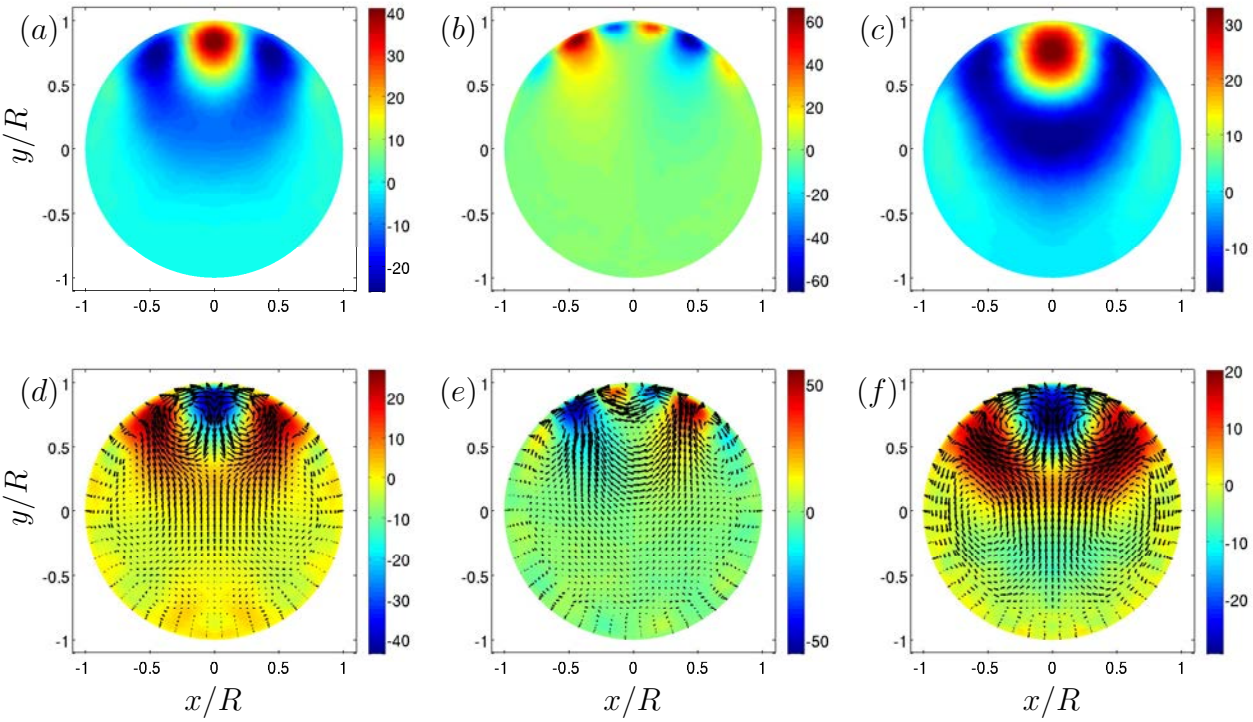

Figure 3.6: POD and EPOD Mode 3. $(a), (d)$ Case 1. $(b), (e)$ Case 2. $(c), (f)$ Case 3. $(a) - (c)$ Temperature POD mode on temperature basis. $(d) - (f)$ Velocity EPOD mode on temperature basis. Color represents axial velocity fluctuations, vectors represent cross-plane velocity fluctuations.

Figures 3.8(a)-(c). This quantity is normalized by $q''_{w,\text{max}}/(\rho c_p)$ where $q''_{w,\text{max}}$ is the maximum heat flux at the wall obtained from eq. (2.2). As obtained from the DNS, the spatial distribution of the heat flux is similar for all cases. The turbulent heat flux is mainly negative, since the heat is transported downwards and decays to zero at the wall, since v' vanishes at the wall. For the three cases, the turbulent heat flux is concentrated in the upper part of the pipe, and the heat flux contours have a kidney shape. This might be due to the fact that the streamwise velocity is maximum at the core, leading to a stronger heat convection in the streamwise direction in this region, as compared to the mid-region of the pipe. Small differences can be observed between the three cases. For example, for case 1, Fig. 3.8(a), the region near the top where the turbulent heat flux is close to zero is somewhat thicker than in the other two cases. This is because the thermal boundary layer is thicker in case 1 than in case 2 (that has a larger Pr) and than in case 3 (that has a larger Re). This also results in somewhat larger values of the heat flux in cases 2 and 3, compared to case 1. Since the turbulent heat flux is concentrated in the upper part of the pipe, we have selected two heights for further analysis, namely $y_1 = 0.5R$ and $y_2 = 0.8R$.

As mentioned in the previous section, the EPOD modes determine what velocity fluctuations are correlated to the temperature fluctuations. Therefore, we have reconstructed the temperature fields

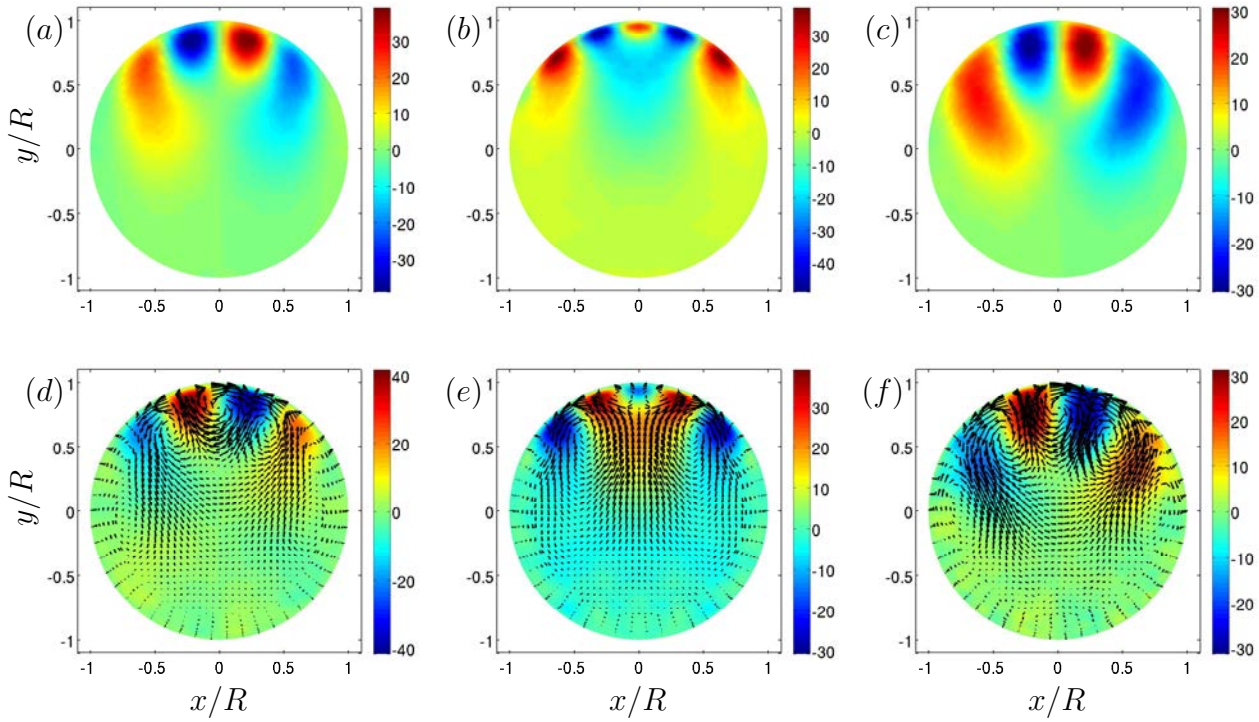

Figure 3.7: POD and EPOD Mode 4. $(a), (d)$ Case 1. $(b), (e)$ Case 2. $(c), (f)$ Case 3. $(a) - (c)$ Temperature POD mode on temperature basis. $(d) - (f)$ Velocity EPOD mode on temperature basis. Color represents axial velocity fluctuations, vectors represent cross-plane velocity fluctuations.

using the first N POD modes, $T_N(\underline{x}, t)$, and the vertical velocity fields using the corresponding N EPOD modes, $v_N(\underline{x}, t)$. Using these fields we compute a reconstructed turbulent heat flux $\langle v_N T_N \rangle$. Figure 3.8(d)-(f) shows the profile of $\langle v'T' \rangle$ at $y_1 = 0.5R$ for the three cases, together with the profiles of $\langle v_N T_N \rangle$ for $N = 4$, 16, 64 and 256. Figure 3.8(g)-(i) shows the corresponding profiles at $y_2 = 0.8R$. At both heights, already with 16 modes we recover at least half of the heat flux while with 256 modes the reconstruction has already converged for the profiles shown, namely $\langle v_{256} T_{256} \rangle \approx \langle v'T' \rangle$. For case 1, at both heights, with 64 modes the reconstruction is very good, while for cases 2 and 3 with 64 modes the reconstruction can still be improved. Note that, with a given reconstruction, it is possible to overpredict the value of the heat flux, as for example in case 2 at $y_2 = 0.8R$ with 64 modes, Fig. 3.8(h). This means that there are some modes beyond $N = 64$ that represent upwards heat flux so that in Fig. 3.8(h), the $N = 256$ reconstruction has converged to the actual value, as mentioned before.

In order to provide a more quantitative description of the heat flux reconstruction, we define an integral measure of the turbulent heat flux in the pipe. This can be easily done since everywhere

$\langle v'T' \rangle \leq 0$, and the integral

$$\Gamma = \int_0^R \int_0^{2\pi} \langle v'T' \rangle r \mathrm{d}r\mathrm{d}\theta, \tag{3.5}$$

is a meaningful quantity. We define Γ_N as the corresponding integral computed using $\langle v_N T_N \rangle$. Figure 3.9(a) shows for the three cases the ratio Γ_N/Γ (in %) as a function of the number of modes. This plot confirms that in case 1 ($Re_\tau = 180$,$Pr = 0.7$) less modes are required than in cases 2 ($Re_\tau = 180$,$Pr = 4$) and 3 ($Re_\tau = 360$,$Pr = 0.7$) to obtain a converged estimation of the turbulent heat flux in the whole domain, as already suggested by the profiles shown in Fig. 3.8. For $N < 10$, the contribution to the heat flux grows faster in case 3 than in case 2, however for $N > 10$ the trend reverses and it is the case 3 the one which requires more modes to obtain a converged estimation. For example, in case 3, 94% of Γ is obtained with 256 modes. In cases 1 and 2 the percentage achieved with 256 modes is 99.3 % and 96.4%, respectively.

It is also meaningful to compare the reconstruction of the heat flux, to the POD reconstruction of the temperature variance and the corresponding EPOD reconstruction of the turbulent kinetic energy. Therefore we define the integral measures of the temperature variance and the turbulent kinetic energy,

$$\Theta = \int_0^R \int_0^{2\pi} \langle T'T' \rangle r \mathrm{d}r\mathrm{d}\theta, \quad K = \frac{1}{2} \int_0^R \int_0^{2\pi} \langle u_i' u_i' \rangle r \mathrm{d}r\mathrm{d}\theta \tag{3.6}$$

and the corresponding POD, Θ_N, and EPOD, K_N, reconstructions. Figure 3.9(b) shows Γ_N/Γ as a function of K_N/K and as a function of Θ_N/Θ, for the three cases. It is remarkable that with 256 POD-EPOD modes more than 90% of the turbulent heat flux is recovered while the velocity fluctuations which are responsible for this turbulent transport only account to about 30% of the turbulent kinetic energy. This is explained by the fact that although turbulent velocity fluctuations are present overall in the pipe, only those which reach the upper part of the pipe are effective in transporting heat. It is also noteworthy that the POD-EPOD reconstruction seems to be somewhat more efficient in estimating the turbulent heat flux than the POD reconstruction in estimating the temperature variance. This can be seen in Figure 3.9(b), since for all three cases the line Γ_N/Γ vs. Θ_N/Θ is always slightly above the line $\Gamma_N/\Gamma = \Theta_N/\Theta$. This result might appear surprising since the POD modes are optimal in terms of the temperature variance. However it confirms the considerations discussed in §3.2.3 that a modal basis able to describe optimally the fluid temperature fluctuations is able to provide information about the flow structures that represent convective heat transfer.

3.5 Conclusions

We have analyzed the DNS database introduced in the previous chapter with the aim of identifying the motions responsible for the turbulent heat flux in the vertical direction. To this aim we have used a modal decomposition of instantaneous velocity and temperature fields in crossplanes based

on an extended proper orthogonal decomposition. Ee have shown that while standard POD modes of velocity are distributed over the whole pipe, extended POD modes of velocity are concentrated in the upper part of the pipe, where the vertical heat tranfer is taking place. The combined analysis of a given POD temperature mode and its corresponding EPOD mode of velocity provides insight on the physical mechanisms of heat transfer. The study of the first few modes has resulted in the identification of the cross-plane vortices responsible for bringing hot fluid from the top to the pipe core. The size of these vortices seems to depend on the ratio between the thermal boundary layer thickness and the momentum boundary layer thickness, so that they are strongly affected by the Prandtl number. Ee have reconstructed the temperature fields using POD modes and the vertical velocity fields using the corresponding EPOD modes. We have used these fields to compute a reconstructed turbulent heat flux in the vertical direction, finding that already with 16 modes we recover at least 50% of the total heat flux, while in all cases with 256 modes the reconstruction converges to the original heat flux. In addition, we have quantified the turbulent kinetic energy using the EPOD reconstructed velocity fields obtaining that with only 40% of the total turbulent kinetic energy we are able to reconstruct more than 95% of the turbulent heat flux in the vertical direction.

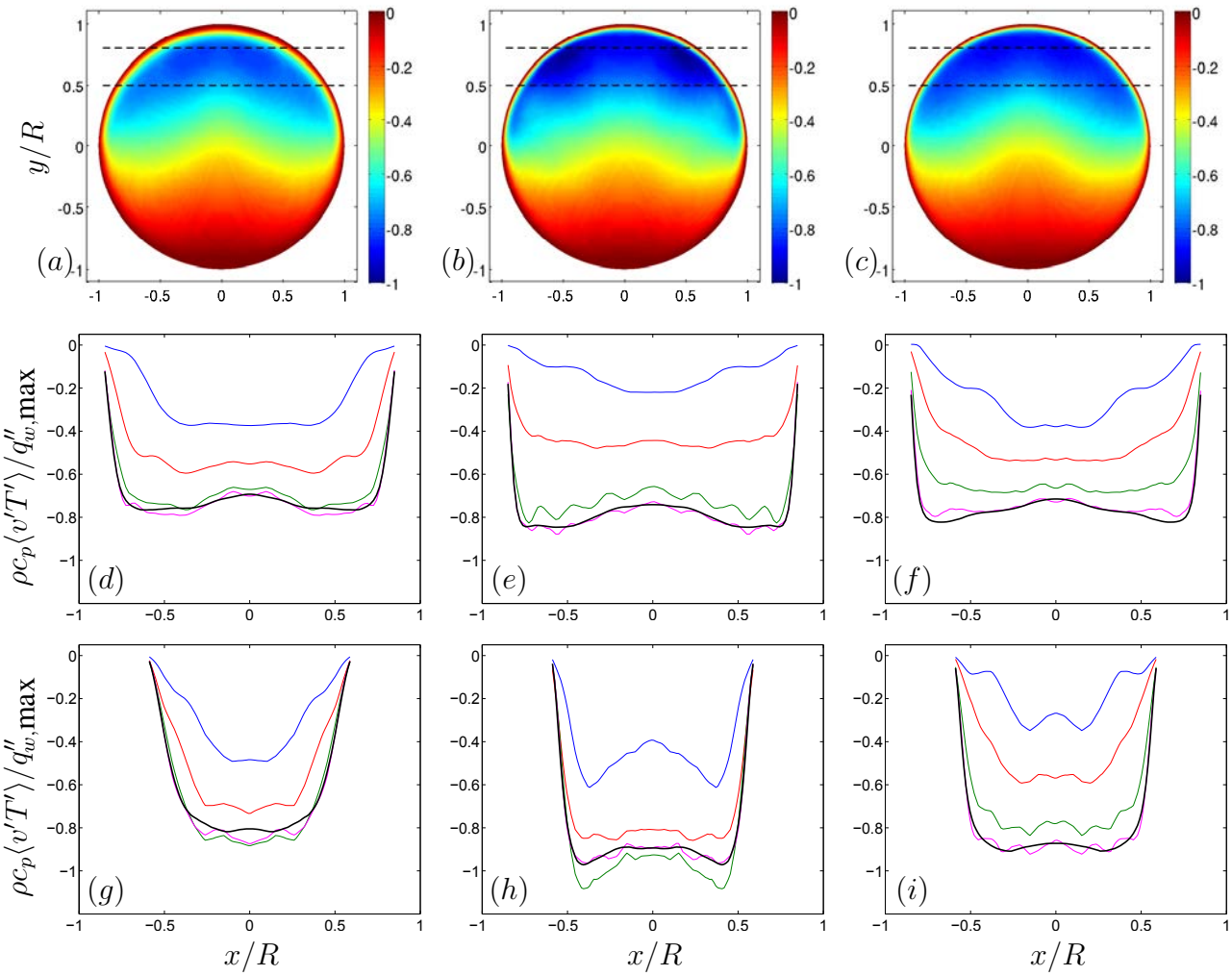

Figure 3.8: (a)-(c) Turbulent heat flux in the vertical direction $\rho c_p \langle v'T' \rangle / q''_{w,\text{max}}$ obtained from the DNS. The dashed lines indicate the two heights at which the profiles are computed. (d)-(f) Profiles of the turbulent heat flux in the vertical direction at $y/R = 0.5$. (g)-(i) Profiles of the turbulent heat flux in the vertical direction at $y/R = 0.8$. DNS data (black). POD-EPOD reconstruction of the heat flux using 4 modes (blue), 16 modes (red), 64 modes (green) and 256 modes (magenta). (a),(d),(g) Case 1. (b),(e),(h) Case 2. (c),(f),(i) Case 3.

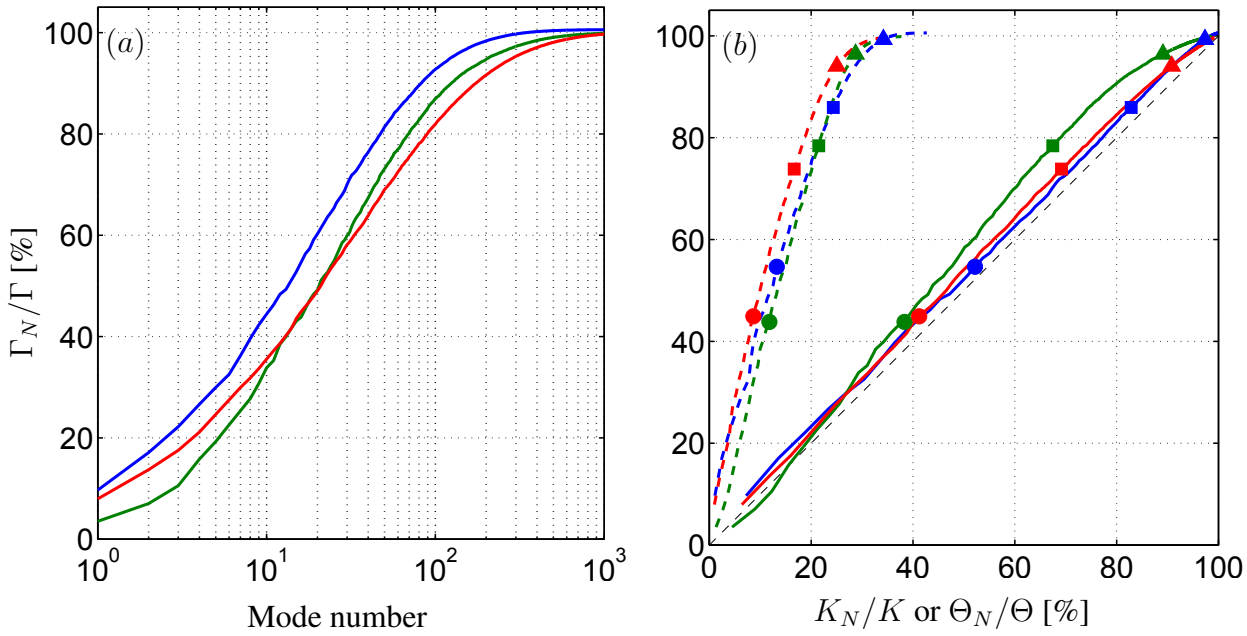

Figure 3.9: Integral measure of the turbulent heat flux reconstruction $\Gamma_N/\Gamma[\%]$ vs. (a) Number of modes, (b) Integral measure of the kinetic energy reconstruction $K_N/K[\%]$ (dashed lines) and of the temperature variance reconstruction $\Theta_N/\Theta[\%]$ (solid lines). Blue, case 1. Green, case 2. Red, case 3. Circles, $N = 16$ modes. Squares, $N = 64$ modes. Triangles, $N = 256$ modes. The dashed black line in (b) is the line $y = x$ which is provided for reference.

4 Influence of temperature-dependent fluid properties

This chapter reports the influence of having temperature-dependent fluid properties in a pipe with sinusoidal heat flux boundary conditions. Three cases with constant properties and with low and high sensitivity to temperature, the latter representative of a molten salt, are studied by means of DNS. The focus is on comparing the velocity and temperature fields from the perspective of the heat flux analysis. The effect of variable fluid porperties on the overall flow performance is quantified.

4.1 Introduction

In chapter 2, we made a first approximation to the problem of heat receivers studying the effect of circumferentially-varying heat flux conditions on the turbulent heat transfer in a pipe. The focus was on the influence of Reynolds and Prandtl numbers variations and on the improvement of eddy diffusivity models. The problem was however simplified by considering constant fluid properties.

In the present chapter we report the DNS results of a pressure-driven fully developed turbulent flow in a pipe with sinusoidal heat flux conditions and temperature-dependent viscosity and thermal diffusivity. The main objective is to study the influence of variable fluid properties on the mean values and turbulence statistics in the heat transfer fluid. To that end, three different conditions will be considereded: a case with a constant viscosity, a case with a percentual variation of viscosity with temperature similar to the characteristic values of the molten salts used in CSR, and an intermediate situation between these two cases.

Despite its industrial relevance, DNS of turbulent heat transfer in pipes are scarce compared to plane channel investigations. Numerical studies of pipe flow without heat transfer can be found in the papers of Eggels *et al.* (1994), Wu & Moin (2008), El Khoury *et al.* (2013) and Chin *et al.* (2014). DNS of heat transfer in pipes with *homogeneous* heating are available, for example, in the papers of Piller (2005) and Redjem-Saad *et al.* (2007). Except for the database created in chapter 2 and published in Antoranz *et al.* (2015), DNS of pipe flow with *circumferentially-varying* heat flux seem not to be available in the literature.

Reference articles for the study of *circumferentially-varying* heat flux are the experimental works of Black & Sparrow (1967) and Quarmby & Quirk (1972) and the RANS analysis of Reynolds (1963), Gärtner *et al.* (1974), Launder (1978) and Baughn *et al.* (1984), but in all of them fluid properties are considered uniform.

Regarding the studies on temperature-dependent fluid properties, the works of Zonta *et al.* (2012) and Lee *et al.* (2013), besides not being done for a pipe flow, are of application for the

our current analysis. Zonta *et al.* (2012) carried out DNS of a forced convection turbulent flow in a channel with anisotropic temperature-dependent viscosity and different channel walls temperatures. Lee *et al.* (2013) run DNS of a turbulent boundary layer over heated walls to investigate the effect of viscosity stratification. Both found a reduction of turbulence near the heated wall, where viscosity was lower.

The structure of this chapter is as follows. In section 4.2, the governing equations and the boundary conditions are presented. Section 4.3 describes the computational setup. Section 4.4 describes the cases of study. Results are presented and discussed in section 4.5. First, the circumferential distributions on the pipe wall are reported. Then we analyze the influence of varying fluid properties on the velocity and temperature statistics. This is followed by an attempt to collapse the mean profiles near the wall using the proper inner scaling. We focus then in the secondary flows created due to the non-isotropic fluid properties and their impact on the heat fluxes. Finally, the impact on the overall flow performance is quantified. The conclusions of the study are presented in section 4.6.

4.2 Governing equations

We present the study of a pressure-driven turbulent flow of a Newtonian fluid in a smooth circular pipe, subjected to a circumferentially-varying heat flux. The fluid has constant density, ρ, and specific heat, C_p, but temperature-dependent kinematic viscosity, ν, and thermal diffusivity, α. The equations solved are the Navier-Stokes equations for an incompressible fluid (continuity and momentum), together with an advection-difussion equation for the temperature (neglecting viscous energy dissipation). Energy and momentum equations are coupled by the viscosity variation with temperature. The resulting system of equations is

$$\frac{\partial u_i}{\partial x_i} = 0, \tag{4.1}$$

$$\frac{\partial u_i}{\partial t} + u_j \frac{\partial u_i}{\partial x_j} + \frac{1}{\rho}\frac{\mathrm{d}p}{\mathrm{d}x_i} = \frac{\partial}{\partial x_j}\left(\nu(T)\frac{\partial u_i}{\partial x_j}\right), \tag{4.2}$$

$$\frac{\partial T}{\partial t} + u_i \frac{\partial T}{\partial x_i} = \frac{\partial}{\partial x_i}\left(\alpha(T)\frac{\partial T}{\partial x_i}\right), \tag{4.3}$$

where repeated subindexes indicate summation (Einstein notation), $(x = x_1, y = x_2, z = x_3)$ are the three Cartesian coordinates and $(u_x = u_1, u_y = u_2, u_z = u_3)$ their corresponding velocity components.

Due to the geometry of the problem, we find also convenient the use of cylindrical coordinates (r, θ, z) and velocities (u_r, u_θ, u_z), where $z = x_3$ is the axial coordinate along the pipe axis (see figure 2.1 in Chapter 2).

The system of equations given in (4.1-4.3) is completed with appropriate boundary conditions on the wall: velocity is zero at the wall, and the wall-normal temperature gradient is given by an imposed sinusoidal heat flux distribution

$$q''_w(\theta) = \pi \overline{q}''_w \sin\theta = -\rho C_p \alpha(T) \left.\frac{\partial T}{\partial r}\right|_{r=R}. \tag{4.4}$$

Note that with this heat flux distribution, the pipe wall is heated on the upper part $(0 < \theta < \pi)$ with a net heat flux $\int_0^\pi q''_w(\theta)\, R d\theta = 2\pi R \overline{q}''_w$ entering the domain, but cooled on the lower part $(\pi < \theta < 2\pi)$ with a net heat flux $2\pi R \overline{q}''_w = -\int_\pi^{2\pi} q''_w(\theta)\, R d\theta$ leaving the domain. Thus, the net heat flux to the domain is null and, as a consequence, the volumed averaged temperature in the computational domain remains constant. Since the flow is then homogeneous along the z direction (axial), we can model that direction as periodic.

Several averages will be used throughout the paper. The brackets $\langle\cdot\rangle$ indicate mean values, averaged in time and over the homogeneous direction, z. Primed variables denote fluctuations with respect to these mean values. Bulk variables, denoted with a b subindex, are averaged in time, over the homogeneous direction z, and over the cross-plane area $\Omega(r,\theta)$. In particular, we will use the bulk velocity

$$U_b = \frac{1}{\pi R^2} \int_\Omega \langle u_z \rangle \, d\Omega, \tag{4.5}$$

and the bulk temperature

$$T_b = \frac{1}{\pi R^2 U_b} \int_\Omega \langle u_z T \rangle \, d\Omega, \tag{4.6}$$

which essentially is a mass weighted average of the temperature field.

The variation of the kinematic viscosity and the thermal diffusivity with temperature, $\nu(T)$ and $\alpha(T)$, is prescribed by the following power-laws,

$$\frac{\nu}{\nu_0} = \left(\frac{T}{T_0}\right)^{e_\nu}, \frac{\alpha}{\alpha_0} = \left(\frac{T}{T_0}\right)^{e_\alpha}, \tag{4.7}$$

where ν_0, α_0 and T_0 are constant reference values. The exponents e_ν and e_α are selected to represent the behavior of typical molten salts encountered in Solar Central Receivers (SCR) as discussed in section 4.4. For all the simulations presented here, we choose the initial mass averaged temperature to be equal to T_0. Hence, energy conservation implies that $T_b = T_0$. Note that, the same is not true for ν_b and α_b, which will depart from the reference values ν_0 and α_0 due to the power law dependence of eq. (4.7) with the temperature.

The equations of the problem can be normalized using the pipe radius, R, a reference velocity and a reference temperature. The reference velocity is the global friction velocity, $u_{\tau 0}$, defined as the mean friction needed to compensate the constant pressure-gradient driving the flow, $2\pi R \rho u_{\tau 0}^2 = \pi R^2 \langle dp/dz \rangle$. The reference temperature is the global friction temperature, $T_{\tau 0}$, defined by $\overline{q}''_w = \rho C_p u_{\tau 0} T_{\tau 0}$. With this characteristic length, velocity and temperature, the non-dimensional equations governing our problem depend only on the exponents e_ν and

e_α appearing in eq. (4.7), and three non-dimensional parameters: the global Reynolds number $Re_{\tau 0} = u_{\tau 0} R/\nu_0$, the global Prandtl number $Pr_0 = \nu_0/\alpha_0$ and the normalized temperature $T_0/T_{\tau 0}$.

Once the working fluid is selected (i.e., for constant e_α and e_ν), the influence of the variable fluid properties is mainly controlled by the magnitude of the parameter $T_0/T_{\tau 0}$. Except for large changes in the thermal diffusivity, α, which is not the case for molten salts nor for the present study, the temperature field is dominated by the heat flux boundary boundary condition. The friction temperature, $T_{\tau 0}$, is hence by definition indicative of the temperature variations, ΔT, in the domain. Because of the power-laws selected for the kinematic viscosity and the thermal diffusivity (eq. 4.7), their percent changes from their reference values are defined by the magnitude of the ratio $\Delta T/T_0$, which is of order $T_{\tau 0}/T_0$. With this in mind, we see that large values of the normalized reference temperature $T_0/T_{\tau 0}$ might produce small variations in the fluid properties, while the percent change of kinematic viscosity and the thermal diffusivity might increase when $T_0/T_{\tau 0}$ decreases.

4.3 Computational setup

Equations (4.1-4.3) are solved in non-dimensional form using the massively parallel code Nek5000, developed by Fischer *et al.* (2008). This code, as described in section 2.2 of Chapter 2, uses a spectral-element method (SEM), solving the incompressible Navier-Stokes equations on Gauss-Lobatto-Legendre nodes. The spectral-elements are hexahedral elements, where the fluid variables are discretized using a high-order orthogonal polynomials basis, which allows for spectral accuracy and geometrical flexibility. Time integration is performed with a 3rd order mixed Backward Difference/Extrapolation (BDF3/EXT3) scheme. The variable viscosity and diffusivity are implemented in Nek5000 using user-defined functions, which are called in every evaluation of the diffusive terms.

The computational domain consists of a circular pipe of length $25R$, as shown in figure 2.1. This distance is longer than in previous pipe computations for similar Reynolds conditions (Wu & Moin, 2008; Redjem-Saad *et al.*, 2007; Piller, 2005), and equal to the pipe length used by El Khoury *et al.* (2013). The domain is large enough to capture the maximum wavelength of the large scale motion which was found to be up to $16R$ (Wu & Moin, 2008). Since the axial direction, z, is homogeneous, periodic boundary conditions are used at the inlet and outlet of the pipe.

The same computational mesh is used for all the cases of study. We use a total of 55440 spectral elements of polynomial order $n = 7$, with 105 elements in the stream-wise direction and 528 elements in the cross-plane. The grid spacing is $\Delta r_{max} u_{\tau 0}/\nu_0 \leq 3.5$, $\Delta (R\theta)_{max} u_{\tau 0}/\nu_0 \leq 3.5$, $\Delta z_{min} u_{\tau 0}/\nu_0 \simeq 2.8$ and $\Delta z_{max} u_{\tau 0}/\nu_0 \leq 9$. The first grid point in the radial direction is located at $\Delta r_{min} u_{\tau 0}/\nu_0 \simeq 0.25$ from the wall. This resolution is slightly better than the DNS of turbulent pipe flow (without heat transfer) carried out by El Khoury *et al.* (2013) also using Nek5000. The computational time step selected for all cases is $\Delta t\, u_{\tau 0}/R = 0.00025$, which results in a Courant-

Case	$Re_{\tau 0}$	Pr_0	$T_0/T_{\tau 0}$	Line style
1	180	0.7	∞	Solid (Black)
2	180	0.7	1000	Dashed (Red)
3	180	0.7	500	Dashed-dotted (Blue)

Table 4.1: Parameters of the simulations. Case 1: Constant Fluid Properties, Case 2: Low Sensitivity to Temperature, Case 3: High Sensitivity to Temperature.

Friedrich-Levy number of $CFL \approx 0.5$.

The grid resolution and the prescription of the boundary conditions for the heat flow have been validated in previous works. In Gonzalo (2013), a case with uniform heat flux and constant fluid properties was compared with the results reported by Wu & Moin (2008) and Piller (2005), showing good agreement. In chapter 2 and also in the publication of Antoranz *et al.* (2015), we analyzed the heat transfer in a pipe flow with non-homogeneous heat flux in the circumferential direction, using the same computational mesh that is employed in the present simulations.

4.4 Description of cases

In this chapter, we consider the fully developed turbulent flow in a pipe with global friction Reynolds number $Re_{\tau 0} = 180$ and global Prandtl number $Pr_0 = 0.7$. Three cases with different reference temperatures, $T_0/T_{\tau 0}$, are selected to be representative of constant fluid properties or null sensitivity to temperature, $T_0/T_{\tau 0} \to \infty$, low sensitivity to temperature, $T_0/T_{\tau 0} = 1000$, and high sensitivity to temperature, $T_0/T_{\tau 0} = 500$. This cases are summarized in table 4.1. The sensitivity is indicative of the percent change experimented in the domain by the fluid variables from their values at reference conditions.

As mentioned before, the temperature-dependent fluid properties aimed to be representative of the characteristics of molten salts typically used in Central Solar Receivers (SCR). The data for the salt properties was obtained from the thorough review of Benoit *et al.* (2016) on heat transfer fluids in tube-receivers. Although all salt properties vary with temperature (see section 1.2 in chapter 1), we have only retained here the variation of the kinematic viscosity, $\nu(T)$ (the most sensitive), and the thermal diffusivity, $\alpha(T)$. Exponents selected to represent the behavior of typical molten salts in eq. 4.7 were $e_\nu = -3.0$ and $e_\alpha = +0.3$.

figure 4.1 shows the relative variation of the mean kinematic viscosity $\langle\nu\rangle$ and the mean thermal diffusivity $\langle\alpha\rangle$ as a function of the variability of $\langle T\rangle/T_0$ observed in our simulations.

Note that the power-laws selected generate asymmetric viscosity and diffusivity profiles, producing larger property variations at temperatures below T_0. For Case 3, with the lowest value of $T_0/T_{\tau 0}$, the percentage change of $\langle\nu\rangle$ is $[-30\%, +57\%]$ and of $\langle\alpha\rangle$ is $[-4.4\%, 3.5\%]$. For Case 2, with the intermediate value of $T_0/T_{\tau 0}$, the variation is of $[-17\%, 24\%]$ for $\langle\nu\rangle$ and of

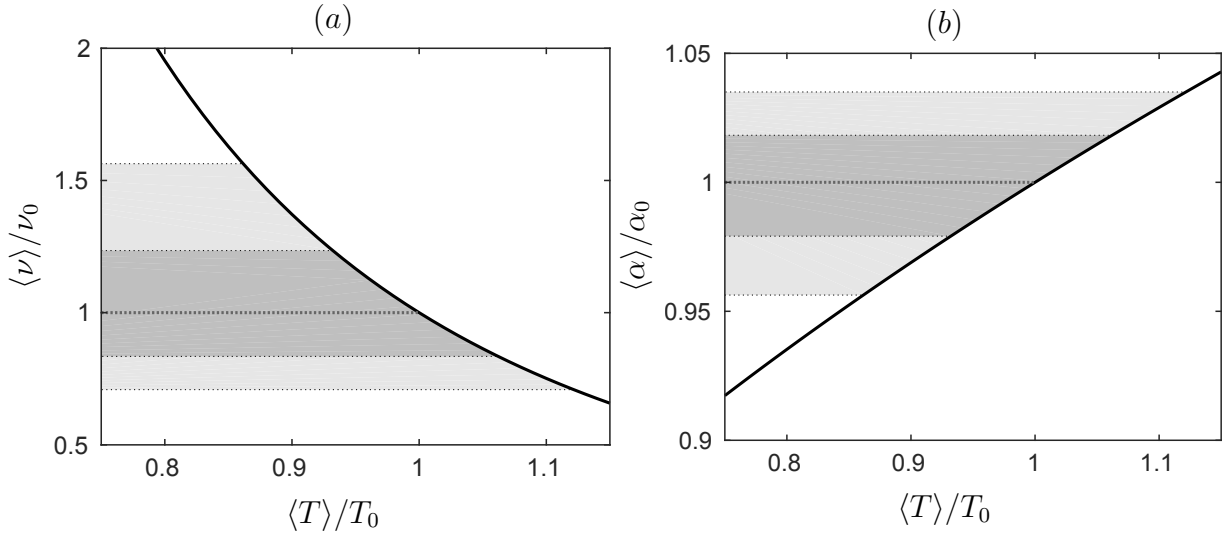

Figure 4.1: Variation of kinematic viscosity (a) and thermal diffusivity (b) with temperature. Shaded areas show range of change for current computations. Case 1: darkest grey line, Case 2: dark grey area, Case 3: light grey area.

$[-2.1\%, 1.8\%]$ for $\langle\alpha\rangle$. Case 3 is then designated as high sensitivity case and Case 2 is referred as low sensitivity case in table 4.1. Case 1 with constant properties has null sensitivity to temperature. Even though the heat flux on the pipe surface is kept the same for all cases, these variations in fluid properties affect the temperature field and heat transport in the domain. Computational results for the three cases are reported and discussed in the next section.

4.5 Results and discussion

The statistics for the different cases were accumulated for a time period of $t_{tot}\, u_{\tau 0}/R = 187.5$, which is roughly equal to 110 wash-out times. The results were averaged in time and in the axial direction. No advantage was taken from the symmetry of the problem so that the asymmetry in the plots below provide a measure of the convergence of the statistics.

4.5.1 Circumferential distributions on pipe wall

The circumferential distribution of temperature on the pipe wall is presented in figure 4.2 (a) for the three cases as the change from their corresponding bulk temperatures, $(\langle T_w\rangle - T_b)/T_{\tau 0}$. Case 1 shows an anti-symmetrical temperature distribution with peak amplitude $(\langle T_w\rangle - T_b)/T_{\tau 0} \sim 65$. When $T_0/T_{\tau 0}$ decreases and ν and α are allowed to vary, figure 4.2(a) shows that the wall temperature shifts to lower temperatures. The shift to lower temperatures is characterized in figure 4.2(b) by the difference in wall-temperature between the cases with variable properties (Cases 2

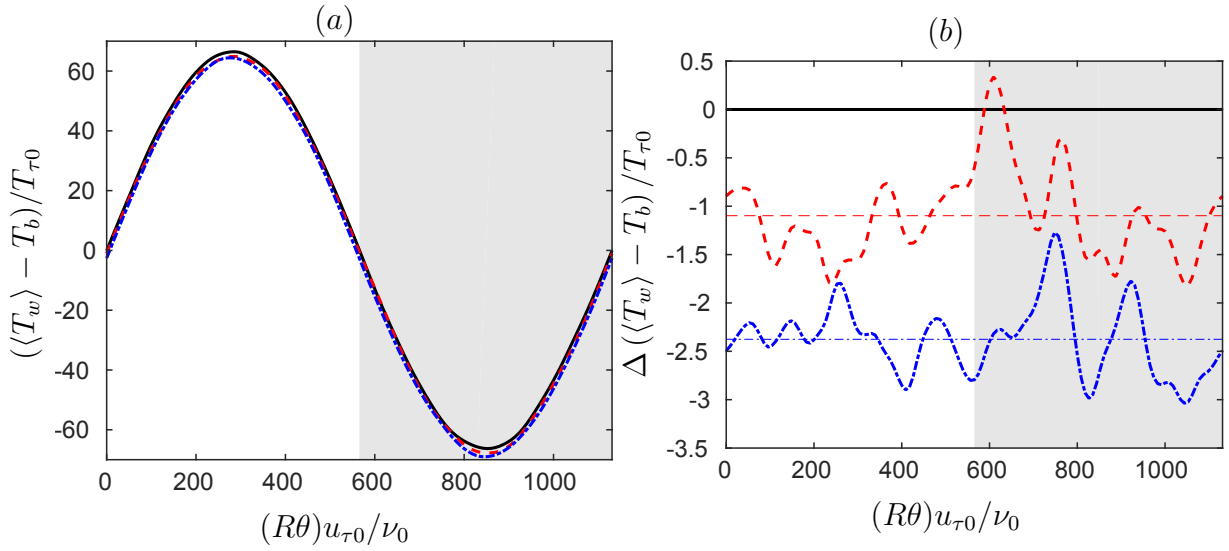

Figure 4.2: Circumferential variation of wall temperature minus bulk temperature at pipe wall (a) and increment from Case 1 (b). Shaded area indicates cooled half of the pipe. Lines are as described in table 4.1.Thinner lines present circumferentially averaged values.

and 3) and the case with constant properties (Case 1), $\Delta(\langle T \rangle_w - T_b)_i/T_{\tau 0}$, where

$$\Delta(\xi)_i = [\xi]_{case\ i} - [\xi]_{case\ 1} \tag{4.8}$$

$i = 2$ and 3. The oscillations we see in this variable are likely an effect attributable to lack of convergence of the statistics. The circumferential average of the normalized temperature difference shows that $(\langle T_w \rangle - T_b)/T_{\tau 0}$ for Case 2 is shifted by ~ -1.1, while Case 3 presents a shift of about ~ -2.4.

The wall temperature gradients are analyzed in figure 4.3. Since the heat flux is constant for all cases (eq. 4.4), the small change in temperature radial gradient at the wall (figure 4.3 (a)) is only produced by the slight variation of the thermal diffusivity $\langle \alpha_w \rangle$. Circumferential gradients (figure 4.3 (b)) are almost identical, consistent with the quasi-constant shift of the wall-temperature profile shown in figure 4.2(b). This suggests that, in the range of Reynolds and Prantdl numbers of the present study, the introduction of variable fluid properties has little or no effect in terms of additional thermal stresses in the pipe wall, which is one of the issues limiting the design of these heat transfer tubes (**?**).

The non-uniform temperature distribution produces a variation of the fluid properties, leading to non-homogeneous distribution of shear stress, $\langle \tau_w \rangle$, and hence, of the local friction velocity $u_\tau(\theta) = \sqrt{\langle \tau_w \rangle / \rho}$. The variation of the friction velocity with the circumferential position is provided in figure 4.4 (a). This velocity will be used in this paper to define a local inner scale for normalizing velocities and distances near the wall in section 4.5.4.

We also define a local friction temperature $T_\tau(\theta)$ as $q''_w(\theta) = \rho C_p u_\tau T_\tau$, whose distribution is provided in figure 4.4 (b). For Case 3, the friction velocity varies with respect to Case 1 fairly

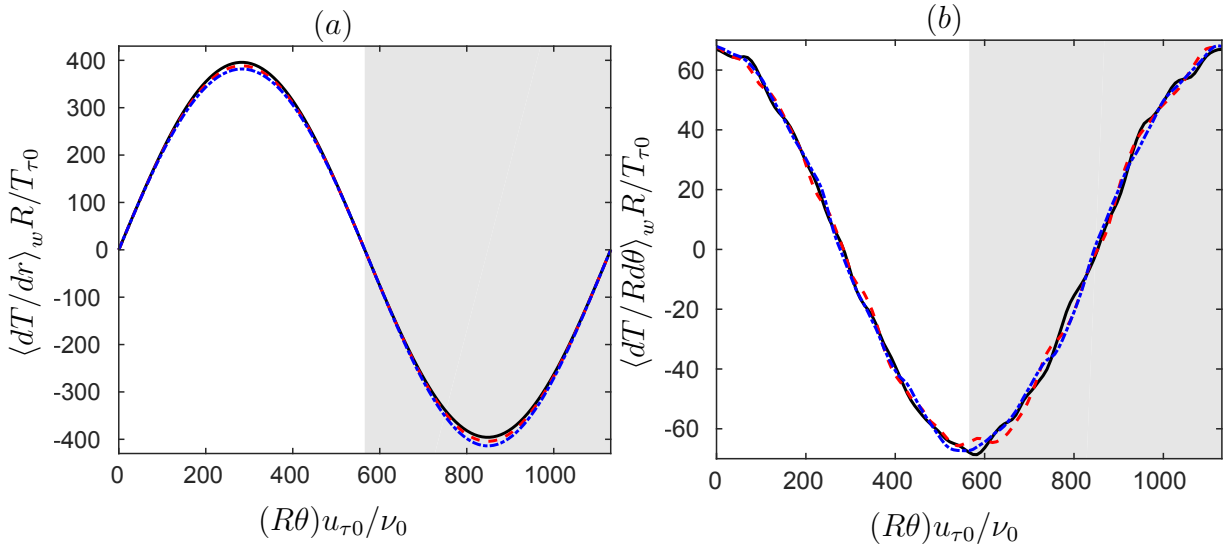

Figure 4.3: Circumferential variation of Radial Temperature gradient (a) and Circumferential Temperature gradient (b) at pipe wall. Shaded area indicates cooled half of the pipe. Lines are as described in table 4.1.

symmetrically from -6% in the hot side of the pipe to +6% in the cold side. The total change in u_τ for Case 2 is 5%. As a consequence, the local friction coefficient $C_f = 2u_\tau^2/U_b^2$ roughly changes 25% (10%) from top to bottom in Case 3 (Case 2). The percent variation of the friction temperature from the case with constant fluid properties is equal and of opposite sign to the the variation of $u_\tau/u_{\tau 0}$, since the thermal boundary condition implies $u_\tau(\theta)T_\tau(\theta) = u_{\tau 0}T_{\tau 0}\pi \sin\theta$ for all cases.

Circumferential variations of the wall values of kinematic viscosity, $\langle\nu\rangle_w$, and the thermal diffusivity, $\langle\alpha\rangle_w$, together with the local friction velocity, u_τ, result in non-homogeneous profiles for the local friction Reynolds number ($Re_{\tau,w} = u_\tau R/\langle\nu\rangle_w$) and local Prandt number ($Pr_w = \langle\nu\rangle_w/\langle\alpha\rangle_w$), which are plotted in figure 4.5. Changes are significant. The Reynolds number varies a 33% from the hot to the cold side of the pipe in Case 2, and a 66% in Case 3, ranging from $Re_{\tau,w} \sim 120$ to $Re_{\tau,w} \sim 240$ in the latter. Prandtl number changes from $Pr_w \sim 0.48$ to $Pr_w \sim 1.15$ in the most sensitive case, which means a 96% variation from the hot and cold sides of the pipe. This figure is reduced to 43% for Case 2. Finally, the local Péclet number, $Pe_{\tau,w} = Re_{\tau,w}Pr_w$, is reported in figure 4.5 (c). It takes a value of about $Pe_{\tau,w} \sim 115$ at the hot side of the pipe, and about $Pe_{\tau,w} \sim 140$ at the cold side for Case 3, when $Pe_{\tau,w} \sim 126$ for Case 1. As expected, the variation in the local Péclet number for Case 2 is smaller, roughly 120 to 132 from hot to cold sides of the pipe. Note that, while the local Reynolds number is increased (decreased) in the hot (cold) side of the pipe, the local Péclet number is decreased (increased). This suggests that while the thermal boundary layers are increased, the momentum boundary layers are decreased (and viceversa).

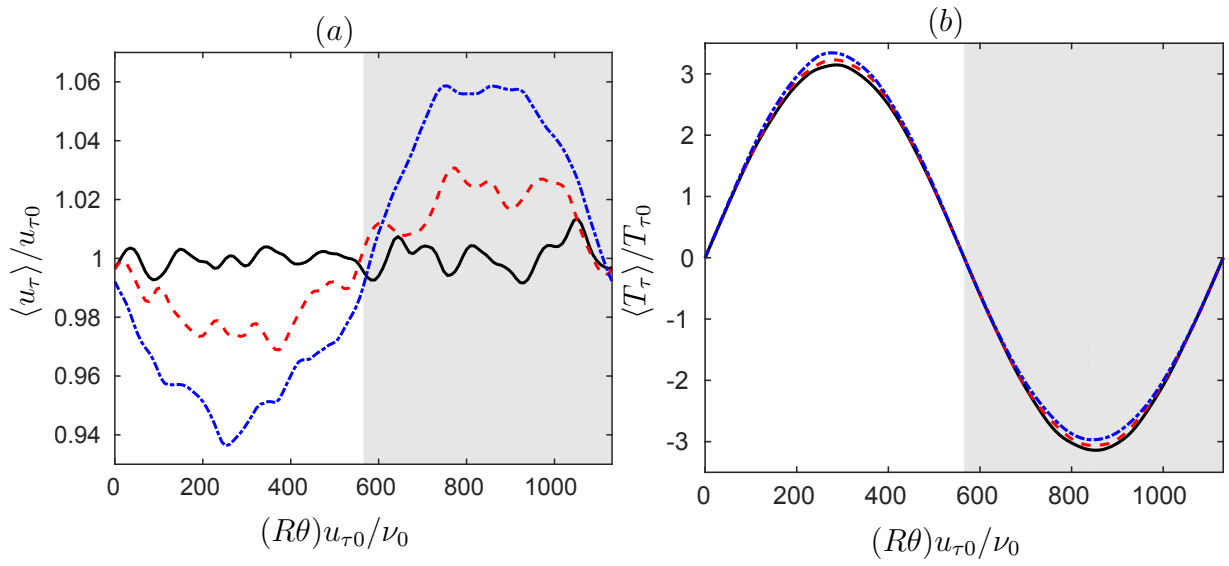

Figure 4.4: Circumferential variation of local Friction Velocity (a) and local Friction Temperature (b) at pipe wall. Shaded area indicates cooled half of the pipe. Lines are as described in table 4.1.

The local Nusselt number on the pipe wall is calculated as

$$Nu(\theta) = \frac{q_w}{\langle T_w \rangle - T_b} \frac{2R}{\rho C_p \langle \alpha \rangle_w}, \tag{4.9}$$

where q_w, $\langle T_w \rangle$ and $\langle \alpha \rangle_w$ are functions of the circumferential postion, θ. The circumferential profile of Nu is displayed in figure 4.6 (a). The distribution is singular at points where $\langle T_w \rangle = T_b$, which happens near $\theta = 0$ and $\theta = \pi$. We observe that, apart from these singularities, the Nusselt number is fairly constant over the heatead and cooled portions of the pipe wall, with values that depend on the local Reynolds and Prandtl numbers, as discussed later in section 4.5.6.

To finalize the discussion of the circumferential variation of the fluid variables at the pipe wall, figure 4.6 (b) shows the r.m.s. of the temperature fluctuations at the wall. As expected from a constant heat flux boundary condition, we find that the r.m.s. of the wall temperature is not zero at the wall, as opposed to cases with iso-thermal or mixed boundary conditions (Piller, 2005). The r.m.s. temperature fluctuations at the wall range from $T'_{rms}/T_{\tau 0} \sim 5.5$ to 7.7 and are maximum in the regions where the heat flux is more intense, $\theta = \pi/2$ and $\theta = 3\pi/2$. These fluctuations are largely influenced by the variable fluid properties. Moreover, they do not scale with $T_{\tau 0}$, nor with $T_\tau(\theta)$ for the three cases considered here. As $T_0/T_{\tau 0}$ decrease, the fluctuations at the heated side are mitigated, while they are exacerbated at the cooled side. For Case 3, we have a $+12\%$ increment in $T'_{rms}/T_{\tau 0}$ peak in the cold region compared to the case of constant fluid properties, while fluctuations are reduced by -7% at the hot top.

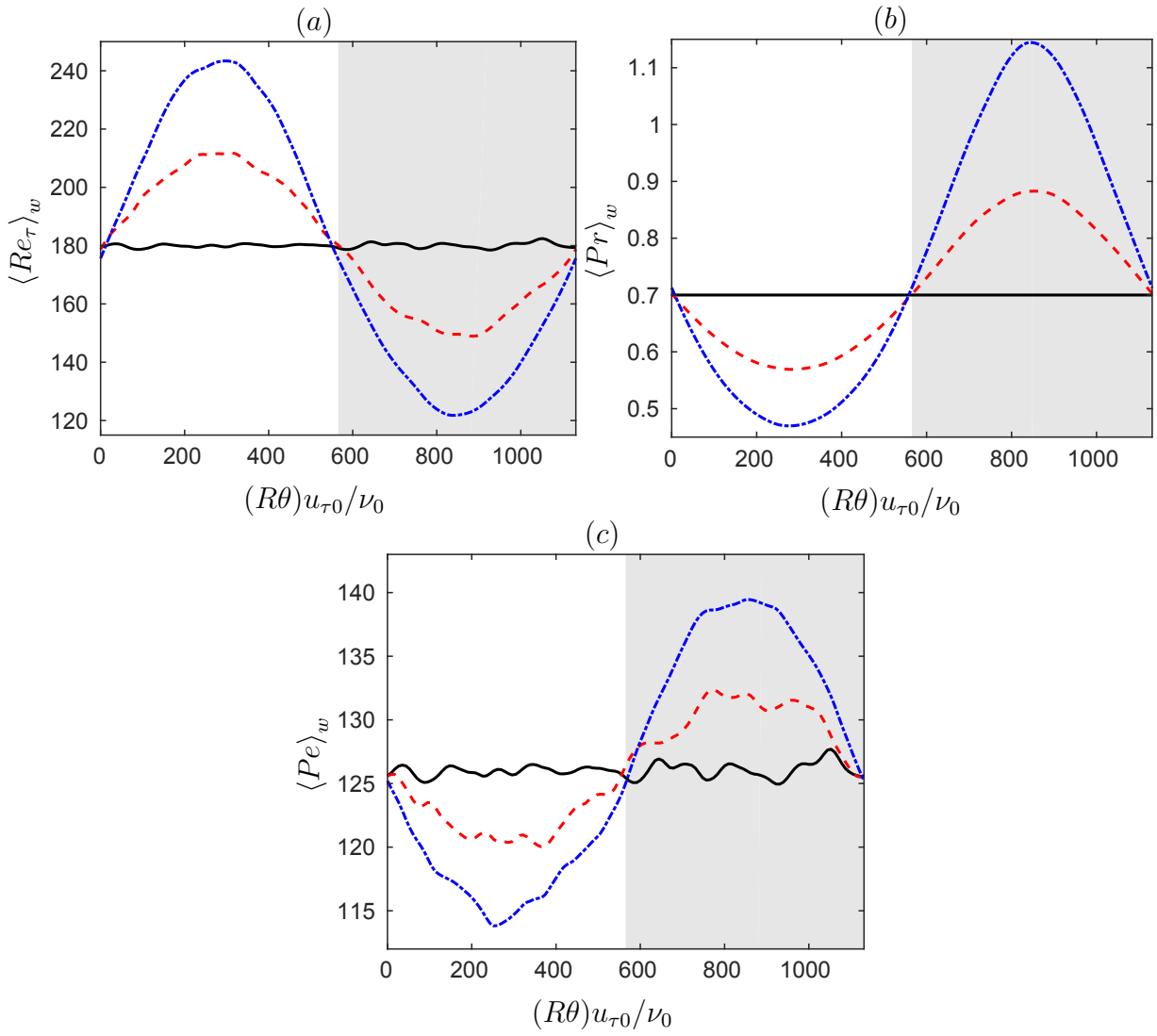

Figure 4.5: Circumferential variation of local friction Reynolds number (a), local Prandtl number (b) and local Péclet number (c) at pipe wall. Shaded area indicates cooled half of the pipe. Lines are as described in table 4.1.

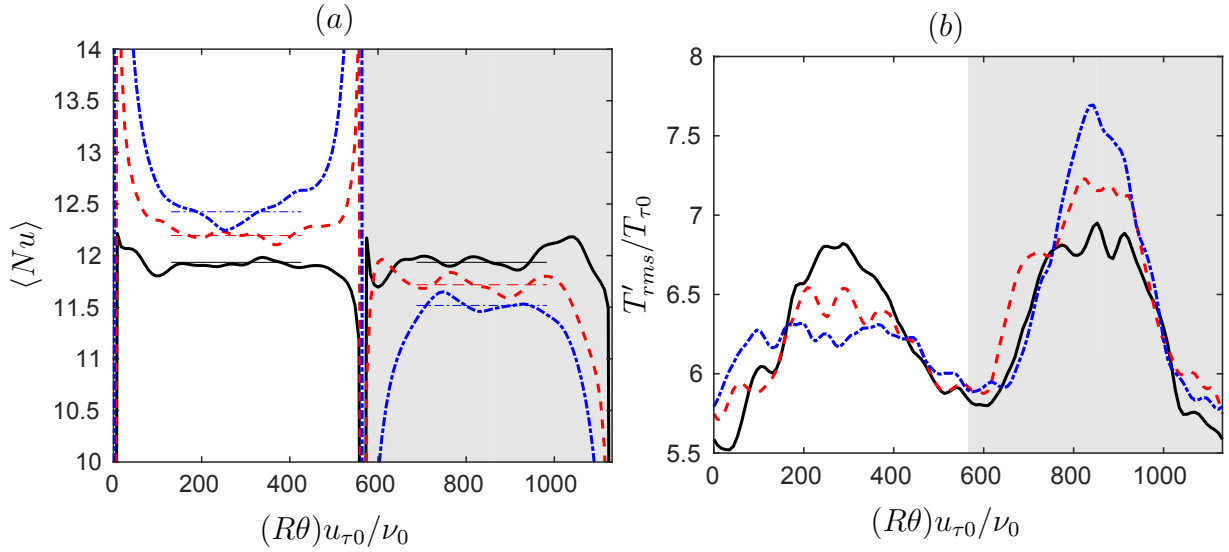

Figure 4.6: Circumferential variation of Nusselt number (a) and local r.m.s. temperature fluctuation (b) at pipe wall. Shaded area indicates cooled half of the pipe. Lines are as described in table 4.1.

4.5.2 Influence on Velocity Statistics

In this section we analyze the differences we find in the velocity components and their fluctuations due to the introduction of the temperature-dependent fluid properties.

Since the heat flux takes a top to bottom direction and the peak temperatures are reached at $\theta = \pi/2$ and $\theta = 3\pi/2$, we only show the radial distributions at those circumferential locations (i.e. flow distribution at the vertical diameter $x = 0$), because this is the location where differences are more apparent. Flow properties variation in the cross-plane are shown through the use of contour plots where the left half of the pipe corresponds to the case with constant properties (Case 1) and the right half belongs to the more sensitive case (Case 3), facilitating the comparison between the two cases.

In figure 4.7, the mean axial velocity profiles for the cases with variable fluid properties are compared with the case of constant properties. The insert shows the variations of $\langle u_z \rangle$ with respect to Case 1, namely $\Delta(\langle u_z \rangle)_i/u_{\tau 0}$. The mean axial velocity profiles tend to lose its symmetry when $T_0/T_{\tau 0}$ decreases as clearly seen in the insert. The velocity gradient becomes smaller near the cold half of the pipe, with a thicker boundary layer caused by the increased viscosity. The opposite is true for the heated half of the pipe, where the mean velocity profile for Case 3 shows a thinner boundary layer and a steeper gradient at the wall. Consistently, the Reynolds number is locally higher in the heated region as observed in figure 4.5.

Velocity fluctuations $u'_{z,rms}$, $u'_{r,rms}$ and $u'_{\theta,rms}$, as well as the turbulent kinetic energy (TKE), are compared in figures 4.8-4.11. We observe that the fluctuations are enhanced near the cold bottom, where the mean velocity gradient is reduced, while the opposite occurs in the hot side.

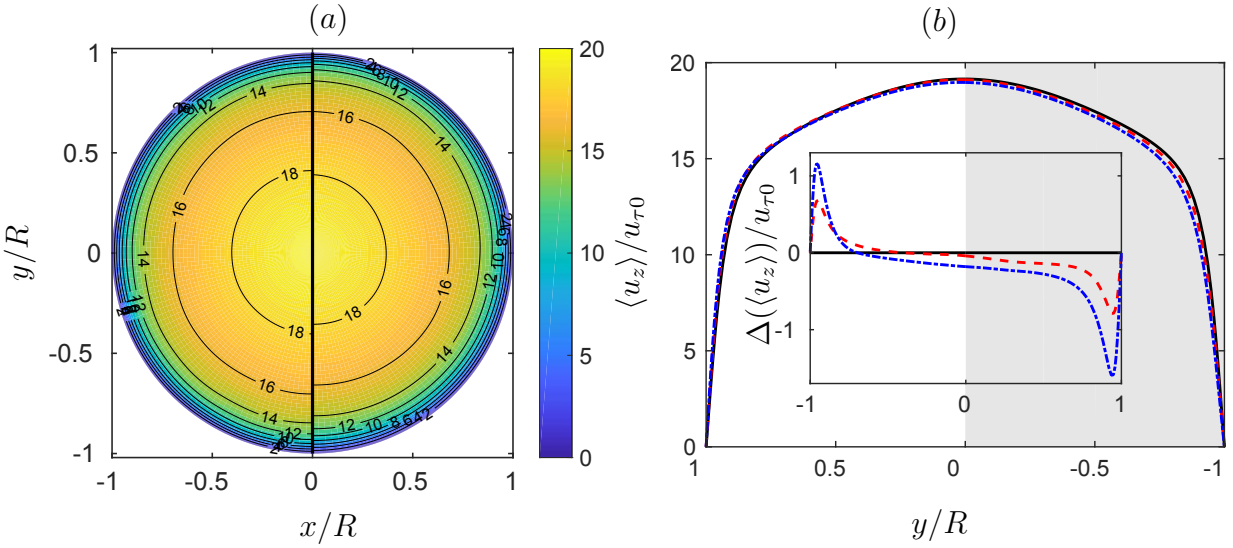

Figure 4.7: Mean axial velocity ($\langle u_z \rangle / u_{\tau 0}$) comparison. (a) Case 1 field (left) is compared with Case 3 field (right). (b) Top-bottom profile comparison. Shaded area indicates cooled half of the pipe. Lines are as described in table 4.1.

Note also that the position of the peak r.m.s. moves closer to the pipe wall as the mean velocity gradient increases. While the latter is the expected behavior in incompresible wall-turbulent flows, the increased r.m.s. for the reduced velocity gradients are not. However, the behavior shown in figures 4.8-4.11 is consistent with the results of Zonta *et al.* (2012), who attributed this effect to a de-stabilizing effect of an increased viscosity, as suggested by Sameen & Govindarajan (2007). There is however another possibility, related to the changes of the local friction velocity and local viscosity with respect to the reference values (i.e. $u_\tau 0$ and ν_0), which is explored later in subsection 4.5.4.

A similar behavior is also observed in the turbulent shear stress $\langle u_r' u_z' \rangle / u_{\tau 0}^2$ for the three cases (figure 4.12). While Case 1 maintains a symmetrical profile, in Case 3, the peak value decreases near the hot part roughly -6.3% but increases near the cold part by approximately $+10\%$, indicating higher stress-producing events (Zonta *et al.*, 2012).

4.5.3 Influence on Temperature Statistics

The profile of the difference between the mean temperature and the bulk temperature normalized with the global friction temperature, $(\langle T \rangle - T_b)/T_{\tau 0}$, is shown in figure 4.13. The temperature distribution in the cross-plane is dominated by the heat flux boundary condition on the wall. Highest mean temperature is reached at the top where the heat flux is maximum and lowest mean temperature is found at the bottom where the heat flux is more negative. Although the profiles for the three cases are similar, the local variation in Prandtl number produces an effect on the thermal boundary layers near the pipe wall. figure 4.14 (a) provides with the temperature increment in Cases 2 and

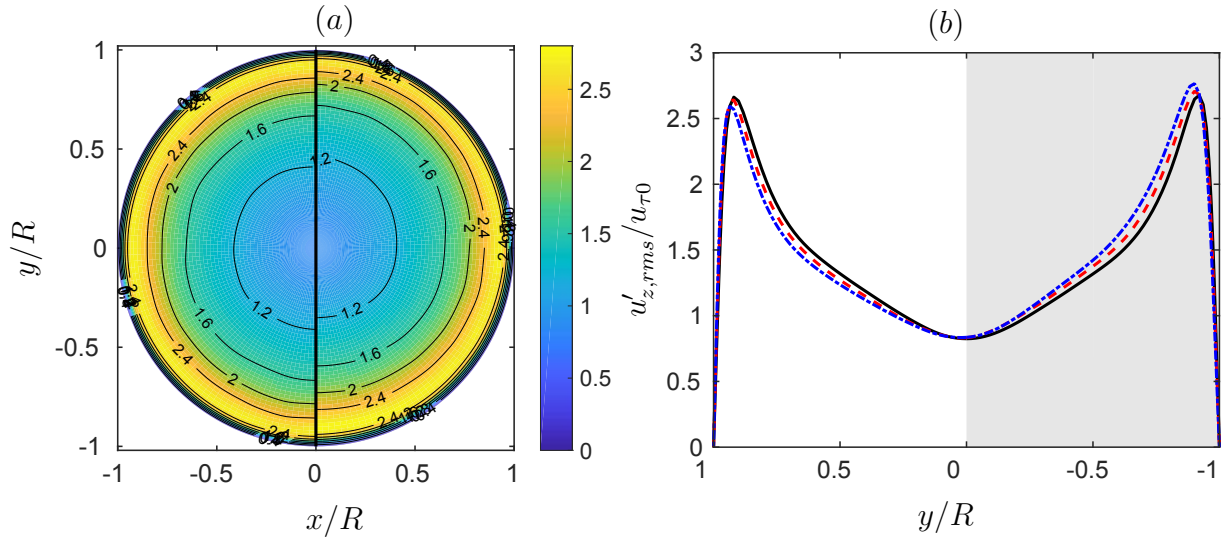

Figure 4.8: Root mean square of axial velocity fluctuations $\left(u'_{z,rms}/u_{\tau 0}\right)$ comparison. (a) Case 1 field (left) is compared with Case 3 field (right). (b) Top-bottom profile comparison. Shaded area indicates cooled half of the pipe. Lines are as described in table 4.1.

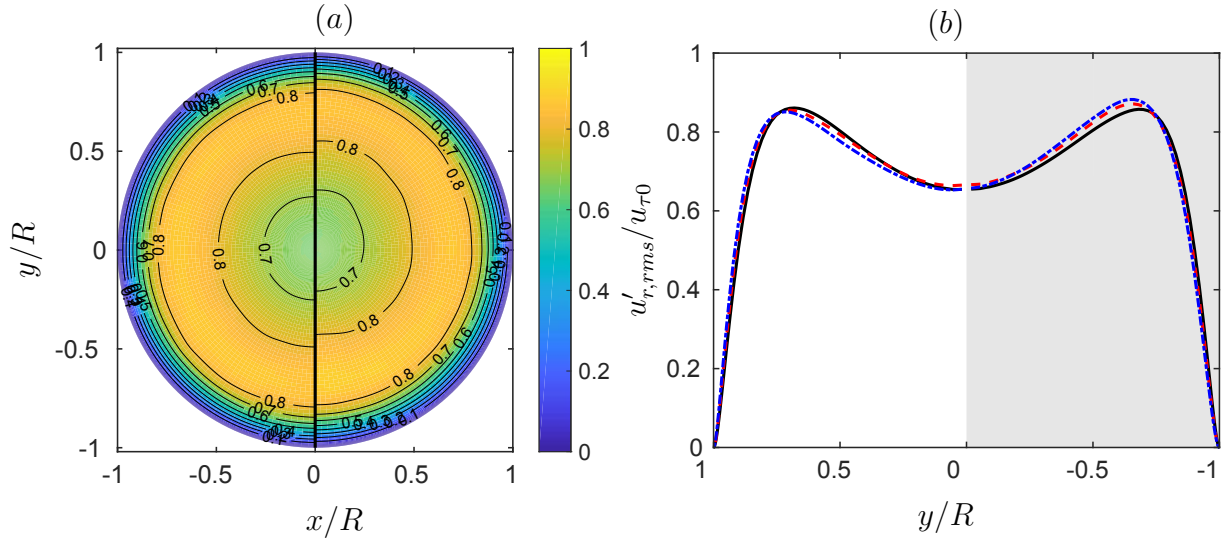

Figure 4.9: Root mean square of radial velocity fluctuations $\left(u'_{r,rms}/u_{\tau 0}\right)$ comparison. (a) Case 1 field (left) is compared with Case 3 field (right). (b) Top-bottom profile comparison. Shaded area indicates cooled half of the pipe. Lines are as described in table 4.1.

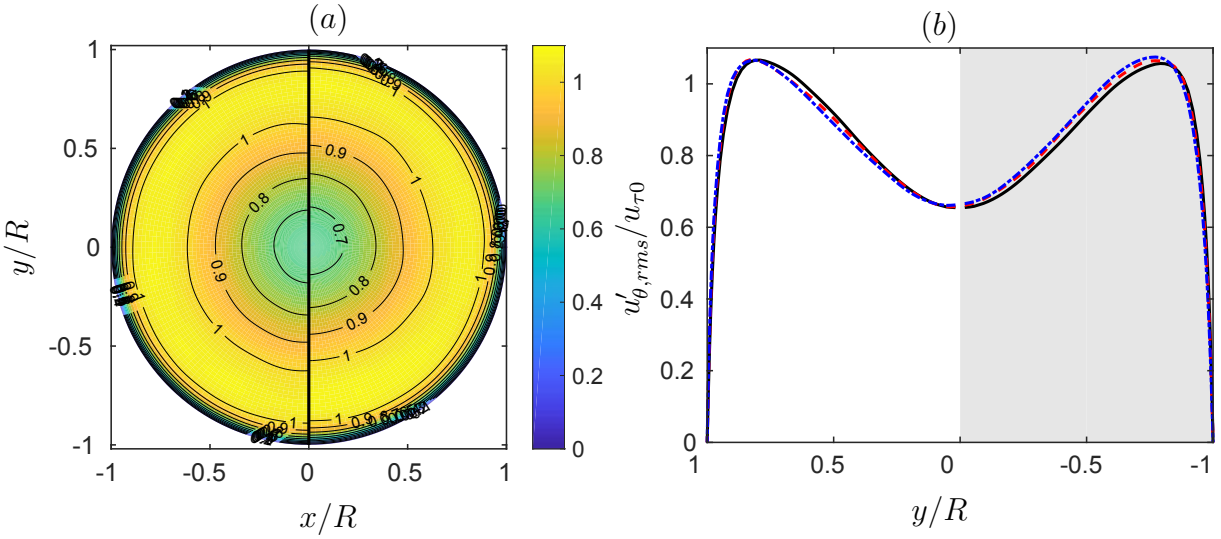

Figure 4.10: Root mean square of circumferential velocity fluctuations $\left(u'_{\theta,rms}/u_{\tau 0}\right)$ comparison. (a) Case 1 field (left) is compared with Case 3 field (right). (b) Top-bottom profile comparison. Shaded area indicates cooled half of the pipe. Lines are as described in table 4.1.

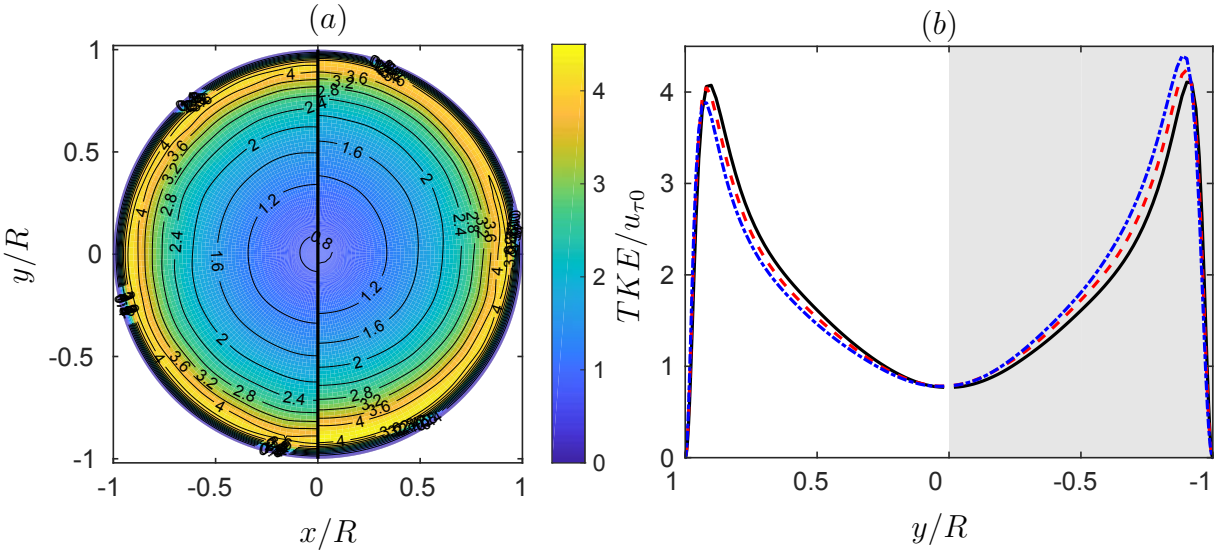

Figure 4.11: Turbulent kinetic energy profiles, $TKE = 1/2\langle u'^2 + v'^2 + w'^2\rangle/u_{\tau 0}^2$. (a) Case 1 field (left) is compared with Case 3 field (right). (b) Top-bottom profile comparison. Shaded area indicates cooled half of the pipe. Lines are as described in table 4.1.

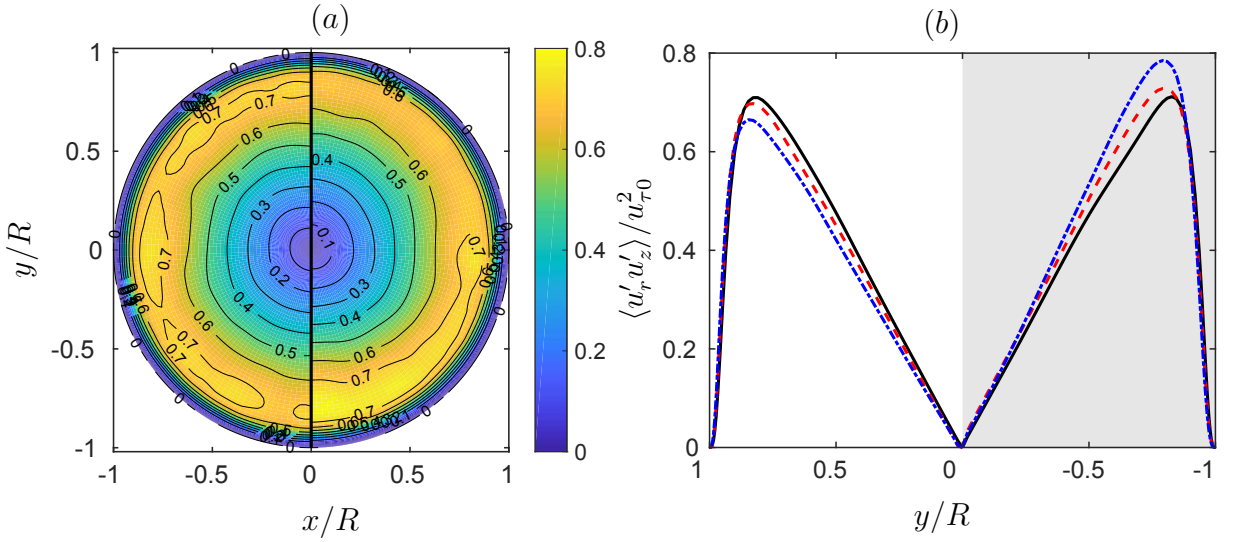

Figure 4.12: Turbulent shear stress ($\langle u_r' u_z' \rangle / u_{\tau 0}^2$) comparison. (a) Case 1 field (left) is compared with Case 3 field (right). (b) Top-bottom profile comparison. Shaded area indicates cooled half of the pipe. Lines are as described in table 4.1.

3 with respect to the temperature obtained for Case 1. We distinguish a central region where the temperature changes linearly from top to bottom with equal slope for the three cases, with Case 2 being shifted towards higher normalized temperatures by $\sim +0.7$ and Case 3 by $\sim +1.7$. Close to the wall the behavior is different and the cases with variable properties have lower temperatures, consistent with the discussion of the temperature profile on the wall (figure 4.2).

Figure 4.14 (b) shows the temperature gradient in the vertical direction $\langle dT/dy \rangle$ for the top-bottom profile. The inserts highlight the differences on the gradient very close to the wall. At the cold bottom, Case 3 presents a slightly steeper gradient of the mean temperature, corresponding with a higher local Péclet number, Pe_w. The opposite happens at the heated half of the pipe, where the temperature gradient is smaller.

Figure 4.15 reports the r.m.s. temperature fluctuations in the cross-plane and on a vertical diameter of the pipe. Near the walls, the behaviour of the temperature r.m.s. is qualitatively similar to the behaviour of the velocity fluctuations, TKE and Reynolds stresses. Fluctuations are promoted near the cooled wall, but damped near the heated wall. Note that these tendencies are consistent with the changes in the mean temperature gradients. For the cooled part of the wall pipe in Case 3 (Case 2) there is a $+8.8\%$ ($+4.1\%$) increment in the peak of $T'_{rms}/T_{\tau 0}$ corresponding to a local Prandtl number of $Pr_w \sim 1.15$ (0.88). At the other end of the pipe, in the heated wall, the peak of $T'_{rms}/T_{\tau 0}$ decreases -7.2% (-3.9%) for Case 3 (Case 2) with a local Prandtl number of $Pr_w \sim 0.47$ (0.58). This behavior seems to be in agreement with the findings reported by Redjem-Saad *et al.* (2007) in DNS of turbulent flow in pipes with uniform heat flux and constant fluid properties, for different Prandtl numbers.

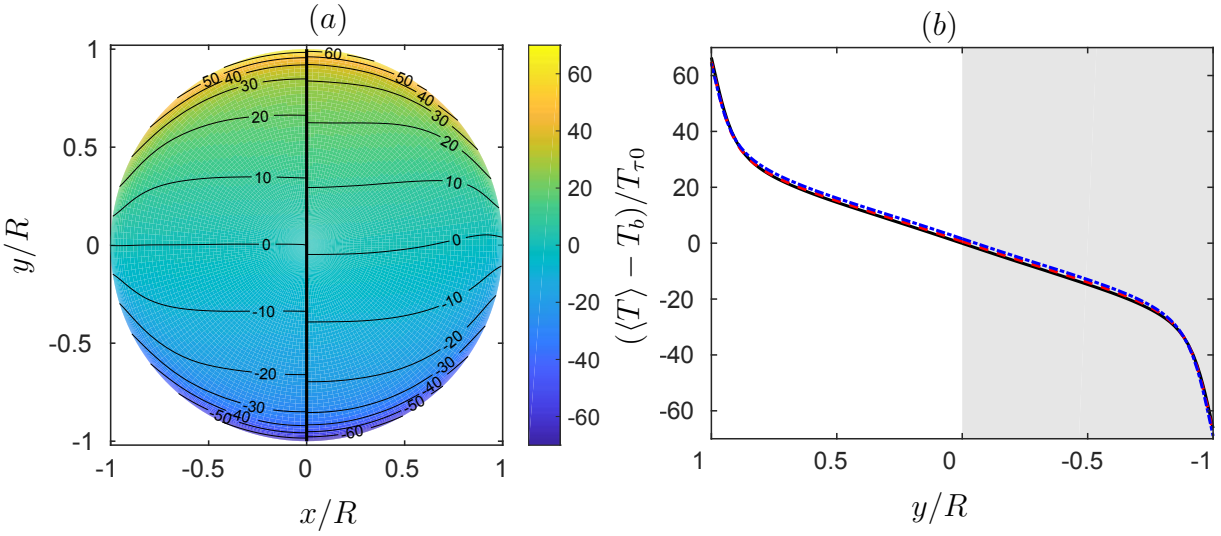

Figure 4.13: Mean temperature $(\langle T \rangle - T_b)/T_{\tau 0}$ comparison. (a) Case 1 field (left) is compared with Case 3 field (right). (b) Top-bottom profile comparison. Shaded area indicates cooled half of the pipe. Lines are as described in table 4.1.

It is interesting to note in figure 4.15 that the behaviour of T'_{rms} around the pipe center is very different to the behaviour of the velocity fluctuations, with all three cases developing a region of high temperature fluctuations at the pipe center. This effect is not seen in computations with uniform heat flux conditions (Redjem-Saad *et al.*, 2007; Piller, 2005) or isothermal conditions (Piller, 2005). This peak of T_{rms} around the pipe center is neither present in the cases discussed in Antoranz *et al.* (2015), where the pipe was heated on the upper wall, while the bottom wall was adiabatic. This suggests that the reason for the peak in the present cases is related to the higher available temperature difference between the upper and lower parts of the pipe. If we assume that the heat transfer (i.e., temperature mixing) between the walls is realised by large velocity structures, extending from the wall to the center of the pipe, the velocity structures in the upper (heated) half of the pipe will be contributing to the temperature variance at the center by bringing hot fluid to a region where the mean velocity is roughly T_b. On the other hand, the velocity structures in the bottom (cooled) half of the pipe, will be bringing cold fluid. Considering that the temperature difference between hot and bulk is similar to the temperature difference between cold and bulk, the result is that the temperature variance at the center is larger than if both halves of the pipe were at the same temperature.

4.5.4 Inner scaling

In this section, we further investigate the similarities of the velocity and temperature profiles near the wall for the three cases. Instead of using global variables (R, $u_{\tau 0}$ and $T_{\tau 0}$) for normalization of the statistics, we propose a conventional local scaling using inner units calculated at the wall.

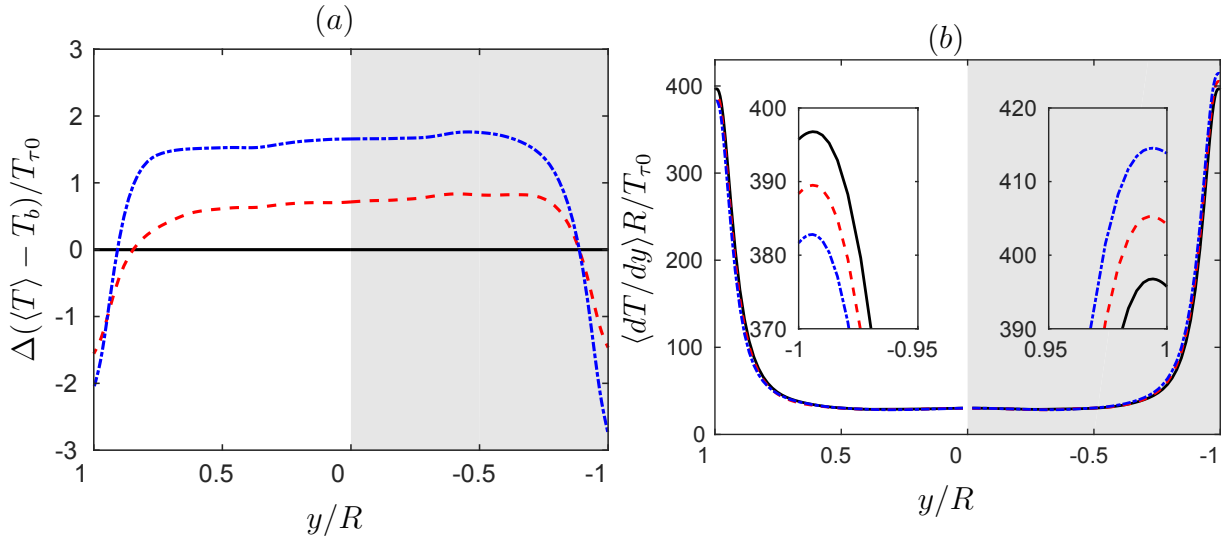

Figure 4.14: Mean temperature increment from Case 1 $\Delta(\langle T\rangle - T_b)/T_{\tau 0}$ (a) and temperature radial gradient (b) top-bottom profiles. Shaded area indicates cooled half of the pipe. Lines are as described in table 4.1.

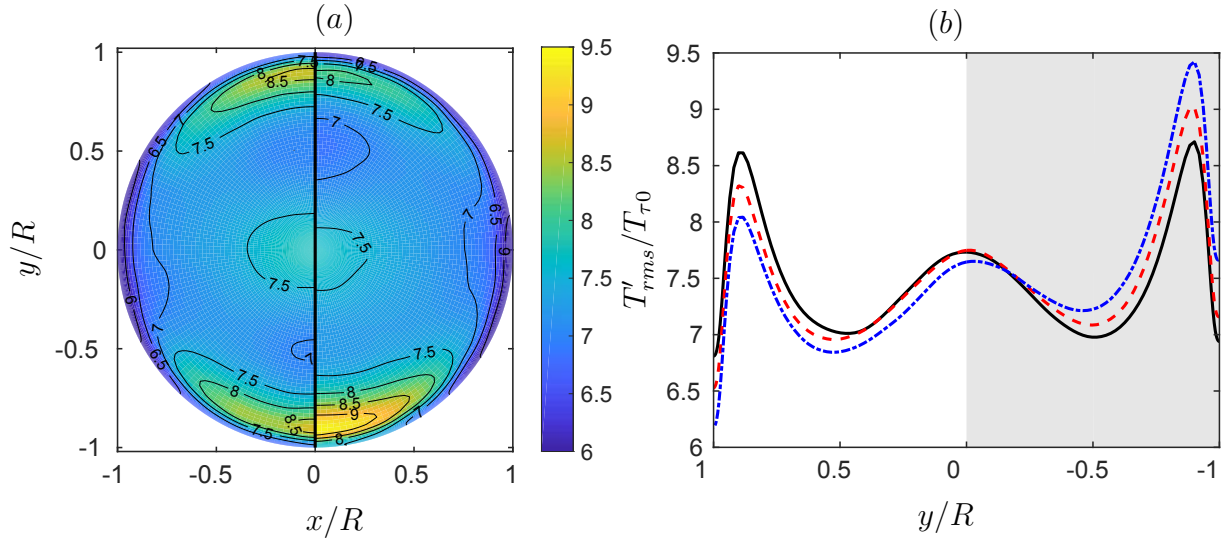

Figure 4.15: Root mean square temperature fluctuation $(T'_{rms}/T_{\tau 0})$ comparison. (a) Case 1 field (left) is compared with Case 3 field (right). (b) Top-bottom profile comparison. Shaded area indicates cooled half of the pipe. Lines are as described in table 4.1.

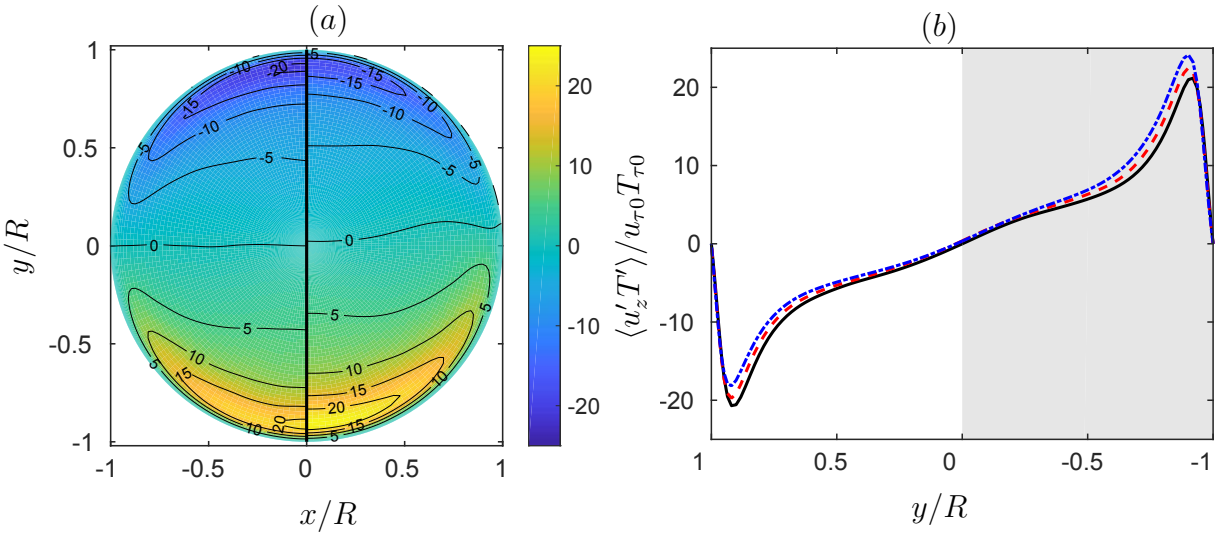

Figure 4.16: Axial turbulent heat flux ($\langle u_z' T' \rangle / u_{\tau 0} T_{\tau 0}$) comparison. (a) Case 1 field (left) is compared with Case 3 field (right). (b) Top-bottom profile comparison. Shaded area indicates cooled half of the pipe. Lines are as described in table 4.1.

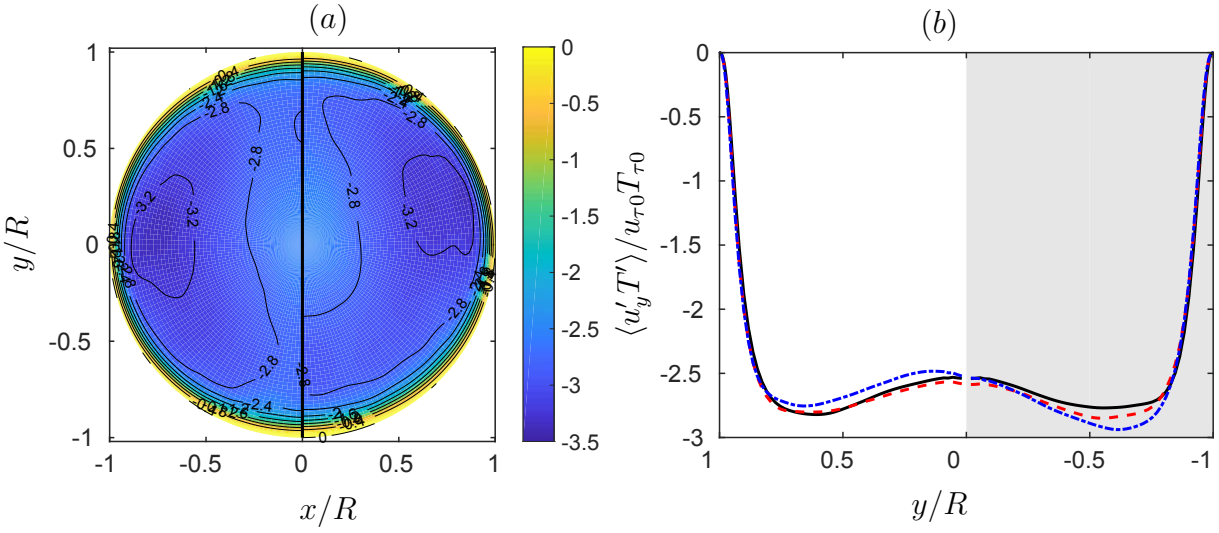

Figure 4.17: Vertical turbulent heat flux $\left(\langle u_y' T' \rangle / u_{\tau 0} T_{\tau 0}\right)$ comparison. (a) Case 1 field (left) is compared with Case 3 field (right). (b) Top-bottom profile comparison. Shaded area indicates cooled half of the pipe. Lines are as described in table 4.1.

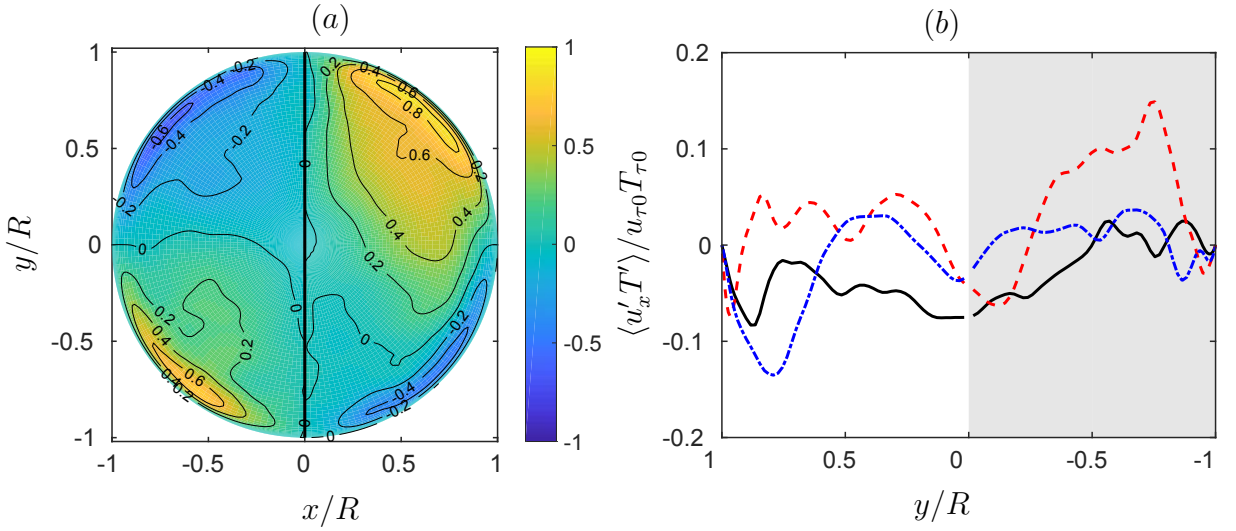

Figure 4.18: Horizontal turbulent heat flux ($\langle u'_x T' \rangle / u_{\tau 0} T_{\tau 0}$) comparison. (a) Case 1 field (left) is compared with Case 3 field (right). (b) Top-bottom profile comparison. Shaded area indicates cooled half of the pipe. Lines are as described in table 4.1.

We define a local friction velocity $u_\tau(\theta) = \sqrt{\langle -\nu \partial_r u_z |_{r=R} \rangle}$, and a local friction temperature $T_\tau(\theta) = q''_w(\theta)/(\rho C_p u_\tau(\theta))$. We also define a local viscous length-scale $\delta_v(\theta) = \langle \nu_w \rangle(\theta)/u_\tau(\theta)$. Flow properties normalized with local wall variables $\delta_v(\theta)$, $u_\tau(\theta)$ and $T_\tau(\theta)$ are denoted hereafter with the superscript $+$.

The mean axial velocity profiles in local inner units, $\langle u_z \rangle^+$, as a function of the inner wall distance, $(R-r)^+$, are provided in figure 4.19 (a). The profiles for all cases show good matching not only very close to the wall, but also in the outer region where an approximate log-law can be observed. Note that, due to the low Reynolds number of the present simulations, it is probably not possible to talk about an overlap or logarithmic region.

The profiles of the velocity fluctuations, $(u'_{z,rms})^+$, $(u'_{r,rms})^+$ and $(u'_{\theta,rms})^+$ are shown in figures 4.19 (b) and 4.20 (a) and (b) respectively. The turbulent shear stress, $\langle u'_r u'_z \rangle^+$, are shown in figure 4.21 (a)., Note that, although the profiles matched fairly well in the viscous sublayer (i.e., $(R-r)^+ \lesssim 10$), the position of the fluctuations peaks are not coincident using this wall distance normalization. Indeed, the peaks of the velocity fluctuations increase (decrease) and move further (closer) from the wall at the heated (cooled) side of the pipe, an effect that is stronger as $T_b/T_\tau 0/$ decreases. Note also that this behaviour is opposite to that observed in figures 4.8-4.12, when global variables are used for normalization. Similar behavior was found by Patel *et al.* (2015) using a semi-local inner scaling. We observe, however, that the profiles for the Case 3 near the cold bottom, in particular for $(u'_{r,rms})^+$ and $\langle u'_r u'_z \rangle^+$, deviate slightly from the others. This deviation might be explained considering that, for the Case 3 at the cold end, the friction Reynolds number is sensibly lower and the boundary layer thicker and the profile might be affected by the pipe curvature at distances from the wall of about $(R-r)^+ \sim 10$.

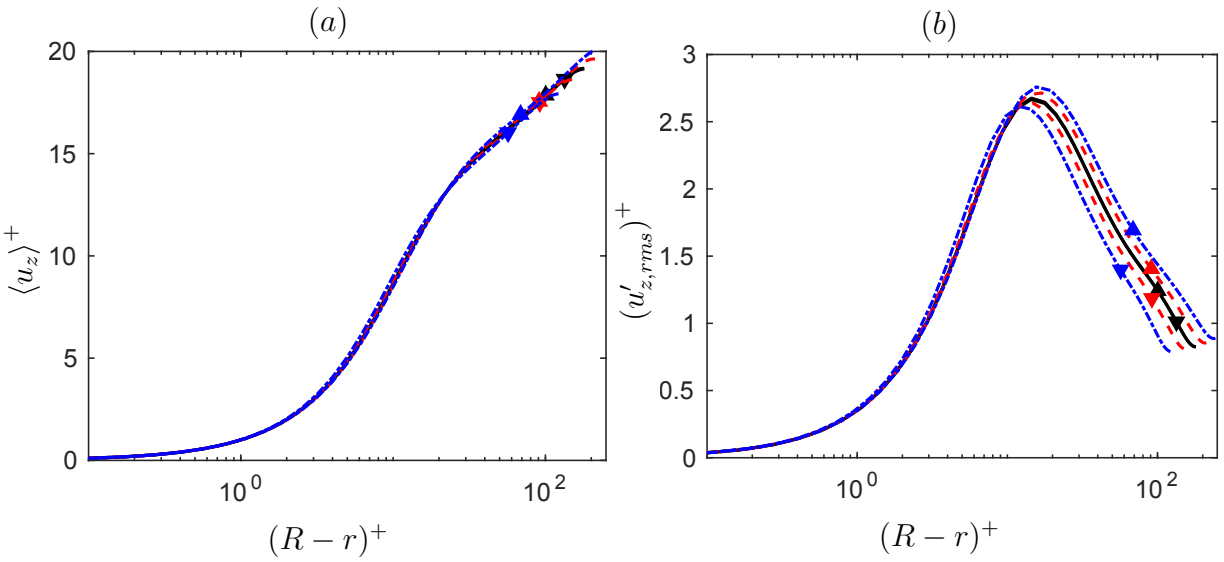

Figure 4.19: Mean axial velocity (a) and root mean square axial velocity fluctuation (b) non-dimensionalized with local variables. Lines are as described in table 4.1. Profiles at hot top are marked with ▲ and at the cold bottom with ▼

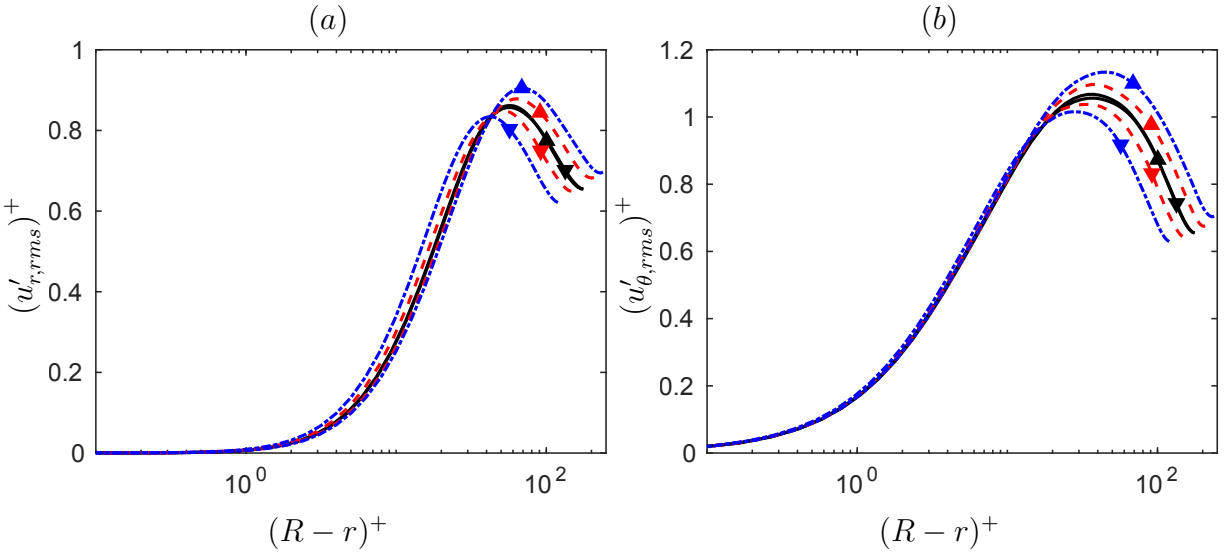

Figure 4.20: r.m.s. radial velocity fluctuation (a) and r.m.s. circumferential velocity fluctuation (b) non-dimensionalized with local variables. Lines are as described in table 4.1. Profiles at hot top are marked with ▲ and at the cold bottom with ▼

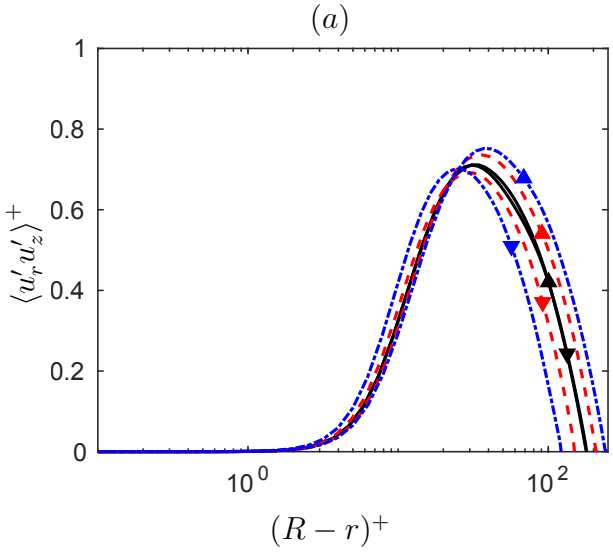

Figure 4.21: Shear stresses non-dimensionalized with local variables. Lines are as described in table 4.1. Profiles at hot top are marked with ▲ and at the cold bottom with ▼

Regarding the thermal field, figures 4.22 and 4.23 show the profiles of $\langle |T_w - T| \rangle^+$, $\langle T'_{rms} \rangle^+$, $\langle |u'_z T'| \rangle^+$ and $\langle u'_r T' \rangle^+$. Note that to ease the comparison, we take absolute values to be able to plot all the profiles in the positive axis. We observe that, as reported by several authors (see e.g. Redjem-Saad *et al.* (2007)), $T_\tau(\theta)$ and $u_\tau(\theta)$ are not able to collapse these profiles for cases with different Pr.

For the mean temperature profiles, figure 4.22(a) shows that the non-dimensional temperature gradient at the cooled wall becomes larger as $T_b/T_{\tau 0}$ increases, while the opposite occurs in the heated wall. The rms of the temperature fluctuations normalized with T_τ also increases with $T_b/T_{\tau 0}$ at the cooled half of the pipe, while it decreases in the heated half (figure 4.15b). In other words, as Pr_w increases the mean temperature gradient at the wall increases, and so does the value of T'_{rms} Note that, besides the plateau of T'_{rms} very close to the wall (within the layer where thermal diffusivity is dominant), figure 4.22(b) shows a peak in the buffer region that becomes more intense and moves closer to the wall as Pr_w increases. Similar trends are observed in the turbulent heat fluxes shown in figure 4.23.

Following the conclusions from Saha *et al.* (2014), we try to identify the dependence of the Prandtl number by assuming that the thermal variables scale as $\langle \Theta \rangle^+ / Pr^\beta$, where Θ is any thermal turbulent statistic and β defines the power-law effect of the local Prandtl number. For the mean temperature, eq. (4.4) and the definition of the local friction temperature yield $-\partial_r T|_{r=R} = T_\tau u_\tau / \nu Pr_w$, and hence $T^+ \approx Pr_w (R-r)^+$ very close to the wall. This classical result is confirmed in figure 4.24 (a) where the profile of $\langle |T_w - T| \rangle^+ / \langle Pr \rangle_w$ collapse in the conductive sublayer ($(R-r)^+ \leq 7$) for all the cases considered here, both in the heated and cooled walls.

For the scaling of the temperature fluctuations ${T'_{rms}}^+$, our simulations suggest $\beta = 0.37$, as

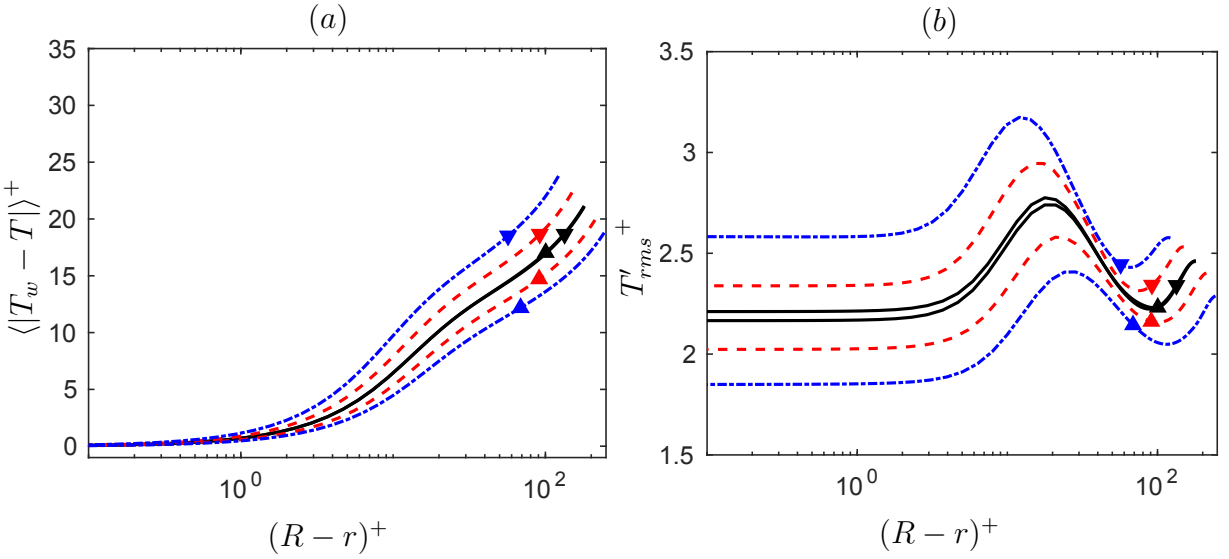

Figure 4.22: Mean temperature (a) and root mean square temperature fluctuation (b) non-dimensionalized with local variables. Lines are as described in table 4.1. Profiles at hot top are marked with ▲ and at the cold bottom with ▼

it can be observed in figure 4.24(b). On the other hand, the values of β that work better for the streamwise and radial turbulent heat fluxes are different. figure 4.25 (a) shows that $\beta = 0.5$ collapses the streamwise turbulent heat fluxes, while the radial component is shown in figure 4.25(b) to collapse for $\beta = 1$. Note that in all these cases the collapse is restricted to the conductive sublayer, namely $(R-r)^+ \lesssim 10$.

This last scaling for the turbulent heat transfer in the radial direction is in complete agreement with the findings of Saha *et al.* (2014) and Redjem-Saad *et al.* (2007). However, the studies on the Prandtl number effect from these authors show discrepancies with respect to the scaling laws presented here for ${T'_{rms}}^+$ and $\langle |u'_z T'| \rangle^+$. Since these authors imposed $T'_{rms} = 0$ at the wall for their heat flux boundary condition, the behavior of the temperature fluctuations near the wall is completely different, hence the scaling with the local Prandtl number. In the case of the streamwise turbulent heat flux $\langle u'_z T' \rangle^+$, results reported by these authors suggest a different exponent for the Prandtl number scaling law, but its value is also different between them. Discrepancies might be attributable to the dissimilar treatment of the pipe wall boundary conditions.

4.5.5 Heat fluxes and Secondary Flows

The introduction of variable fluid properties in the computation lead to the existence of small but discernible mean velocities in the radial and circumferential directions caused by the variations in temperature in the cross-plane. These secondary velocity vectors ($\langle u_x \rangle$ and $\langle u_y \rangle$) are presented in figure 4.26. The secondary velocities in Case 3 are up to $0.1 u_{\tau 0}$, as depicted in figure 4.26 (a), while in Case 2, shown in figure 4.26 (b), they only reach $0.06 u_{\tau 0}$ at maximum. Note that these

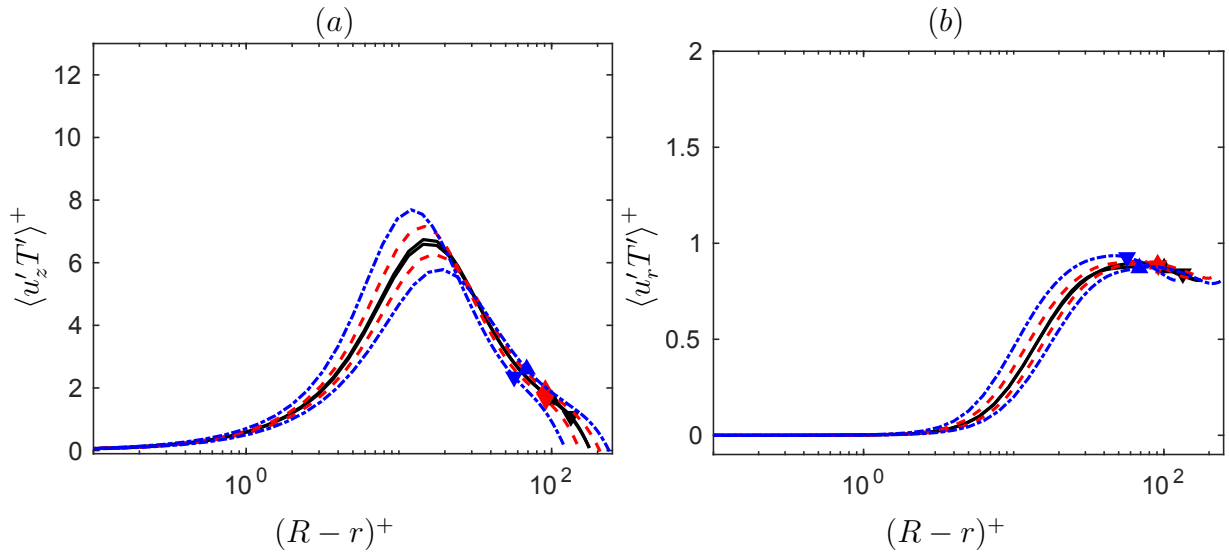

Figure 4.23: Axial (a) and radial (b) turbulent heat fluxes non-dimensionalized with local variables. Lines are as described in table 4.1. Profiles at hot top are marked with ▲ and at the cold bottom with ▼

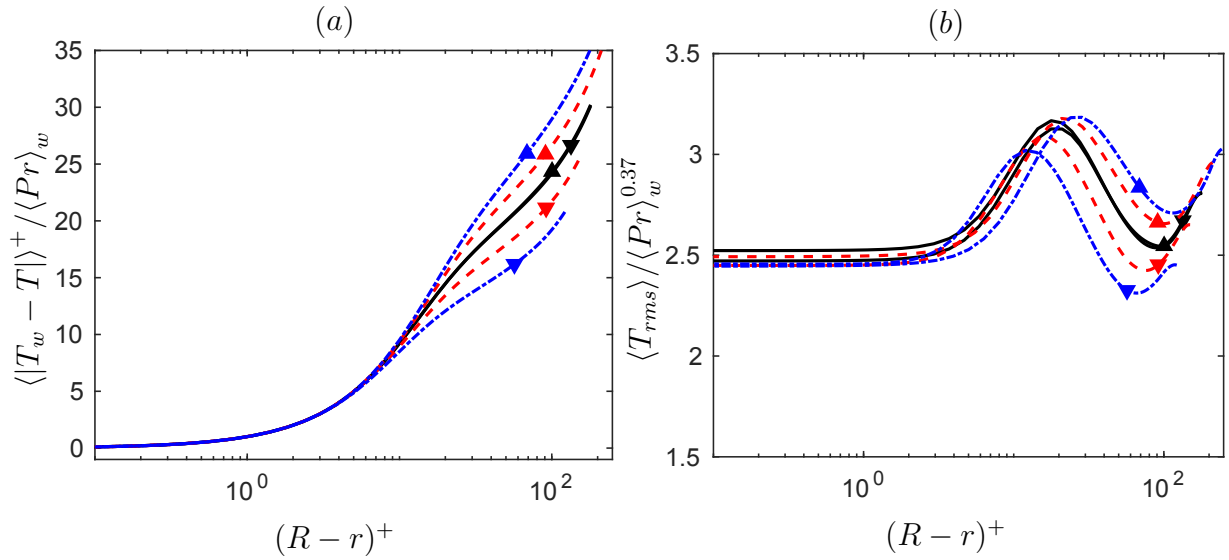

Figure 4.24: Mean temperature (a) and root mean square temperature fluctuation (b) non-dimensionalized with local variables and Pr power-law. Lines are as described in table 4.1. Profiles at hot top are marked with ▲ and at the cold bottom with ▼

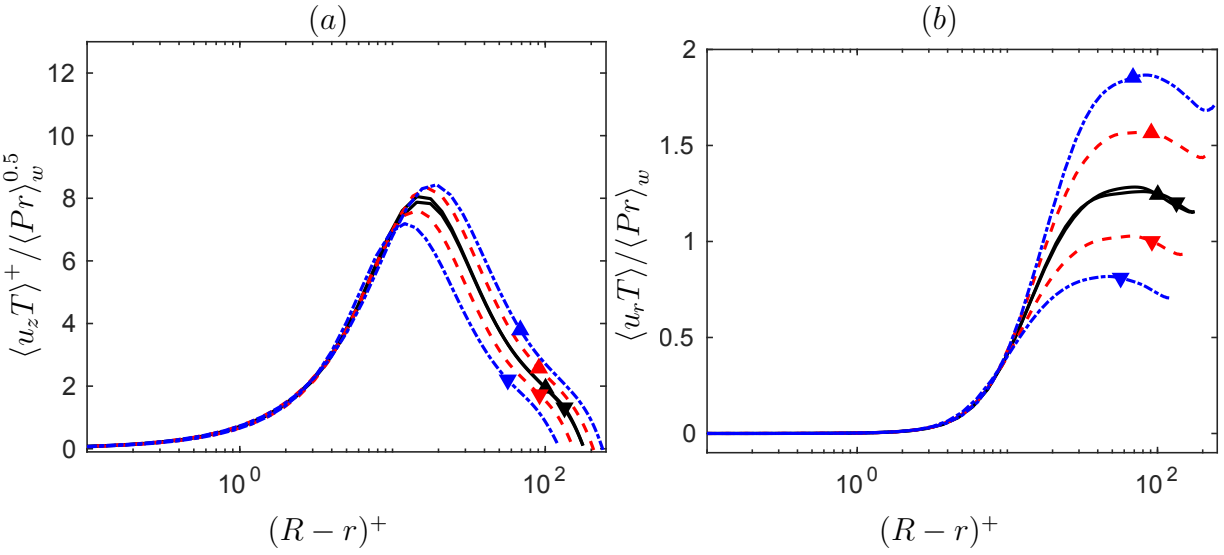

Figure 4.25: Axial (a) and radial (b) turbulent heat fluxes non-dimensionalized with local variables and Pr power-law. Lines are as described in table 4.1. Profiles at hot top are marked with ▲ and at the cold bottom with ▼

velocities are only about 0.6% of the bulk velocity. Nevertheless, these secondary flows have a contribution to the heat fluxes in the cross-plane that is not insignificant. We can distinguish in Case 3 two anti-symmetrical vortex moving hotter fluid from top to bottom along the vertical diameter and returning colder fluid along the pipe walls. We also identify a stagnant region at the cold bottom. This might be a consequence of the higher viscosity in that region, although further analysis are needed to support this conjecture. For Case 2 the secondary flow field structure is less clear, probably due to lack of convergence, but the mechanism might be similar as suggested by the heat flux distributions shown below.

The equation for mean heat fluxes in Cartesian coordinates is

$$\frac{\partial \langle u_i T\rangle}{\partial x_i} = \frac{\partial}{\partial x_i}\left(\langle \alpha(T)\frac{\partial T}{\partial x_i}\rangle\right). \tag{4.10}$$

We define the total heat flux, Φ, as

$$\Phi = \langle u_i\rangle(\langle T\rangle - T_b) + \langle u_i' T'\rangle - \langle \alpha(T)\rangle\langle\frac{\partial T}{\partial x_i}\rangle. \tag{4.11}$$

where the solenoidal component of the flux $\langle u_i\rangle T_b$ has been removed. Due to the fact that $T'/T_0 \ll 1$, and then $\alpha'/\alpha_0 \ll 1$, we have neglected the term $\langle \alpha' \partial x_i T'\rangle$.

In figure 4.27 we plot the three terms of the heat flux potential, the secondary flow heat flux, $\langle u_i\rangle(\langle T\rangle - T_b)$, the turbulent heat flux, $\langle u_y' T'\rangle$, and the diffusive heat flux, $-\langle\alpha\rangle\partial\langle T\rangle/\partial y$, normalized with $u_{\tau 0} T_{\tau 0}$. Heat flux distibutions are provided on two horizontal planes in the cross-plane, one in the heated upper part ($y/R = 0.5$) and another in the cooled lower part ($y/R = -0.5$) of

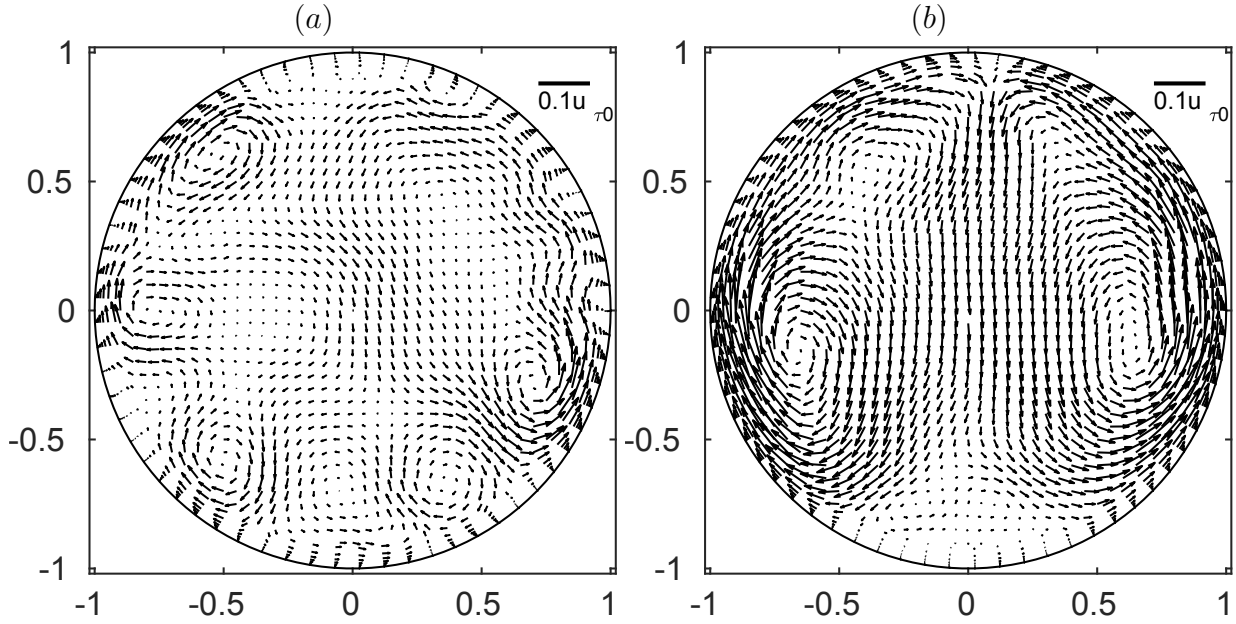

Figure 4.26: Secondary velocity vectors for Case 2 (a) and for Case 3 (b).

the pipe. The sign criteria we follow is that negative values indicate heat flux going from top to bottom.

Figures 4.27 (a) and (b) presents the heat diffusive term. The contribution of the heat diffusion $-\langle\alpha\rangle\partial\langle T\rangle/\partial y$ is maximum in the pipe walls and maintains a fairly constant value at the pipe center driven by the linear variation of the mean temperature in the flow (see figure 4.13). Profiles on the upper line and on the lower line are very similar for the three cases.

The normalized turbulent heat fluxes, dominant in most of the flow domain, are provided in figures 4.27 (c) and (d). Starting from zero on the pipe surface, the profiles reach a maximum near the wall and then decreases slightly towards the mid pipe diameter.

Finally, the heat flux contribution of the secondary flows is reported in figures 4.27 (e) and (f). Note that this term should be zero for Case 1 and that deviations from zero gives an indication of the statistics error due to lack of convergence. For Case 3, where the secondary flows are noticeable, we see a statistically significant different behavior in the heated and cooled parts. On the upper plane ($y/R = +0.5$) the heat flux goes from top to bottom near the pipe center but in the opposite direction near the walls. On the lower line ($y/R = -0.5$), the flux is strong and negative near the walls, indicating heat flux going down created by a cold stream moving upwards. These results are consistent with the vectors plot in figure 4.26.

4.5.6 Mean flow properties

Integral quantities are of great importance for engineering purposes in general and, in particular, for the design of solar power towers, where their economic perspectives heavily depend on the

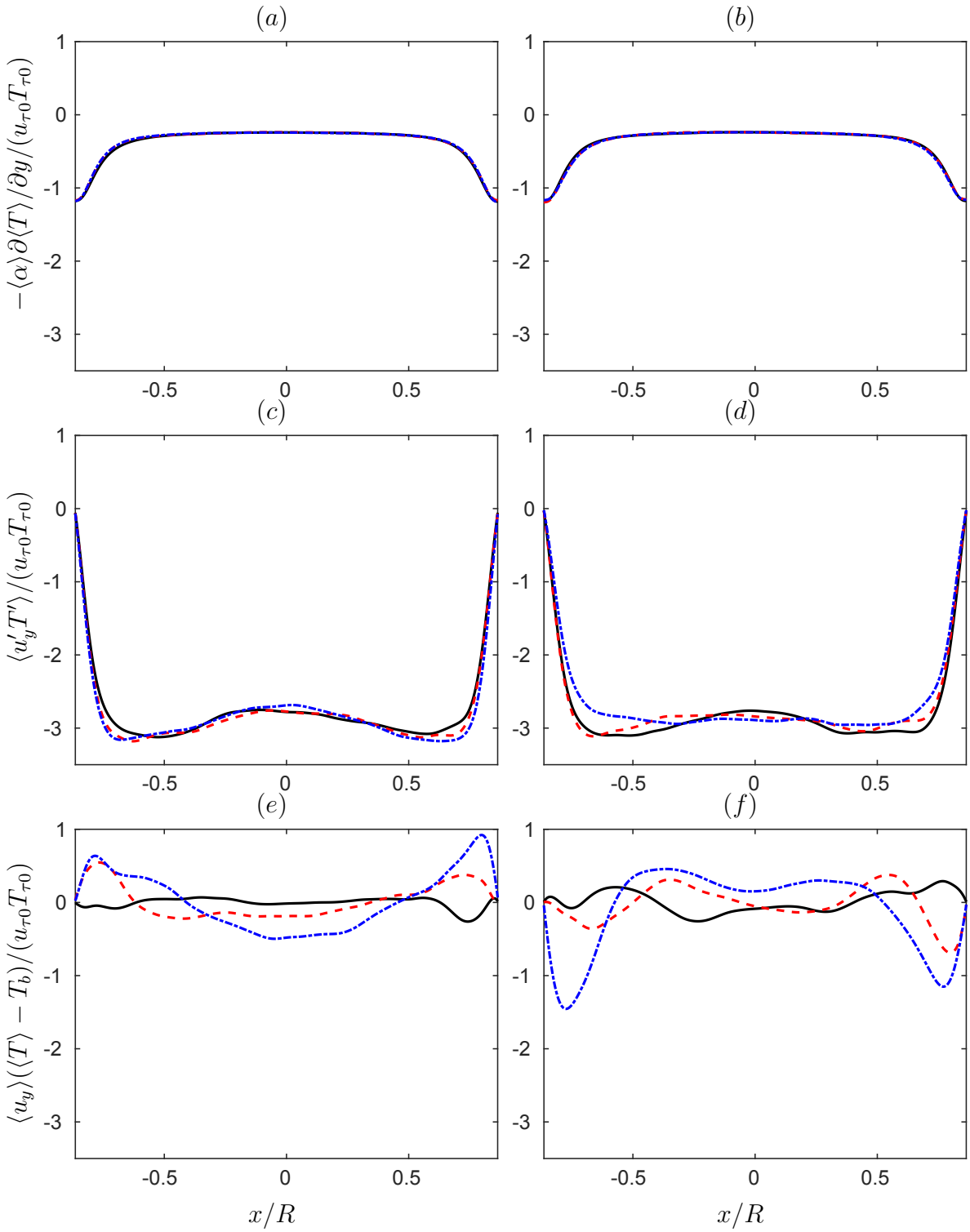

Figure 4.27: Heat flux terms at $y/R = 0.5$ (heated side (a), (c), (e)) and $y/R = -0.5$ (cooled side (b), (d), (f)).

Case	$Re_{\tau 0}$	Re_b	$U_b/u_{\tau 0}$	C_f
Case 1	180.0	5262	14.62	$9.36 \cdot 10^{-3}$
Case 2	180.0	5244	14.57	$9.43 \cdot 10^{-3}$
Case 3	180.0	5188	14.41	$9.63 \cdot 10^{-3}$
El Khoury *et al.* (2013)	182.2	5300	14.54	$9.45 \cdot 10^{-3}$
Wu & Moin (2008)	181.4	5300	14.61	$9.37 \cdot 10^{-3}$
Redjem-Saad *et al.* (2007)	187.0	5500	14.70	$9.25 \cdot 10^{-3}$
Piller (2005)	180.0	5273	14.65	$9.32 \cdot 10^{-3}$
Eggels *et al.* (1994)	179.9	5300	14.73	$9.22 \cdot 10^{-3}$
Colebrook Formula		5300		$9.21 \cdot 10^{-3}$

Table 4.2: Mean pipe mass flow and friction coefficient.

working fluid performance.

We present first the results for the mass flow, in terms of $U_b/u_{\tau 0}$, and the friction coefficient, C_f, predicted in our computations. Results are compared with those obtained from previous reported DNS with constant properties and with the Colebrook's empirical formula, showing good agreement with Case 1. As the bulk temperature is decreased, we see an increment of the overall flow resistance, that implies a $+2.88\%$ in the friction coefficient for Case 3 and a $+0.75\%$ for Case 2.

Regarding the mean thermal performance, table 4.3 shows the Nusselt numbers (Nu) for all the cases. The Nusselt number behavior on the pipe wall is shown in figure 4.6 (a) and discussed in section 4.5.1. From the DNS results we observe that, although the heat flux on the surface is not uniform, the Nussel number is fairly constant on the surface, except for the regions where the temperature at wall $\langle T \rangle_w$ is equal to the bulk temperature T_b and the Nusselt number is singular. We also observe that the cases with variable properties have different Nusselt number values on the hot wall and on the cold wall. The values we provide in table 4.3 correspond with the average of the circumferential variation of the Nusselt number from $\theta = \pi/4$ to $\theta = 3\pi/4$ for the hot wall and from $\theta = 5\pi/4$ to $\theta = 7\pi/4$ for the cold wall. Local Reynolds and Prandtl numbers are also averaged on the same arcs. The value of the Nusselt number for the case with uniform heating obtained from the Gnielinski formula is provided as reference. More appropriate is the comparison with the cases with sinusoidal heat flux boundary condition of Reynolds (1963) and Gärtner *et al.* (1974). Both authors calculated the turbulent heat transfer in a pipe subjected to circumferentially varying heat flux conditions with constant fluid properties using RANS models. While Reynolds (1963) used an isotropic model for the thermal eddy-diffusivity, Gärtner *et al.* (1974) improved the calculations by employing a non-isotropic model. The discrepancies we found in the computed Nusselt number for Case 1 and the value obtained using the data from Reynolds (1963) or Gärtner *et al.* (1974) could be attributed to the simplifications applied by these

Case	$\langle Re_\tau \rangle_w$	Re_b	$\langle Pr \rangle_w$	$\langle Nu \rangle$
Case 1	180.0	5262	0.70	11.94
Case 2 (Hot)	207.6	5244	0.58	12.20
Case 2 (Cold)	153.0	5244	0.86	11.72
Case 3 (Hot)	235.6	5188	0.49	12.42
Case 3 (Cold)	128.7	5188	1.08	11.52
Gärtner *et al.* (1974)		5300	0.70	10.49
Reynolds (1963)		5300	0.70	9.85
Gnielinski formula		5300	0.70	17.51

Table 4.3: Mean Nusselt numbers on pipe wall.

authors in the radial distributions of the eddy viscosity and eddy diffusivities and in the ratio used for the circumferential and radial diffusivities, which do not reflect the physical behavior specially at low Reynolds numbers (Antoranz *et al.*, 2015). Note that the improved model of Gärtner *et al.* (1974) get closer to the current result than the estimation of Reynolds (1963).

The inclusion in the computation of variable fluid properties produce an increase of the local Nusselt number onto the hot wall but a reduction onto the cold wall. From the value of $\langle Nu \rangle = 11.94$ for Case 1 with constant properties, Case 3 varies $+4.1\%$ in the heating region and -3.5% in the cooling region, while changes in Case 2 are around half than in Case 3, from $+2.2\%$ to -1.8%. Observe that, because of the wall temperature distribution, we have a local increment of the friction Reynolds number on the hot wall but a decrement of the Prandtl and Péclet numbers and the opposite happens on the cold wall (see figure 4.5). We try a correlation for the local Nusselt number as a function of the local friction Reynolds number and local Prandtl number obtaining the formula

$$\langle Nu \rangle = 0.225 \langle Re_\tau \rangle_w^{\,0.801} \langle Pr \rangle_w^{\,0.518}. \tag{4.12}$$

Exponent for the Reynolds number is coincident with the one used in the known correlation of Dittus-Boelter for the Nusselt number with uniform heat flux. Exponent for the Prandtl number is, however, larger compared with the value of 0.3 for a turbulent tube with cooling or 0.4 with heating used in the correlation.

The probability density function (p.d.f.) of the instantaneous temperature is plotted in figure 4.28. The area under the curves correspond with the percent of fluid within the integrand temperature range. An accurate estimation of the highest temperatures at the inner wall of the pipe, the so-called film temperature, is of special significance in the design of solar receivers. The film temperature might be limited due to it is responsible for salt decomposition and tube corrosion (Rodríguez-Sánchez *et al.* (2014)). We observe in figure 4.28 that the highest temperatures are reduced from Case 1 to Case 3. Although the shift is small, the probability of having temperatures

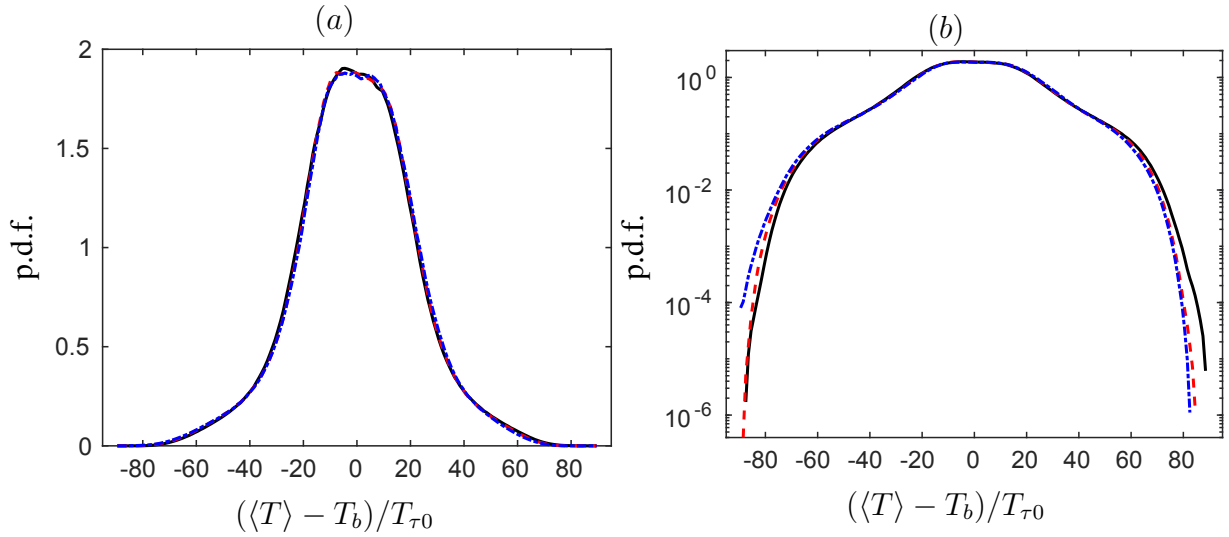

Figure 4.28: Temperature p.d.f. in linear scale (a) and in log scale (b). Lines are as described in table 4.1.

above a certain limit decrease. If we consider a film temperature threshold of $T/T_{\tau 0} = +75$, obtained after the study of Rodríguez-Sánchez *et al.* (2014), the probability of having higher temperatures is of 0.0150% for Case 1, of 0.0050% for Case 2 and of 0.0036% for Case 3.

4.6 Conclusions

DNS of a fully-developed turbulent flow in a pipe with circumferentially-varying heat flux boundary conditions and with temperature-dependent fluid properties was conducted aiming to study their effect on the turbulent heat transfer on the pipes of a solar heat receiver. The analysis was carried out for a pipe with global friction Reynolds number $Re_{\tau 0} = 180$, global Prandtl number $Pr_0 = 0.7$ and for three cases with different bulk temperatures, $T_b/T_{\tau 0} = \infty$, 1000 and 500, corresponding with null, low and high viscosity and diffusivity sensitivity to flow temperature variations.

Inasmuch as the heat flux boundary condition is the same for all cases, the mean temperature distribution on the pipe wall does not change significantly. However, the viscosity and diffusivity dependency on temperature produce the turbulent velocities and temperature fluctuations being enhanced near the cold bottom but dumped near the hot top. The r.m.s. temperature fluctuations at the pipe wall, T'_{rms_w}, has increments of around $+12\%$ and reductions of around -7% for the most sensitivity case. The near wall peak of TKE increased by $+7.8\%$ at the cold end and reduced by -5.2% at the hot end.

Considering an inner scaling using local variables at wall, we find good matching for the velocity statistics within the viscous sublayer, with some discrepancies arisen near the bottom of the pipe where the viscosity is higher. In order to collapse the temperature statistics in the conductive

sublayer, a power-law of the Prandtl number is applied to scale the profiles. The r.m.s. temperature fluctuations seems to match by rescaling the normalized profile using $\langle Pr \rangle_w^{0.37}$, while the stream-wise and radial turbulent heat fluxes need exponents of 0.5 and 1.0, respectively.

The non-homogeneous fluid properties induce the occurrence of secondary flows on the pipe cross-plane. These velocities have a contribution to the heat transfer that are same order than the conductive fluxes and accounts for one forth of the total heat flux crossing the pipe in the most sensitive case.

Finally, the analysis of the integral flow quantities show that, when we reduced the bulk temperature and the fluid properties are more sensitive to temperature variations, the overall friction coefficient increases by up to a $+2.88\%$. Regarding the heat transfer on the wall, characterized by the Nusselt number, we compute higher $\langle Nu \rangle$ on the heated wall (around $+4.1\%$) but lower $\langle Nu \rangle$ on the cooled wall (around -3.5%) when reducing the bulk temperature. The probability of finding film temperatures larger than $75T_{\tau 0}$ decreases from 0.0150% in the constant properties case to 0.0036% in the most sensitive case due to less turbulent activity near the heated wall.

5 Conclusions and recommendations for future work

5.1 Conclusions

In the present thesis we have investigated on the forced-convection heat transfer in the fully-developed turbulent pipe flow subjected to non-homogeneous heat flux boundary conditions and with temperature-dependent fluid properties. These conditions aimed to be representative of the problem of the tubes in a Central Solar Receiver using molten salts as currently found in modern Central Power Tower plants.

In a first approach to the problem, we have conducted DNS of the turbulent heat transfer in a pipe with circumferentially-varying heat flux boundary conditions but with constant fluid properties. The computation have been carried out for two Reynolds number ($Re_\tau = 180$ and 360) and two Prandtl numbers ($Pr = 0.7$ and 4). The numerical results demonstrate that most of the temperature turbulent fluctuations take place in the upper side of the pipe, where heat flux is maximum, while the r.m.s. temperature fluctuation is much smaller near the adiabatic wall. A second conclusions from the computations is that, while the Reynolds number has a small impact on the wall temperature distribution, the Prandtl number produces deep changes, being the circumferential variations of temperature more pronounced when Pr is higher. Finally, we have used the results from Chapter 1 to challenge the current correlations for the thermal eddy-diffusivities in the radial and circumferential directions. We have obtained the following outcomes.

First, we have observed that, despite the varying heat flux condition on the surface, the eddy-diffusivities are only functions of the radial direction but not of the circumferential direction.

Second, we have verified that, as measured in the experiments, eddy-diffusivities in the radial and circumferential directions are not equal, and that the ratio $\varepsilon_{h\theta}/\varepsilon_{hr}$ varies as the inverse of the wall distance near the wall for all Re_τ and Pr cases studied. This implies a correction over Launder's hypothesis where the anisotropic behaviour of the eddy-diffusivities was related to the ratio of mean square velocity fluctuations in the cross-plane.

And third, we have obtained the asymptotic behavior near the wall of the turbulent Prandtl numbers in radial and circumferential directions, finding that the latter increases faster with wall distance. This asymptotic behavior is independent of the Reynolds and Prandtl numbers, in the range considered in this study.

We have further analyzed the DNS database with the aim of identifying the motions responsible for the turbulent heat flux in the vertical direction. To this aim we have used a modal decomposition of instantaneous velocity and temperature fields in crossplanes. The modal decomposition employed is based on an extended proper orthogonal decomposition, in which the temperature is

decomposed using standard proper orthogonal decomposition while the velocity is decomposed with an extended proper orhogonal decomposition using the POD temperature basis. This allows to discern which velocity fluctuations are correlated to the temperature fluctuations. Indeed we have shown that while standard POD modes of velocity are distributed over the whole pipe, extended POD modes of velocity are concentrated in the upper part of the pipe, where most of the heat transfer is taking place. The combined analysis of a given POD temperature mode and its corresponding EPOD mode of velocity provides insight on the physical mechanisms of heat transfer. The study of the first few modes has resulted in the identification of the cross-plane vortices responsible for bringing hot fluid from the top to the pipe core. The size of these vortices seems to depend on the ratio between the thermal boundary layer thickness and the momentum boundary layer thickness, so that they are strongly affected by the Prandtl number. This analysis was followed by a more quantitative study in which we have reconstructed the temperature fields using POD modes and the vertical velocity fields using the corresponding EPOD modes. We have used these fields to compute a reconstructed turbulent heat flux in the vertical direction, finding that already with 16 modes we recover at least 50% of the total heat flux, while in all cases with 256 modes the reconstruction converges to the original heat flux. In addition, we have quantified the turbulent kinetic energy using the EPOD reconstructed velocity fields obtaining that with only 40% of the total turbulent kinetic energy we are able to reconstruct more than 95% of the turbulent heat flux in the vertical direction. This suggests that most of the heat transfer is due to relatively few turbulent structures, while the rest of the turbulence is *inactive* in the sense of heat transfer. The analysis presented has shown that extended proper orthogonal decomposition appears to be a suitable tool to assess the flow features associated with temperature fluctuations, a tool that deserves to be embraced by the heat transfer community. We hope that this work will contribute towards this aim.

Concerning the analysis of the variable fluid properties impact on the heat transfer problem, we have reported the findings of a DNS with sinusoidal heat flux boundary conditions and with temperature-dependent viscosity and diffusivity for three cases representative of null, small and high sensitivity with temperature, being the latter the case corresponding to the molten salt behavior.

We have observed that, although the mean temperature distribution on the pipe wall does not change significantly, the introduction of variable properties produce discernible changes in the velocity and temperature fluctuations between the cold side and the hot side of the pipe, being enhanced on the cooled wall but dumped on the heated wall. These differences can be attributable to the large change in viscosity with temperature for the molten salts, creating lower (higher) values of the local friction Reynolds number at the cold (hot) wall but higher (lower) values of the local Prandtl number.

Considering an inner scaling using local variables at wall, we have found good matching for the velocity statistics within the viscous sublayer, with some discrepancies arisen near the bottom of the pipe where the viscosity is higher. In order to collapse the temperature statistics in the

conductive sublayer, different power-laws of the Prandtl number are applied to scale the profiles. The r.m.s. temperature fluctuations seems to match by rescaling the normalized profile using $\langle Pr \rangle_w^{0.37}$, while the stream-wise and radial turbulent heat fluxes need exponents of 0.5 and 1.0, respectively.

The secondary flows on the pipe cross-plane induced by the non-homogeneous fluid properties have been shown to have a contribution to the heat transfer of the same order than the conductive fluxes accounting for one forth of the total heat flux crossing the pipe in the most sensitive case.

Finally, we have quantified the change of the integral flow parameters showing, for the most sensitive case in the study, an overall friction coefficient increase of about $+2.88\%$, a local Nusselt number increase on the heated wall around $+4.1\%$ but a reduction on the cooled wall around -3.5%. The probability of finding film temperatures larger than the assumed limit decreases from 0.0150% in the constant properties case to 0.0036% in the most sensitive case due to less turbulent activity near the heated wall.

5.2 Recommendations for future work

In this thesis, several Direct Numerical Simulations have been performed to accurately and reliably compute the turbulent heat transfer in a pipe replicating the case of Cental Solar Receivers tubes. We have taken particular care to analyze the results and to discuss their physical meaning. The outcomes have been contrasted with correlations or with experimental evidences when available and have been compared with the results obtained from other authors when adequate. Although the objectives of the thesis have been satisfactorily accomplished, there are some important issues that still need to be addressed.

The post-processing of the computational results have focused only on the mean variables and first moments of the turbulent fluctuations. This analysis has allowed us to described the overall performance of the heat transfer fluid running through the pipes and to gain a first insight of the changes in the turbulent process due to the non-uniform heat flux and to the variable fluid properties. Some of the ideas presented in the thesis might be reinforced by an analysis of higher order moments of the turbulent fluctuations as well as by a thorough study of the turbulence spectra.

It is also worth noting that the scope of the current study has been limited to values of the Reynolds and Prandtl numbers in the lower range of application for the case of Central Solar Receivers tubes using molten salts. A natural continuation of the work might extend the numerical simulations to the range of Reynolds numbers from $Re_\tau = 500$ to 1000 and of Prandtl numbers from $Pr = 4$ to 10. We also encourage the introduction of temperature-dependent density and specific heat laws in the governing equations, aiming to have a reliable representation of the molten salt behavior.

As a final recommendation, we suggest performing specific experiments for the cases and conditions presented in this thesis. Although our conclusions seem to be in agreement with the findings

described in the specialized literature, it would be of interest to perform a direct comparison with a comparable experiment.

Bibliography

ANTORANZ, A., GONZALO, A., FLORES, O. & GARCIA-VILLALBA, M. 2015 Numerical simulation of heat transfer in a pipe with non-homogeneous thermal boundary conditions. *Int. J. Heat and Fluid Flow* **55**, 45–51.

BALTZER, J. R., ADRIAN, R. J. & WU, X. 2013 Structural organization of large and very large scales in turbulent pipe flow simulation. *J. Fluid Mech.* **720**, 236–279.

BAUGHN, J., HOFFMAN, M., LAUNDER, B. & TAKAHASI, R. K. 1984 *J. Heat Transfer* **106**, 64–70.

BEJAN, A. 2016 *Advanced engineering thermodynamics*. John Wiley & Sons.

BENOIT, H., SPREAFICO, L., GAUTHIER, D. & FLAMANT, G. 2016 Review of heat transfer fluids in tube-receivers used in concentrating solar thermal systems: Properties and heat transfer coefficients. *Renewable and Sustainable Energy Reviews* **55**, 298–315.

BERKOOZ, G., HOLMES, P. & LUMLEY, J. L. 1993 The proper orthogonal decomposition in the analysis of turbulent flows. *Annu. Rev. Fluid Mech.* **25**, 539–575.

BLACK, A. & SPARROW, E. 1967 Experiments on turbulent heat transfer in a tube with circumferentially varying thermal boundary conditions. *J. Heat Transfer* **89** (3), 258–268.

BLACKWELL, B. F., KEYS, W. M. & MOFFAT, R. J. 1972 Report hmt-16. Thermosciences Division, Dept. Mech. Eng., Stanford Univ.

BORÉE, J. 2003 Extended proper orthogonal decomposition: a tool to analyse correlated events in turbulent flows. *Experiments in fluids* **35** (2), 188–192.

CHIN, C., MONTY, J. & OOI, A. 2014 Reynolds number effects in DNS of pipe flow and comparison with channels and boundary layers. *Int. J. Heat Fluid Flow* **45**, 33–40.

CHUNG, S. Y. & SUNG, H. J. 2003 Direct numerical simulation of turbulent concentric annular pipe flow: Part 2: Heat transfer. *Int. J. Heat Fluid Flow* **24** (3), 399–411.

CITRINITI, J. H. & GEORGE, W. K. 2000 Reconstruction of the global velocity field in the axisymmetric mixing layer utilizing the proper orthogonal decomposition. *J. Fluid Mech.* **418**, 137–166.

DITTUS, F. & BOELTER, L. 1930 Univ. of california publications on engineering. *Univ. of California publications in Engineering* **2**, 371.

DUWIG, C. & IUDICIANI, P. 2010 Extended proper orthogonal decomposition for analysis of unsteady flames. *Flow Turbul. Combust.* **84** (1), 25–47.

EGGELS, J., UNGER, F., WEISS, M., WESTERWEEL, J., ADRIAN, R., FRIEDRICH, R. & NIEUWSTADT, F. 1994 Fully developed turbulent pipe flow: a comparison between direct numerical simulation and experiment. *J. Fluid Mech* **268**, 175–210.

EL KHOURY, G., SCHLATTER, P., NOORANI, A., FISCHER, P., BRETHOUWER, G. & JOHANSSON, A. 2013 Direct numerical simulation of turbulent pipe flow at moderately high Reynolds numbers. *Flow, Turbul. Combust.* **91**, 475–495.

FISCHER, P. F., LOTTES, J. W. & KERKEMEIER, S. G. 2008 NEK5000 Web page. `http://nek5000.mcs.anl.gov`.

FLORES, O., MARUGÁN-CRUZ, C., SANTANA, D. & GARCÍA-VILLALBA, M. 2014 Thermal stresses analysis of a circular tube in a central receiver. *Energy Procedia* **49C**, 354–362.

GÄRTNER, D., JOHANNSEN, K. & RAMM, H. 1974 Turbulent heat transfer in a circular tube with circumferentially varying thermal boundary conditions. *Int. J. Heat Mass Transfer* **17**, 1003–1018.

GEMASOLAR 2017 Torresol energy: Gemasolar. `http://www.torresolenergy.com/TORRESOL/planta-gemasolar/es`, retrieved 10-07-2017.

GNIELINSKI, V. 1976 New equations for heat and mass transfer in turbulent pipe and channel flow. *Int. Chem. Eng.* **16** (2), 359–368.

GONZALO, A. 2013 Estudio numérico de transferencia de calor en conductos en régimen turbulento. Master's thesis, Univ. Carlos III de Madrid, Spain.

GUALA, M., HOMMEMA, S. E. & ADRIAN, R. J. 2006 Large-scale and very-large-scale motions in turbulent pipe flow. *J. Fluid Mech.* **554**, 521–542.

HELLSTRÖM, L. H. O., GANAPATHISUBRAMANI, B. & SMITS, A. J. 2015 The evolution of large-scale motions in turbulent pipe flow. *J. Fluid Mech.* **779**, 701–715.

HELLSTRÖM, L. H. O., MARUSIC, I. & SMITS, A. J. 2016 Self-similarity of the large-scale motions in turbulent pipe flow. *J. Fluid Mech.* **792**, R1–1–R1–12.

HELLSTRÖM, L. H. O. & SMITS, A. J. 2014 The energetic motions in turbulent pipe flow. *Phys. Fluids* **26** (12), 125102.

HELLSTRÖM, L. H. O. & SMITS, A. J. 2017 Structure identification in pipe flow using proper orthogonal decomposition. *Phil. Trans. R. Soc. A* **375**, 20160086.

HOLLINGSWORTH, D. K., KEYS, W. M. & MOFFAT, R. J. 1989 Report hmt-41. Thermosciences Division, Dept. Mech. Eng., Stanford Univ.

HOLMES, P., LUMLEY, J. L., BERKOOZ, G. & ROWLEY, C. W. 2012 *Turbulence, coherent structures, dynamical systems and symmetry*, 2nd edn. Cambridge University Press.

ISE 2017 ISE: UC3M Energy System Engineering. `http://ise.uc3m.es/`, retrieved 07-07-2017.

KIM, J. & MOIN, P. 1989 Transport of passive scalars in a turbulent channel flow. In *Turbulent Shear Flows 6*, pp. 85–96.

KLEWICKI, J. C., CHINI, G. P. & GIBSON, J. F. 2017 Prospectus: towards the development of high-fidelity models of wall turbulence at large Reynolds number. *Phil. Trans. R. Soc. A* **375**, 20160092.

KOLB, G. J. 2011 An evaluation of possible next-generation high-temperature molten-salt power towers. Sandia National Labs, Report No. SAND2011-9320.

LAUNDER, B. E. 1978 Heat and mass transport. In *Topics in Applied Physics. Turbulence* (ed. B. P.).

LEE, J., JUNG, S., SUNG, H. & ZAKI, T. 2013 Effect of wall heating on turbulent boundary layers with temperature-dependent viscosity. *J. Fluid Mech* **726**, 196–225.

LUMLEY, J. L. & POJE, A. 1997 Low-dimensional models for flows with density fluctuations. *Phys. Fluids* **9** (7), 2023–2031.

MATSUBARA, K., SAKURAI, A., MIURA, T. & KAWABATA, T. 2012 Spanwise heat transport in turbulent channel flow with prandtl numbers ranging from 0.025 to 5. *J. Heat Transfer* **134**, 041701.

MOORE, S. R., VERNON, M., HO, C. K., SIEGEL, N. P. & KOLB, G. J. 2010 Design considerations for concentrating solar power tower systems employing molten salt. Sandia Report 6978.

NASA 2017 Nasa: Climate change and Global warming. `https://climate.nasa.gov`, retrieved 07-07-2017.

NUSSELT, W. 1927 Die theorie des winderhitzers. *Z. Ver. Deut. Ing* **71**, 85–91.

PATEL, A., PEETERS, J. W., BOERSMA, B. J. & PECNIK, R. 2015 Semi-local scaling and turbulence modulation in variable property turbulent channel flows. *Physics of Fluids* **27** (9), 095101.

PETUKHOV, B. 1970 Heat transfer and friction in turbulent pipe flow with variable physical properties. *Advances in heat transfer* **6**, 503–564.

PICARD, C. & DELVILLE, J. 2000 Pressure velocity coupling in a subsonic round jet. *Int. J. Heat Fluid Flow* **21** (3), 359–364.

PILLER, M. 2005 Direct numerical simulation of turbulent forced convection in a pipe. *Int. J. Numer. Meth. Fluids* **49**, 583–602.

PRANDTL, L. 1904 On fluid motions with very small friction. *Verhldg* **3**, 484–91.

QUARMBY, A. & QUIRK, R. 1972 Measurements of the radial and tangential eddy diffusivities of heat and mass in turbulent flow in a plain tube. *Int. J. Heat Mass Transfer* **15**, 2309–2327.

REDJEM-SAAD, L., OULD-ROUISS, M. & LAURIAT, D. 2007 Direct numerical simulation of turbulent heat transfer in pipe flows: effect of Prandtl number. *Int. J. Heat Fluid Flow* **28** (5), 847–861.

RENEWABLE ENERGY 2017 Wikipedia. Renewable energy. `https://en.wikipedia.org/wiki/Renewable_energy`, retrieved 07-07-2017.

REYNOLDS, O. 1883 An experimental investigation of the circumstances which determine whether the motion of water shall be direct or sinuous, and of the law of resistance in parallel channels. *Proceedings of the royal society of London* **35** (224-226), 84–99.

REYNOLDS, W. C. 1963 Turbulent heat transfer in a circular tube with variable circumferential heat flux. *Int. J. Heat Mass Transfer* **6**, 445–454.

RODRÍGUEZ-SÁNCHEZ, M., SORIA-VERDUGO, A., ALMENDROS-IBÁÑEZ, J., ACOSTA-IBORRA, A. & SANTANA, D. 2014 Thermal design guidelines of solar power towers. *Applied Thermal Engineering* **63** (1), 428–438.

ROWLEY, C. W. & DAWSON, S. T. M. 2017 Model reduction for flow analysis and control. *Annu. Rev. Fluid Mech.* **49**, 387–417.

SAHA, S., KLEWICKI, J. C., OOI, A. S. H., BLACKBURN, H. M. & WEI, T. 2014 Scaling properties of the equation for passive scalar transport in wall-bounded turbulent flows. *Int. J. Heat Mass Transfer* **70**, 779–792.

SAMEEN, A. & GOVINDARAJAN, R. 2007 The effect of wall heating on instability of channel flow. *J. Fluid Mech* **577**, 417–442.

SCHWERTFIRM, F. & MANHART, M. 2007 DNS of passive scalar transport in turbulent channel flow at high Schmidt numbers. *Int. J. Heat and Fluid Flow* **28** (6), 1204–1214.

SIROVICH, L. 1987 Turbulence and the dynamics of coherent structures. Part I: Coherent structures. *Quart. Appl. Math.* **45**, 561–571.

SOLAR THERMAL ENERGY 2017 Wikipedia. Solar thermal energy. `https://en.wikipedia.org/wiki/Solar_thermal_energy`, retrieved 07-07-2017.

VON KÁRMÁN, T. 1937 The fundamentals of the statistical theory of turbulence. *J. Aeronautical Sciences* **4** (4), 131–138.

WU, X. & MOIN, P. 2008 A direct numerical simulation study on the mean velocity characteristics in turbulent pipe flow. *J. Fluid Mech.* **608**, 81–112.

ZONTA, F., MARCHIOLI, C. & SOLDATI, A. 2012 Modulation of turbulence in forced convection by temperature-dependent viscosity. *J. Fluid Mech* **697**, 150–174.

List of Tables

List of Figures